MXenes: A New Family of Two-Dimensional Materials and its Application as Electrodes for Li-ion Batteries

A Thesis

Submitted to the Faculty

of

Drexel University

by

Michael Naguib Abdelmalak

in partial fulfillment of the

requirements for the degree

of

Doctor of Philosophy

April 2014

DEDICATIONS

To my beloved son Martin and my lovely wife Martina, you both gave a different meaning of life.

ACKNOWLEDGMENTS

When I started thinking about writing this part, I was amazed by the number of people who helped me and deserve my sincere acknowledgment. I did my best to list all of them. However, I may have dropped, unintentionally, some of them; I would like to ask for their forgiveness.

First of all, words cannot express how grateful I feel toward my advisors: Prof. Michel Barsoum and Prof. Yury Gogotsi for their kindness providing unlimited support during my PhD study at Drexel University. Their enthusiasm and confidence in me was encouraging to think outside the box developing ideas and implementing them. None of the success I achieved could have been possible without their encouragement and their constructive feedbacks on my work. Each of them is a great scientist and an expert in his field. Also, each of them has his own working style. Thus, it was a very rich, an extremely useful, and a fruitful experience.

I would like to thank the undergraduate students: Joshua Carle, Laura Allen, Cerina Gordon, Brandon Eng, and Jay Shah who helped me in the laboratory over the four years of my PhD.

Thanks to Prof. Volker Presser who kindly taught me a lot of skills he masters. It was a very good coincidence to start my PhD at the same time that he started his postdoctoral fellowship at Drexel University. He was very helpful, encouraging, and an inspiring figure to me. Also, I'm grateful to him for hosting me in his new laboratory at INM – Leibniz Institute für Neue Materialien (Saarbrucken, Germany), where I conducted the *in situ* dilatometry study. Many thanks to Dr.

Jenifer Atchison and Dr. Mesut Aslan for their appreciated help during my stay in Germany.

I would like to thank Prof. Patrice Simon for hosting me in his laboratory at Université Paul Sabatier (Toulouse, France) where I was trained on preparations and testing of lithium ion batteries, LIBs. Also, Dr Jérémy Come is acknowledged for the very useful guidance during my training.

I would like to thank my colleagues in both MAX and Nanomaterials groups for their help in the laboratories and the excellent time I enjoyed working and entertaining with them. From MAX group, special thanks to Mohammed Shamma who welcomed me and helped to settle in Philadelphia and made me feel home in the first couple of weeks while I was more than 5500 miles away! I'm grateful to Babak Anasori, Nina Lane, Darin Tallman, Justin Griggs, Joseph Halim, Grady Bentzel, Michael Ghidiu, Matt Nelson, and Matthias Agne for the friendly working atmosphere they were keeping in the MAX group laboratories. Thanks to Daniel Vryhof for the synthesis of Mo_2GaC. Many thanks to Babak Anasori, in addition of being a good friend, his artistic touches gave MXenes excellent visibility all over the world.

From the Nanomaterials group (NMG) I'm grateful to Riju Singhal, Carlos Pérez, Min Heon, John McDonough, Olha Mashtalir, Boris Dyatkin, Kristy Jost, Amanda Pentecost, Kelsey Hatzell, Katie van Aken, Chang (Evelyn) Ren, Chuanfang Zhang (John), Zheng Ling for making the working experience in NMG labs full of fun. Special thanks to my friend Maria Lukatskaya for the very useful discussions we had and the encouraging spirit that she was spreading. Many thanks

to Yohan Dall'Agnese for his help in testing delaminated MXene electrodes in LIBs and for the very nice time that I enjoyed working with him during his M.Sc. practical work at Drexel University. I would like to thank Dr. Vadym Mochalin and Dr. Majid Beidaghi for the useful discussions.

The kind help from the MSE staff: Keiko Nakazawa, Yenneeka Long, Sarit Kunz, and Andrew Marx was highly appreciated. They saved me from troubles many times during my PhD. Also, I would like to thank the A.J. Drexel Nanomaterials Institute staff: Michelle Sipics, Danielle Tadros, and Jill Buckley for their help in solving administrative problems.

Dr. Murat Kurtoglu and Nina Lane are acknowledged for the theoretical calculations they conducted. I'm thankful to Olha Mashtalir, Darin Tallman, and Dr. Junjie Niu at Drexel University, in addition to Dr. Jun Lu from Linkoping University (Sweden) for the TEM work they conducted. I would like to thank Min Heon, Dr. Kevin M. Cook and Joseph Halim for carrying out the XPS measurements and large portion of the analysis. Special thanks to Boris Dyatkin for the BET and TGA measurements in addition to vacuum annealing treatments.

I'm grateful to Dr. Alexander Kolesnikov at Oak Ridge National Laboratory (ORNL) for the INS measurements. His enthusiasm gave me great impression about working environment in ORNL that encouraged me later to join the laboratory for my next career step. Dr. Yu Xie and Dr. Paul Kent at ORNL are acknowledged for modeling the surface of MXenes and its interaction with lithium that helped in answering many questions those arose from the experimental findings. Thanks to Dr.

Kyung-Wan Nam at Brookhaven National Lab (BNL) for carrying out *in situ* XAS measurements.

This work was supported by the Assistant Secretary for Energy Efficiency and Renewable Energy, Office of Vehicle Technologies of the U.S. Department of Energy under Contract No. DE-AC02-05CH11231, Subcontract 6951370 under the Batteries for Advanced Transportation Technologies (BATT) Program. Also supported by the Commonwealth of Pennsylvania's Ben Franklin Technology Development Authority through the Ben Franklin Technology Partners of Southeastern Pennsylvania.

The German Academic Exchange Service (DAAD) is acknowledged for the short term scholarship (registration number: A/12/72736) that supported my research trip to Prof. Presser's laboratory at INM, Saarbrucken, Germany. Also, I'm grateful to Partner University Fund (PUF) for supporting my research trip to Prof. Simon's laboratory at UPS, Toulouse, France.

A mixture of sincere apology with a lot of thanks is to my lovely wife Martina. All the extra time I dedicated to this work was discounted from the very precious time of being with her. Also, for being with me during my PhD trip she sacrificed a lot of things in her career. Thus, I owe her every single success I achieved in my career! I wish one day I'll be able to return back part of her favors.

Last but not least, I would like to thank my parents and sister for their love, unlimited support, unconditional encouragement, and the efforts they exerted growing me up since I was a kid till the moment that I became a father! I would not

have been able to achieve any success without their love and support. I wish that I have met their expectations for their little child.

TABLE OF CONTENTS

LIST OF TABLES

LIST OF FIGURES

ABSTRACT

MXenes: A New Family of Two-Dimensional Materials and its Application as Electrodes for Li-ion Batteries

Michael Naguib Abdelmalak

Advisors: Prof. Michel W. Barsoum and Prof. Yury Gogotsi

Two-dimensional, 2D, materials, such as graphene, possess a unique morphology compared to their 3D counterparts, from which interesting and novel properties arise. Currently, the number of non-oxide materials that have been exfoliated is limited to two fairly small groups, *viz.* hexagonal, van der Waals bonded structures (*e.g.* graphene and BN) and layered transition metal chalcogenides.

The MAX phases are a well established family of layered ternary transition metal carbides and/or nitrides, with a composition of $M_{n+1}AX_n$, where M is an early transition metal, A is one of A group elements, X is C and/or N; with n = 1, 2, or 3. The aim of this work is to exfoliate the MAX phases and produce 2D layers of transition metals carbides and/or nitrides by the selective etching of the A layers from the MAX phases. We labeled the resulting 2D $M_{n+1}X_n$ layers "*MXenes*" to emphasize the loss of the A group element from the MAX phases and the suffix "*ene*" to emphasize their 2D nature and their similarity to graphene.

The etching process was carried out using aqueous hydrofluoric acid at room temperature. Thirteen different MXenes were produced as a result of this work, *viz.,* Ti_2C, Nb_2C, V_2C, Mo_2C, $(Ti_{0.5},Nb_{0.5})_2C$, $(Ti_{0.5},V_{0.5})_2C$, Ti_3C_2, $(Ti_{0.5},V_{0.5})_3C_2$, $(V_{0.5},Cr_{0.5})_3C_2$, Ti_3CN, Ta_4C_3, Nb_4C_3 and $(Nb_{0.5},V_{0.5})_4C_3$. The as-synthesized MXenes were terminated with a mixture of OH, O, and/or F groups. Sonicating

MXenes resulted in separating the stacked layers to a small extent. When Ti_3C_2 was intercalated with dimethylsulfoxide, however, followed by sonication in water, large-scale delamination occurred, which resulted in aqueous colloidal solutions that could in turn be fabricated into MXene "paper".

MXenes were found to be electrically conductive, hydrophilic and stable in aqueous environments, a rare combination indeed, with huge potential in many applications, from energy storage, to sensors to catalysts. This work focused on the use of MXenes as electrode materials in Li-ion batteries. They exhibited excellent capability to handle high cycling rates with good gravimetric capacities. The lithiation and delithiation were found to be due to redox intercalation/deintercalation reactions.

CHAPTER 1: INTRODUCTION

Two-dimensional, 2D, solids - defined as crystals with very high aspect ratios and thicknesses that are a few atomic layers hick - have garnered tremendous interest recently. By far the most studied of all 2D materials is graphene, a material that is comprised of atomically thin layers of sp^2 bonded carbon atoms, connected by aromatic in-plane bonds. Graphene was known for decades, but it was not until Novoselov and Geim *et al.*[1] managed to isolate a single layer of it and characterized its electronic properties that interest in this material has exploded. This is the work that earned them the Nobel Prize in Physics for 2010.

In general, 2D materials are finding their way in many applications ranging from electronic devices (sensors, transistors, *etc.*)[2, 3] to electrochemical energy storage electrodes,[4-6] and reinforcement in composites.[7-9] Although graphene has attracted more attention than all other 2D materials combined, its simple chemistry may be considered as a double-edged sword that limits its use. Complex, layered structures that contain more than one element may offer new properties because they provide a larger number of compositional variables that can be tuned for achieving specific properties. Here I would like to quote from Castro Neto and Novoselov's paper on 2D materials beyond graphene where they said: "*Graphene is probably the most famous example, but there are numerous other examples with amazing electronic and structural properties.*"[10] Beyond graphene, other 2D materials such as hexagonal boron nitrides, h-BN,[11] transition metal dichalcogenides, TMDs,[12] metal oxides and hydroxides are well known.[13]

As far as I am aware, there were no reports in the literature on truly 2D layers of transition metal carbides nor nitrides, before I started this work in 2010. An attempt to produce nanosheets of titanium and niobium carbides was reported by Chen *et al*.[14] They used few-layer graphene as a template and reacted them with volatile titanium or niobium iodides. The resulting nanosheets were found to be polycrystalline (cubic rock salt structure) with an average crystalline size of 8-12 nm. Thus, while not truly a 2D transition metal carbide, it can be considered as a thin film.

It is well established that the ternary carbides and nitrides with a $M_{n+1}AX_n$ chemistry – where M is an early transition metal (one of the following: Sc, Ti, V, Cr, Zr, Nb, Mo, Hf, and Ta), A is: Al, Si, P, S, Ga, Ge, As, Cd, In, Sn, Tl, or Pb, while X is carbon and/or nitrogen, and n = 1, 2, or 3– form laminated structures with anisotropic properties.[15] These, so called MAX, phases are layered hexagonal -space group $P6_3/mmc$- with two formula units per unit cell. As shown in Figure 1, layers of edge shared M_6X octahedrons interleaved with pure A-group element layers. Depending on the value of n, the thickness of the $M_{n+1}X_n$ change; if n = 1 – resulting in the 211 phases, then the layer consists of a single block of octahedra (3 atoms thick). If n = 2, then the 312 phases, consist of 2 octahedra blocks; if n = 3, then the 413 phases consist of 3 blocks of octahedra. The thickness of the 211, 312 and 413 layers (Figure 1) are respectively, ~0.2-0.3 nm, ~0.3-0.7 nm, and ~ 0.6-0.9 nm, thick.

Currently more than sixty different pure MAX phases are known. However, given that the MAX phases can also be synthesized with different combinations, or solid solutions, of M atoms, such as $(Ti_{0.5},Nb_{0.5})_2AlC$,[16] A atoms, such as $Ti_3(Al_{0.5},Si_{0.5})C_2$,[17] and on the X sites such as $Ti_2Al(C_{0.5},N_{0.5})$,[18] their potential number is quite large indeed.

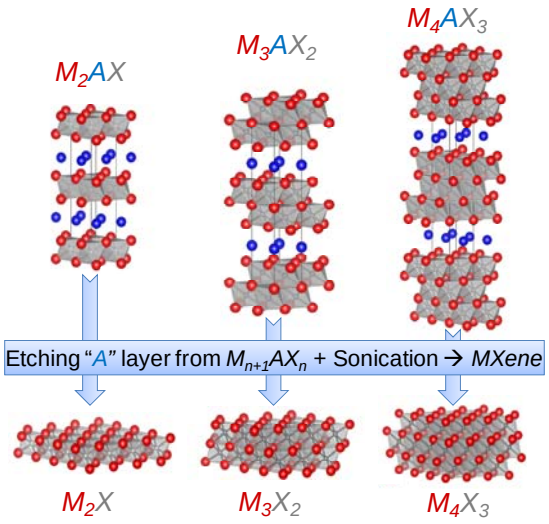

Figure 1: Schematic for the MAX phases structure and the resulted 2D layers after etching the A layers and sonicating them. Reproduced with permission.[19]

The mechanical deformation of the MAX phases – which is mediated by basal dislocations and is quite anisotropic - can lead to partial delamination and formation of lamellas with thicknesses that range from tens to hundreds of nanometers. [20] However, none of MAX phases had ever been exfoliated into a few nanometer thick, crystalline layers reminiscent of graphene for the simple reason that most of the M-A bonds are quite strong indeed. Furthermore, as far as I am aware, until our publication on the subject there were no reports on the selective room, or even moderate, temperature liquid or gas phase extraction - of the A-group layers from the MAX phases and/or their exfoliation. Interestingly, Hoffman and *et al.*[21] showed that it is relatively straightforward to extract both the M and A to form disordered graphitic carbon called carbide derived carbon, CDCs. The latter are microporous, but not layered.

This work has two main objectives. The first is *to exfoliate the MAX phases and produce 2D layers of transition metals carbides and/or nitrides by the selective etching of the A layers from the MAX phases.* We labeled the resulting 2D $M_{n+1}X_n$ layers

"*MXenes*" to emphasize the loss of the A group element from the MAX phases and the suffix "*ene*" to emphasize their 2D nature and relationship to graphene. The approach I used for exfoliating MAX phases is *"selective etching of A layers out from the MAX phases"* As noted above. up-to-date, over sixty MAX phases are known to exist.[22] It follows that the ability of removing the A atoms layers from the MAX structure could in principle lead to more than twenty possible "pure" $M_{n+1}X_n$ chemistries. The fact that MXenes can also be synthesized from MAX solid solutions on the M and X sites will result in countless other 2D materials.

The application I explored for MXenes was their use as electrode materials *in Li-ion batteries, LIBs.* This task constitutes the second objective of this work namely *investigating the performance of MXenes as electrode materials for LIBs and understanding the lithiation/delithiation mechanisms*.

In addition to the introduction and appendices, this thesis consists of five chapters. In chapter two, the background and literature survey on inorganic 2D materials and the MAX phases are presented. While chapter three focuses on the materials and methods used in this work. The outcomes on the materials synthesis fronts are discussed in chapter four. The performance of MXenes as electrode materials in LIBs and the mechanisms of their lithiation and delithiation are explored in chapter five. Finally, the conclusions and outlook for future work are given in chapter six.

CHAPTER 2: BACKGROUND AND LITERATURE SURVEY

In this chapter a background and literature survey of inorganic 2D materials covering their categories and properties, in addition to their synthesis techniques used to produce them is summarized. A brief description for their applications, in general, and in LIBs their usage as electrode materials are reviewed.

Detailed description for the structure and properties of the MAX phases will be provided in this chapter as well. The focus will be on their structure and chemical reactivity. At the end of the chapter the objectives of this work will be discussed.

1.1 Categories of Two-Dimensional Materials

1.1.1 Graphene and its Analogues:

Graphene is a single hexagonal layer of sp^2 bonded carbon, C, atoms. As shown in Figure 2, graphene can be considered as the parent for all other graphitic allotropes (fullerenes, carbon nanotubes, and graphite).[23] The term "*Graphene*" was first introduced by Mouras *et al.* [24] in 1987 to describe a single atomic layer of carbon that is the building block of graphite. Much earlier reports on atomically thin carbon based layers can be found in the literature. For example, as early as 1859, Brodie started with graphite and made graphite oxide out of it, and produced extremely thin carbon-based layers that he called "*Graphon*".[25] More examples for early attempts to exfoliate graphite can be found in a review article by Chung.[26] However, it was only in 2010 that graphene garnered the world's attention, after the Royal Swedish Academy of Sciences awarded Andre Geim and Konstantin Novoselov the Nobel Prize in Physics for "groundbreaking experiments regarding the two-dimensional material graphene".[27]

Geim and Novoselov *et al*.[1] were the first to isolate single graphene layers and explore their electronic properties. They found that graphene offers ballistic transport.[1]

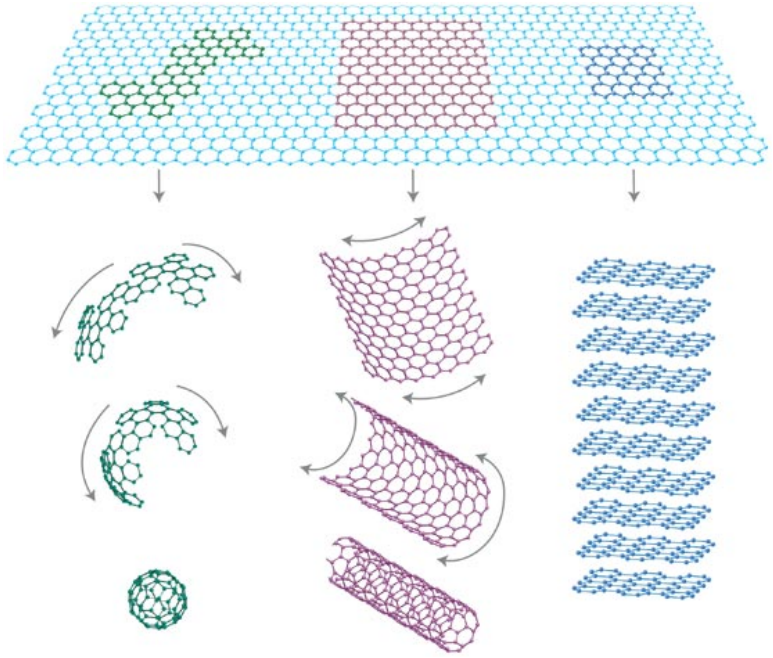

Figure 2: Schematic for the graphene sheet (on top) and other graphitic allotropes made of graphene: graphite (at the bottom right side) which is a stack of graphene sheets, carbon nanotube (bottom middle) which is a roll of graphene, and fullerene (bottom left side) which is a ball of wrapped graphene. Reproduced with permission.[23]

Similar to graphite, hexagonal boron nitride, h-BN, consists of atomically thin sheets of hexagons in which each side of the hexagon is a born-nitrogen couple instead of the carbon-carbon one in the case of graphene (Figure 3).[28] Unlike graphite, h-BN is an insulator [29] and is white in color, which is why sometimes, its atomic layers are referred to as "*White Graphene*". Pacilé *et al.*[30] were the first to report on the exfoliation of few layers of h-BN. Combination of graphene and h-BN forming boron carbonitride atomic layers has been reported.[28] Hexagonal monolayers of BC_3 on NbB_2 were synthesized by Ueno *et al.*[31]

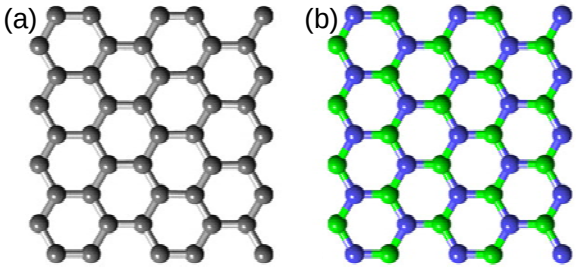

Figure 3: Schematic of top view of (a) graphene, and, (b) h-BN layer. Grey spheres represent C atoms, while the green and blue spheres represent B and *n* atoms, respectively. Reprinted by permission from Macmillan Publishers Ltd: Nature Communications, [28] copyright 2014.

Silicon and germanium in 2D forms, (so-called silicene and germanene, respectively) are considered to be graphene analogues, since they are expected to have hexagonal structures single atomic thickness.[32] Although, they have been extensively studied using theoretical calculation and predicted to be stable, [32-34] only silicene was recently synthesized experimentally.[35, 36]

1.1.2 Transition Metal Dichalcogenides (TMDs):

Transition metal dichalcogenides (TMDs) represent a large family of layered materials with composition of $\dot{M}\dot{T}_2$, where $\dot{M}$ is transition metal of groups IV-VI (Ti, V, Zr, Nb, Mo, Hf, Ta, W, *etc.*) and $\dot{T}$ is one of the chalcogens, namely: sulfur, S, selenium, Se, or tellurium, Te. As shown in Figure 4, each layer consists of chalcogens on the outer surfaces and transition metals in the center.[37] The bonding within each $\dot{T}$-$\dot{M}$-$\dot{T}$ layer is strong primary bonding, while the interlayer bonding is a weak van der Waals one.[38] These weak bonds between the layers, allows for the relatively facile exfoliation of TMDs. Even before the spark of finding the outstanding properties in graphene that attracted attention to all other 2D materials, earlier reports on the exfoliation of TaS_2,[39] NbS_2,[40] and MoS_2 [41] can be found in the literature.

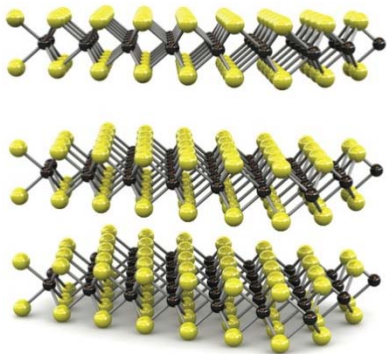

Figure 4: Atomic model of transition metal dichalcogenides. The black and yellow spheres represent transition metal, and chalcogens (S, Se, or Te) atoms, respectively. Reprinted by permission from Macmillan Publishers Ltd: Nature Nanotechnology, [42] copyright 2011.

1.1.3 Metal Oxides and Hydroxides:

Layered metal oxides and hydroxides can be considered as the largest category of 2D materials, especially if clays are included. In layered metal oxides, as shown in Figure 5, each layer is considered to be a negatively charged slab of corner and/or edge-shared octahedral units of $M'O_6$ (M' is Ti, Nb, Mn, Ta, Co, W, *etc.*) with alkali cations (K^+, Rb^+, Cs^+, *etc.*) filling the interlayer spacing.[13] Unlike, graphene and TMDs the negatively charged layers here are electrostatically bonded together through the alkali cations.[13] Thus, chemical modification is usually needed, to exfoliate these layered oxides, which involves reacting the alkali cations.[43-45] This will be discussed in detail later in Section 1.2. Layered vanadium oxide (V_2O_5) molybdenum oxide (MoO_3) can be considered as exceptions, since the bond between the layers is a weak van der Waals.[46-48]

Layered double hydroxides consist of water separated octahedral brucite-like layers of divalent and trivalent metal ions (M^{2+} and M^{3+} respectively). The layers are positively charged and the charge is controlled by the molar fraction, x, of the trivalent ion. Their general formula is: $[M^{2+}_{1-x}M^{3+}_{x}(OH)_2]^{x+}[A^{\gamma-}_{x/\gamma}]^{x-}\cdot mH_2O$, where A is γ-valent anions balancing the charge of the layer.[13, 49]

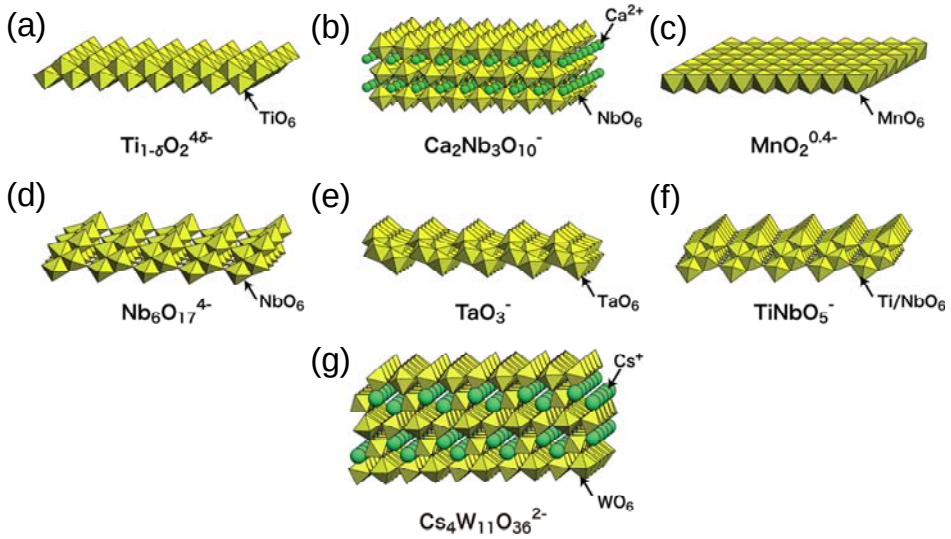

Figure 5: Schematic for the oxide layer structure of (a) titanium, (b) calcium niobium, (c) manganese, (d) niobium, (e) tantalum, (f) titanium niobium, and (g) cesium tungsten. Reprinted by permission from WILEY-VCH Verlag GmbH: Advanced Materials, [13] copyright 2010.

Clays can also be considered as layered metal hydroxides. Each clay layer consists of corner shared silica tetrahedros sheets and sheets of alumina octahedrons. Both Al and Si cations can be substituted by other cations. For example, Mg^{2+} or Fe^{2+} can replace the Al^{3+} resulting in negatively charged sheet, also Al^{3+} can replace Si^{4+} in the silica tetrahedral sheets. To achieve charge neutrality in case of negatively charged sheets, cations such as Na^{+}, Ca^{2+}, *etc.* occupy the interlayer spacings. Clays are classified into subgroups based on the ratio of alumina to silica sheets in the layer. If the number of silica to alumina sheets is 1:1, the clay is called kaolinite; if it is 2:1 then it is either classified as smectite, vermiculite, illite, or chlorite. In most clays the bonds between the layers are mainly hydrogen bonds.[50] When layers are highly charged, they are held together electrostatically by the interlayer cations. Since they are hydrophilic by nature and the layers are weakly bonded, many compounds including water can intercalate

easily between the clay layers and increase the spacing between them resulting in swelling.[51-53] It is worth noting here that clays are indubitably mankind's oldest example of the use of 2D materials on a massive and historic scale.

1.2 Synthesis Techniques for Two-Dimensional Materials

1.2.1 Bottom-Up Approaches:

The main technique that uses a bottom-up approach to synthesis 2D materials is chemical vapor deposition, CVD. It was used to produce of 2D layers of graphene, [54-56] h-BN,[57] and MoS_2 [58, 59]. The main advantage of CVD 2D layers over mechanical or chemical exfoliation is the larger areas obtained by the former. [60] Also, the process can be easily scaled up. For example; Bae *et al.*[61] reported on roll-to-roll production of more than 76 cm (30 inch screen size) graphene films for use as transparent electrodes. In principle, CVD also allows for the fabrication of electronic devices such as transistors.[62]

The CVD approach is of special importance when there is no known 3D layered phase for a novel 2D material. A good example is silicene, which does not exist in any 3D layered structure. Therefore, controlled deposition of silicon on a substrate -Ag(111) - was the only possible way to synthesize silicene.[63]

Growing 2D layers from solutions can be considered as another bottom-up approach. [64] However, the resulted 2D materials are more close to those produced by top-down approaches.

1.2.2 Top-Down Approaches:

1.2.2.1 Mechanical Exfoliation:

Most layered materials have relatively weak bonds such as van der Waals, or hydrogen holding the layers together. It follows that 2D layers can be readily exfoliated

from 3D crystals mechanically by cleaving the crystals against another surface. Novoselov *et. al.*[1] were the first to use this approach to separate single graphene layers from highly oriented pyrolytic graphite (HOPG), using Scotch® tape to peel the graphene layers which then were transferred to a Si wafer for extensive investigation. This approach enabled Novoselov *et. al.*[1] to investigate the electronic behavior of single layers of graphene for the first time. Another mechanical method entails rubbing the 3D materials against paper like writing with chalk on a blackboard or writing with a graphite pencil on paper.[11] Mechanical exfoliation was extended to many layered materials other than graphene including: h-BN,[11, 30] TMDs,[11, 65] MoO_3,[46, 66] and hydrated WO_3.[67]

Although this technique is simple, it is difficult scale up. Also, the lateral size of the 2D layer produced by this technique is limited by the size of the parent 3D crystal. Finally, this approach works only for weakly bonded layered materials.

1.2.2.2 Chemical Exfoliation:

Chemical exfoliation of 3D layered materials is used for the production of a wide range of 2D materials chemistries, as varied as graphene and its oxide,[68-71] h-BN,[30, 72] TMDs,[12, 73, 74] metal oxides and hydroxides,[13, 44, 49, 75, 76] and clays.[77-80] The main idea behind chemical exfoliation is to break the bonds between the layers by chemical, chemical-thermal (thermal treatment after chemical reaction), or chemical-mechanical (chemical reaction assisted by sonication) procedures. Most of the chemical exfoliations processes are carried out in liquids. A schematic for the different liquid exfoliation mechanisms is shown in Figure 6.[81]

The most widely used method entails, intercalating of a material or compound between the layers that ultimately results in their separation from each other. An example for that approach is intercalating potassium, K, between the graphene layers then exposing the potassium intercalated graphite to water or ethanol.[82] The vigorous reaction between the intercalated K and water results in separating the graphene layers from each other.

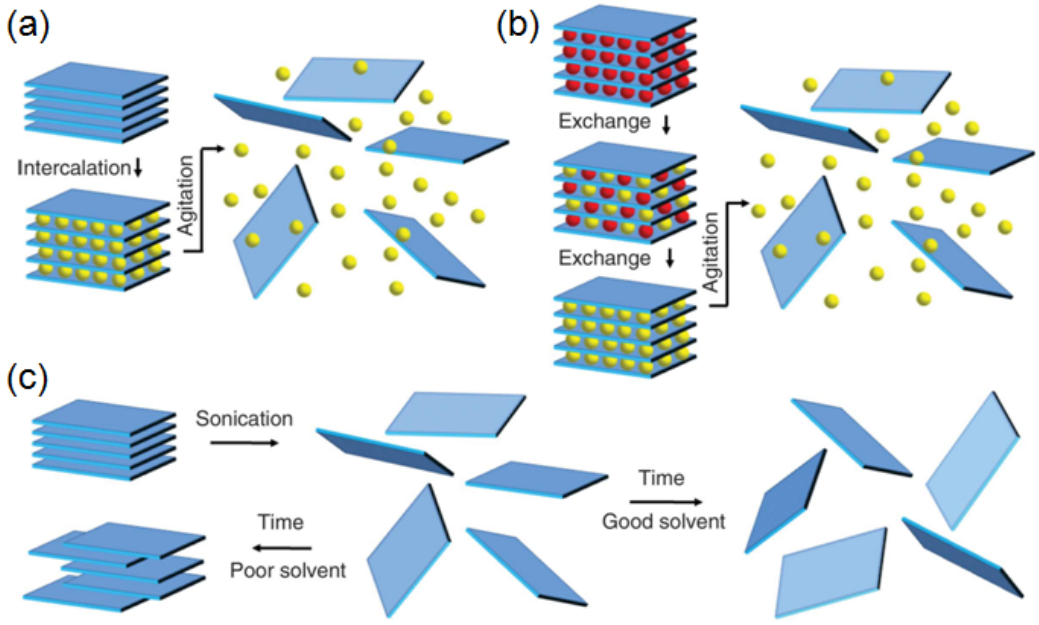

Figure 6: Schematic for the different liquid exfoliation mechanisms (a) Intercalation followed by agitation, (b) chemical modification by exchanging the compound that is between the layers by other intercalants followed by agitation, and, (c) sonication, if carried out in the right solvent, the sonicated layers will stay in suspension for a long time, if not the layers will restack. From [81] Reprinted with permission from AAAS: Science, copyright 2013.

Another example is the reaction of graphite with a mixture of acids (nitric acid, and sulfuric acid) with potassium chlorate, which results in oxidizing the graphite. Then by thermal shock (rapid heating to 1050 °C for 30 s) the intercalant decompose with a

large volume expansion that results in separating the 2D graphene oxide layers from each other.[83]

Sonication assisted exfoliation can also be used instead of thermal shock to exfoliate the intercalated graphene oxide layers.[84] Exfoliation of TMDs can be carried out by sonicating their powders in different solvents such as N-methyl-pyrrolidone or isopropanol.[12] Similarly, graphene sheets can be exfoliated by sonication in water with additives of surfactants.[85] As shown in Figure 6c, using the right solvent is very important to avoid restacking and re-agglomeration.[12]

Chemical modification of the interlayer composition is needed in some conditions where the bonds between the layers are too strong to be broken with the approaches described above.[43-45, 86] An example of this approach is the modification of the perovskite structure, $KCa_2Nb_3O_{10}$ by proton exchanging in 2M HNO_3 and then reacting with tetra (*n*-butyl)ammonium hydroxide (TBA^+OH^-) to form $TBA_\beta H_{1-\beta}Ca_2Nb_3O_{10}$ which is then easily exfoliated.[43]

Sublimation of silicon from silicon carbide, SiC, single crystals by heating it under high vacuum (~ 1.3 $x10^{-4}$ Pa) [87] or under argon [88] results in forming graphene. It is worth noting that in parallel to Novoselov *et al.* [1] early work (the work that got them Nobel Prize in physics 2010) Berger *et al.*[89] used SiC to produce few-layers graphene, and they explored their electronic properties, but their paper got published about 6 weeks after Novoselov's.

1.3 Applications of Two-Dimensional Materials

Since "*Two-Dimensional Materials*" is a diverse group of materials, they have different properties depending on their composition. Thus, it is not feasible to

summarize, or to generalize, their properties here. However, by definition all 2D materials have very high aspect ratios of lateral dimension compared to the few atoms thick layers. This 2D morphology typically results in very high specific surface areas. Another general theme is that most of 2D materials exhibit properties that differ from those of their 3D counterparts

The unique properties of 2D materials suggest that they be used in many applications. Reinforcement for polymers composites is one of the most promising applications for 2D materials, to produce light weight, high strength,[7-9] and conductive (in case of using conductive 2D material as graphene) [7, 8] composites. Due to their good electronic properties and flexibility, they can be used in transparent flexible electronic devices.[71] The large surface areas also suggest that they be used in energy storage systems such as electrochemical capacitors or supercapacitors.[5, 90] Also in LIBs, 2D materials such as graphene, [91] TMDs, [92-94] and metal oxides [95, 96] can be used as anodes materials. I'll focus here on the use of 2D materials in electrochemical energy storage and more specifically in LIBs.

Energy storage systems, in general, are a cornerstone in today's world technologies. Their applications vary from electric vehicles for transportation [97] to large scale power grid systems that are needed to manage intermittent renewable energy supply.[98] Among different energy storage systems, batteries have several advantages such as their compact size and high efficiencies.[98, 99] More specifically, LIBs have attracted most of the attention since they were first commercialized by Sony in 1991, due to their high energy density and wide voltage window.

Extensive research efforts have been dedicated to exploring and developing new anode materials for LIBs. The goal of much of the research is to develop new materials with higher capacities and lifetimes than current graphite or lithium titanate anodes. With Si insertion anodes receiving much attention in the past few years, [100-102] there is certainly a need to explore other materials.

2D materials are of special interest as host materials for metal ion batteries, due to their unique morphology that enable fast ion diffusion and offer ion insertion channels.[6] Exfoliated 2D materials with large specific surface areas, such as MoS_2,[92] and WS_2 [93] show better electrochemical performance, as anodes in secondary LIBs, compared to their un-exfoliated counterparts. For example, the capacity of exfoliated MoS_2 was found to be more than three times the capacity of pristine unexfoliated MoS_2.[92]

1.4 MAX Phases

The MAX phases are a group of unique ternary layered carbides and nitrides, with a $M_{n+1}AX_n$ composition The uniqueness of these phases comes from their unique combination of properties, as they combine both metals and ceramics characteristics.[103] For example, similar to ceramics they have high stiffness[104] and high corrosion,[105] oxidation, and creep resistance. Similar to metals, they have high electrical and thermal conductivities, in addition they are quite readily machinable.

All known *MAX* phases are layered hexagonal, with $P6_3/mmc$ symmetry, where the M layers are nearly closed packed, with *X* atoms filling the octahedral sites. The $M_{n+1}X_n$ layers are in turn interleaved with layers of A atoms.[106] In other words, the

MAX phase structure can be described as 2D layers of early transition metal carbides and/or nitrides "glued" together with layers of A element (Figure 1). The strong M-X bond has a mixed covalent/metallic/ionic character, while the M-A bond is metallic.[107] So, in contrast to other layered materials such as graphite and TMDs,[11] where weak van der Waals interactions hold the structure together, the bonds between the layers in the MAX phases are too strong to be broken by shear or any similar mechanical means. Thus, chemical modification, similar to what was discussed above for metal oxides and hydroxides, is needed to exfoliate them. This modification can be carried out by taking advantage of the differences in character and relative strengths of the M-A bonds compared with the M-X bonds. As described in this thesis the A layers can be selectively etched by chemical means without disrupting the M-X bonds.

Since the M-A bonds are weaker than the M-X bonds, heating of MAX phases under vacuum,[108] or in certain molten metals [109] at high temperatures results in the selective loss of the A element. However, because of the elevated temperature needed, de-twinning of the $M_{n+1}X_n$ layers takes place which results in formation of a 3D $M_{n+1}X_n$ rock salt structure.[110, 111] On the other hand, the use of strong etchants, such as Cl_2 gas, at temperatures above 200 °C results in etching *both* the A and M atoms, to yield carbide derived carbons or CDCs.[21, 112] It follows that, in order to selectively etch the A element, while preserving the 2D nature of the $M_{n+1}X_n$ layers, a delicate balance between temperature and the activity of the etchant needs to be maintained.

Before starting this work, it has never been reported on exfoliation of MAX phases nor synthesis of 2D transition metal carbides and/or nitrides. Thus, the aim of this work is to exfoliate the MAX phases and produce 2D layers of transition metals

carbides and/or nitrides by the selective etching of the A layers from the MAX phases. Then explore the usage of the exfoliated materials as electrode materials in LIBs.

CHAPTER 3: MATERIALS AND METHODS

In this chapter detailed description for the synthesis of the MAX phases that were used in this work, in addition to experimental details of MXenes synthesis and characterization techniques are given. Electrodes preparation, LIBs assembling, and electrochemical testing are described here as well. Finally, experimental details for the *in situ* and *ex situ* characterization techniques during lithiation and delithiation of MXenes are discussed.

3.1 Synthesis of MAX Phases

Powders, with characteristics given in Table 1, were mixed with the atomic ratios listed in Table 2 using zirconia balls in plastic jars for 12-18 h. After mixing the powders were placed in alumina crucibles and heated - with heating rates listed in Table 2 - under continuous argon, Ar, flow in a tube furnace to the soaking temperature listed in Table 2. Once the soaking temperature was reached, the furnace was held at that temperature, under Ar flow, for the soaking time listed in the same table. Then, the samples were furnace cooled down to room temperature, RT. The resulting material was in the form of a powder compact, which was then milled using titanium nitride coated milling bits to obtain powders for further study. In the cases of Ti_3AlCN, Ti_2SnC, Hf_2SnC and Ti_3SnC_2 the resulting compact was easily ground into a powder by lightly crushing it in a mortar and pestle. In all cases, the resulting powder was sieved through a -400 mesh screen such that the particle size was < 35 μm.

Two exceptions for the procedure described above are for Ti_2InC and Ta_4AlC_3. For the former titanium, Ti, and graphite, C, powders were mixed together using a ball mill for 18 h, and then the indium, In, shots were added to the mixture before heating and

distributed through the mixture using a spatula. The rest of the procedure described above was the same. For Ta_4AlC_3 after mixing the powders, instead of heating the mixture directly in the furnace it was cold pressed into cylindrical discs, 25 mm in diameter and roughly 10 mm high, using pressure of 500 MPa. The discs were placed in a tube furnace. The rest of the procedure was the same as described above.

Table 1: Sources and characteristics of powders used in this work

Powder	Purity (*wt.* %)	Particle Size	Source
Titanium	99.5	-325 mesh	Alfa Aesar, Ward Hill, MA, USA
Vanadium	99.5	-325 mesh	Alfa Aesar, Ward Hill, MA, USA
Chromium	99.0	-325 mesh	Alfa Aesar, Ward Hill, MA, USA
Niobium	99.8	-325 mesh	Alfa Aesar, Ward Hill, MA, USA
	99.8	-325 mesh	Atlantic Equipment Engineers, Bergenfield, NJ, USA
Zirconium	99.5	-50 mesh	Atlantic Equipment Engineers, Upper Saddle River, NJ, USA
Hafnium	99.6	-325 mesh	Alfa Aesar, Ward Hill, MA, USA
Tantalum	99.97	-325 mesh	Alfa Aesar, Ward Hill, MA, USA
Aluminum	99.5	-325 mesh	Alfa Aesar, Ward Hill, MA, USA
Tin	99.8	-325 mesh	Alfa Aesar, Ward Hill, MA, USA
Indium	99.99	Shots 3 mm	CERAC Inc., Milwaukee, WI, USA
Silicon	99.0	-325	Alfa Aesar, Ward Hill, MA, USA
	NA	- 1250	Elkem, Oslo, Norway
Graphite	99.0	-300 mesh	Alfa Aesar, Ward Hill, MA, USA
AlN	99.0	-1250 mesh	Sigma Aldrich, St. Louis, MO, USA
TiC	99.0	NA	Johnson Matthey Electronic, NY, USA
	99.0	NA	Alfa Aesar, Ward Hill, MA, USA
VC	99.0	-325mesh	Alfa Aesar, Ward Hill, MA, USA
Ti_2AlC	> 92 *wt.* %	-325 mesh	Kanthal, Sweden
Ti_3SiC_2	> 95 *wt.* %	-325 mesh	Kanthal, Sweden
Ti_2SC	> 95 *wt.* %	-325 mesh	Kanthal, Sweden

Table 2: Summary of starting compositions, and synthesis parameters of max phases used in this work

Order	MAX Phase	Starting Composition (atomic ratio)	Soaking Parameters		
			Heating Rate, °C/min	Soaking Temp., °C	Soaking Time, h
211	$Ti_2AlC_{0.85}$	TiC : Ti : Al 0.85 : 1.15 : 1.05	10	1400	4
	Ti_2AlN	Ti : AlN 2.0 : 1.0	10	1500	2
	V_2AlC	V : Al : C 2.0 : 1.3 : 1.0	5	1500	4
	Cr_2AlC	Cr : Al : C 2.0 : 1.1 : 1.0	5	1400	1
	Nb_2AlC	Nb : Al : C 2.0 : 1.1 : 1.0	5	1600	4
	Ta_2AlC	Ta : Al : C 1.0 : 1.6 : 1.0	10	1500	1
	Ti_2SnC	Ti : Sn : C 2.0 : 1.0 : 1.0	10	1250	2
	Ti_2InC	Ti : In : C 2.0 : 1.0 : 1.0	10	1300	2
	Hf_2SnC	Hf :Sn : C 2.0 : 1.0 : 1.0	10	1450	2
	Hf_2InC	Hf :In : C 2.0 : 1.0 : 1.0	5	1300	2
	$(Ti_{0.5},V_{0.5})_2AlC$	Ti : V : Al : C 1.0 : 1.0 : 1.3 : 1.0	5	1450	2
	$(Ti_{0.5},Nb_{0.5})_2AlC$	Ti : Nb : Al : C 1.0 : 1.0 : 1.2 : 1.0	10	1500	1
	$(V_{0.5},Nb_{0.5})_2AlC$	V : Nb : Al : C 1.0 : 1.0 : 1.3 : 1.0	5	1550	2
	$(Nb_{0.8}Zr_{0.2})_2AlC$	Nb : Zr : Al : C 1.5 : 0.5 : 1.1 : 1.0	5	1600	4
312	Ti_3AlC_2	Ti_2AlC : TiC 1.0 : 1.0	10	1350	2
	Ti_3AlCN	Ti : AlN : C 3.0 : 1.0 : 1.0	10	1500	2
	Ti_3SnC_2	Ti : Sn : C 3.0 : 1.0 : 2.0	10	1600	4
	$(V,Cr)_3AlC_2$	V : Cr : Al : C 1.5 : 1.5 : 1.2 : 2.0	10	1550	2
	$(Ti,V)_3AlC_2$	Ti : V : Al : C 1.5 : 1.5 : 1.3 : 2.0	5	1450	2
413	Ta_4AlC_3	Ta : Al : C 4.0 : 1.75 : 3.0	10	1500	1

In some cases, MAX phases powders (-325 mesh) were milled further using a temperature controlled attrition mill (Union Process Inc., Akron, Ohio, USA) with a stainless steel chamber that was maintained at 0 °C during milling. Milling was carried out using stainless steel balls in an ethanol medium, and a speed of 700 rpm for 4 h. After

milling, the powders were separated from the stainless balls and the ethanol was allowed to evaporate in air at RT.

3.2 Chemical Treatments of MAX Phases:

Several chemical treatments were carried out on different MAX phases in attempts to etch the A-group layers. They can be categorized in three main groups: 1) molten salt treatments; 2) non-aqueous fluorination treatments, and, 3) wet chemical treatments.

3.2.1 Molten Salt Treatments:

Both powder and bulk Ti_2AlC samples were used. For the bulk sample, a stoichiometric mixture of Ti, Al_4C_3 (99%, Alfa Aesar, Ward Hill, MA, USA) and graphite (99%, Alfa Aesar, Ward Hill, MA, USA) powders was mixed and hot pressed for 4 h under vacuum at 1600 ºC under a load corresponding to a stress of 40 MPa. The resulting sample was predominantly single phase and fully dense.

Roughly 10 g of Ti_2AlC powder (Table 1) were mixed with ≈ 30 g of LiF powder (99%, Alfa Aesar, Ward Hill, MA, USA) and heated to 900 °C for 2 h in air in a platinum, Pt, crucible. After cooling, the resultant powder was investigated by a XRD Siemens D500 diffractometer. To induce preferred orientation, the resulting powders were cold pressed to 1 GPa into ≈ 300 μm thin, 2.5 cm diameter disks.

Bulk samples were also immersed in molten LiF at 900 °C for 2 h. Upon cooling, the bulk samples were cleaned by gently grinding off the solidified salt, and their surfaces were investigated by X-ray diffraction. The bulk samples were also cross-sectioned, mounted, ground, and polished - down to 1 μm - and observed under an optical microscope.

The same procedures at the same temperature were carried out on bulk and powders of Ti_2AlC using potassium fluoride, KF, powder (99%, Alfa Aesar, Ward Hill, MA, USA).

Bulk samples of Ti_3SiC_2 were treated by molten sodium hexafluoroaluminate (cryolite), Na_3AlF_6 (97.8%, Alfa Aesar, Ward Hill, MA, USA) by immersing them in the later at 1000 °C for 2, or 4 h in air. Heating was carried out in a Pt crucible. After cooling to RT, the same procedure for cleaning and preparing the samples for characterization, used in the LiF case, was carried out.

3.2.2 Fluorination Treatments:

The following MAX phases, Ti_2AlC, Ti_2SC, Ti_3AlC_2, and Ti_3SiC_2 were treated using by liquid anhydrous hydrogen fluoride (A-HF) at different temperatures. Another set of samples was treated with a 5 % fluorine, F_2, gas, the balance is nitrogen, at 200 °C. The treatments were carried out by F2ChemTech (Fluorine Chemistry and Technology LLC, Allentown, PA, USA). The sources and characteristics of the Ti_2AlC, Ti_2SC and Ti_3SiC_2 powders can be found in Table 1, and the synthesis conditions for the Ti_3AlC_2 powders can be found in Table 2. In all the cases, -325 mesh powders were used. For the A-HF treatment, 10 g of each MAX phase powder listed in Table 3 was placed in a reactor before immersing in a liquid A-HF with the molar ratio listed in the same table.. The reactor was then heated to the onset temperatures and times listed in Table 3. The onset temperatures were determined by carefully increasing the temperature from RT and monitoring gas evolution.

Table 3: Anhydrous HF treatment conditions and the amount of anhydrous HF (A-HF) used for each MAX phase

MAX Phase	*Wt.* of A-HF in g that was used per 10 g of MAX	A-HF : MAX Molar Ratio	Onset temperature, °C	Time, h
Ti_2AlC	37	~ 25	55	2
Ti_2SC	36	~ 25	100	1
T_3AlC_2	32	~ 31	100	1
Ti_3SiC_2	32	~ 31	75	1

3.2.3 Wet Chemical Treatments:

The source and concentration of the as-received reagents (aqueous acids and bases), used to treat the MAX phases, are listed in Table 4. In some cases reagents were used in as received concentrations, in other cases they were diluted by deionized (DI) water. When the as received concentration was given as a range, the average of this range rounded to the nearest integer and assumed to be the concentration of that compound. For example, in case of HF, 50 *wt.* % was used to represent the as received concentration. A mixture of HNO_3:HCl with a 1: 3 molar ratio (aqua regia) was also used to treat some MAX phases.

Table 4: Sources and concentrations of the reagents used in the wet chemical treatments of max phases

Name (Chemical Formula)	Source and as Received Concentration in *wt.* % (the rest is H_2O)
Hydrochloric Acid (HCl)	Fisher Scientific, Fair Lawn, NJ, USA. 37 %
Nitric Acid (HNO_3)	Alfa Aesar, Ward Hill, MA, USA. 68-70 %
Sulfuric Acid (H_2SO_4)	Fisher Scientific, Fair Lawn, NJ, USA. 93-98 %
Hydrofluoric Acid (HF)	Fisher Scientific, Fair Lawn, NJ, USA. 48-51 %
Sodium Hydroxide (NaOH)	VWR, Radnor, PA, USA. 50 %

In general, handling acids or bases require extra caution considering their risks on human health. Thus, all safety precautions should be taken very seriously. All reactions were carried out in a chemical fume hood with a good ventilation system. Special cautions were taken for handling HF.

The wet chemical treatments were carried out by immersing the MAX phase powders (-325 mesh, and in some cases -400 mesh) in a reaction vessel. The latter comprised a plastic jar with a lid that had a hole in it to vent gas products. The reaction vessels were not filled to more than 1/3 of their volume, to avoid overflow of the reaction products. Following safety regulations, the reaction vessels were placed in a secondary container during the experiments. Since some reactions were strongly exothermic, some of the reactions were quite aggressive. Thus, whenever a new reaction was tried, a small amount of MAX phase powder (< 0.1 g) was added initially to the solution in order to test aggressiveness of the reaction. Then, small portions of the powder were added slowly with intervals of more than 1 minute to avoid excessive heat buildup. The maximum ratio of MAX phase to chemical reagent was 1:10 by weight. After adding the MAX phase powder to the reaction vessel a magnetic stir bar was added and the vessel was closed and placed on the stirrer for a prespecified time, after which the content of the reaction vessel was transferred to plastic centrifuging vials and centrifuged using a centrifuging machine (HERMLE Z 400, Labortechnik GmbH, Wehingen, Germany) at 3500 rpm for 1 h. The supernatant was then decanted from the vials.

Fresh DI water was added to the vials that were in turn shaken well to re-suspend the settled sediment, and the centrifuging and decanting steps were repeated till the pH of the decanted liquid reached ≈ 5. Lastly, the wet sediment was immersed in ethanol in a wide-mouth jar and allowed to dry in air at RT. After drying, the weight (*wt.*) loss % was calculated as following:

$$\boldsymbol{wt.loss}\ \% = \frac{\boldsymbol{wt.before\ any\ treatment - wt.after\ the\ treatment}}{\boldsymbol{wt.before\ any\ treatment}} \times \mathbf{100}. \qquad (1)$$

3.3 Post MXene Synthesis Treatments

3.3.1 Vacuum Annealing:

Vacuum annealing was carried out using a custom made vacuum furnace (Solar Atmospheres, USA). Samples were outgassed in the furnace at RT, under a vacuum of ~$1.3x10^{-4}$ Pa. The temperature was then ramped - at a rate of 300 °C·h^{-1} - to the soaking temperature and held at that temperature for certain times, before furnace cooling to RT.

3.3.2 Delamination of MXenes:

For delaminating the exfoliated $Ti_3C_2T_x$ (the T_x stands for mixed terminations of O, OH, and/or F in MXenes) particles, dimethylsulfoxide, DMSO (≥ 99.7 *wt.* %, Fisher Scientific, Fair Lawn, NJ, USA), was used. After stirring of the $Ti_3C_2T_x$ powders with DMSO for 18 h at RT, the colloidal suspension was centrifuged to separate the DMSO intercalated powder from the excess DMSO. After decantation of the supernatant, DI water was added to the residue in a *wt.* ratio of $Ti_3C_2T_x$ to DI water of 1:500. After bath sonication of the suspension for 6 h, the powder was filtered using a porous anodic aluminum oxide membrane filter (47 mm diameter, 0.2 μm pore size, Whatman Anodisc) and oven dried overnight in an oven at ~ 70 °C. The resulting film was comprised of delaminated flakes, henceforth referred to as d-$Ti_3C_2T_x$ and/or MXene "paper".

3.4 General Materials Characterization Techniques

X-ray diffraction, XRD, patterns were obtained with powder diffractometers using Cu K_α radiation, The step scans varied from 0.02 to 0.04° 2θ and 1 s per step. Over the span of 4 years two different diffractometer were used: a Siemens D500, Bruker

AXS, Karlsruhe, Germany and a Rigaku SmartLab, Tokyo, Japan. Silicon, Si, powder was added to some samples as an internal standard to calibrate the diffraction angles and the instrumental peak broadening. In order to obtain highly oriented samples for XRD along the {000*l*} planes, powders were cold pressed, CP, at 450-1000 MPa into thin discs. This was of special importance in case of MXenes, since the layers are highly disordered and they give a very high noise to peak ratio. Only after pressing the layers became more ordered and useful information such as *d*-spacing and peaks broadening were extracted from the XRD patterns. In some cases, pressing the powders by hand using a flat glass slide was sufficient enough to orient the layers.

An optical microscope, OM (S8AP0, Leica Microsystems Inc., Bannockburn, IL, USA) in transmitted light mode was used to investigate the transparency of some of the produced materials.

A scanning electron microscope, SEM (Supra 50VP, Zeiss, Oberkochen, Germany) equipped with an energy-dispersive X-ray, EDX, spectrometer (Oxford Inca X-Sight, Oxfordshire, UK) was used to investigate the chemical compositions and particles' morphologies.

Transmission electron microscopy, TEM (FEI, Tecnai G2 TF20UT FEG, The Netherlands) operating at 200 kV was used for high-resolution imaging and selected area electron diffraction, SAED. A multi-scan CCD digital camera was used to capture the images. Elemental analysis in the TEM was carried out using an ultra-thin window X-ray energy dispersive spectrometer. Electron energy loss spectra, EELS, were obtained using a FEI Tecnai G2 TF 20 UT field emission gun TEM operated at 200 kV with 0.19 nm point resolution and 0.7 eV energy resolution for EELS. Also, another TEM, (JEOL

JEM-2100, Akishima, Japan) using an accelerating voltage of 200 kV was used in this work. Specimens for TEM analysis were prepared by suspending powders in isopropanol, sonicating for 5 min, and placing a drop on a 200 mesh lacey-carbon-coated copper grid (LC200-Cu, Electron Microscopy Sciences, Hatfield, PA, USA). The elemental compositions were determined using an EDX analyzer, (AMETEK/EDAX Genesis EDAX Inc., Mahwah, NJ, USA), mounted on the TEM.

To investigate the changes in surface area, gas sorption analysis was carried out (Autosorb-1, Quantachrome Instruments, Boynton Beach, FL, USA) using nitrogen, N_2, and Ar adsorbates at 77 K. Prior to the analysis, the samples were outgassed under vacuum at 200 ºC for 48 h. The adsorption isotherms of the different gases at 77 K were analyzed and used to calculate the specific surface area (SSA) using the Brunauer-Emmet-Teller (BET) equation.[113] P/P_0 values between 0.05 and 0.10 were used to calculate the SSA.

X-ray photoelectron spectroscopy (XPS)[1] was used to characterize the chemical state of the particles after treatment. For some samples, AXIS Ultra DLD (Kratos Analytical Ltd, Manchester UK) instrument was used employing a 800 μm monochromatic Al-kα X-ray to irradiate the surface of the sample. Photoelectrons were collected by a 180° hemispherical electron energy analyzer. Samples were analyzed at a 90° takeoff angle between the sample surface and the path to the analyzer. High-resolution spectra were taken at a pass energy of 20.00 eV, with a step size of 0.1 eV. For other samples, a PHI VersaProbe 5000 (Physical Electronics, Inc, Chanhassen, MN, USA) instrument was used employing a 100 μm monochromatic Al-kα X-ray to irradiate

[1] XPS measurements were taken by Dr Kevin Cook and Mr. Josph Halim, and they helped in analyzing the results when peak fitting was possible.

the sample surface. Photoelectrons were collected by a 180° hemispherical electron energy analyzer. Samples were analyzed at a 45° takeoff angle between the sample surface and the path to the analyzer. High-resolution spectra were taken at a pass energy of 11.75 eV and with a step size of 0.05 eV.

The Nb_2C spectra were taken after the sample was sputtered with an Ar beam operating at 3.8 kV and 150 μA for 10 min; the V_2C spectra were taken without Ar sputtering. All binding energies were referenced to that of free carbon at 284.5 eV.

The inelastic neutron scattering (INS)[2] experiments were performed using the fine-resolution Fermi chopper spectrometer SEQUOIA at the Spallation Neutron Source (SNS) at the Oak Ridge National Laboratory (ORNL).[114] INS measurements were made at a temperature, T, of 7 K with four incident neutron energies: E_i = 50, 160, 250 and 600 meV, to provide high energy resolution (about 1-3% of E_i) in a wide range of energy transfer 2 meV < E < 550 meV. The collected neutron scattering data were transformed from time-of-flight and instrument coordinates to the dynamical structure factor $S(q,E)$ using the software package mantidplot [115]. A generalized vibrational density of states $G(E)$ was then calculated. The INS spectra from the empty container were also measured under the same conditions and subtracted from the sample data.

Sheet resistances of cold pressed, CP, discs were measured using a four-probe technique (Cascade Probe Station CPS-1303-24 with 4-point probe head Alessi C4S-57, Cascade Microtech, Inc., Beaverton, USA).

Contact angle measurements of deionized water (DI) were also performed at RT using the sessile drop technique. 10 μL water drops were placed on the surfaces of CP

[2] INS measurements were carried out by Dr. Alexander I Kolesnikov at Oak Ridge National Laboratory (ORNL). Reprinted with permission from *J. Am. Chem. Soc.*. DOI: 10.1021/ja501520b. Copyright 2014 American Chemical Society.

discs. The contact angles were measured from photographs taken with a CCD camera yielding an accuracy of approximately ±3°.

In case of Ti_2AlC treated with A-HF, Fourier transform infrared spectroscopy, FTIR (Perkin Elmer Spectrum 100 FTIR, Shelton, CT, USA) was used to analyze the gaseous reaction products during the A-HF treatment. After the treatment, the crystal structure was determined from XRD using TOPAS4 (Bruker AXS, Karlsruhe, Germany).[3] Based on the fundamental parameter approach, FPA,[116] the instrumental parameters (*e.g.*, broadening, offset) were derived from measurements of a Si reference. From the diffractograms, the peak positions and intensities were extracted via whole-pattern fitting with the Pawley method [117] yielding results in agreement with the LeBail method.[118] Based on the space group identified from indexing, the derived unit cell dimensions and peak intensities were used for structure solutions, based on whole-profile fitting simulated annealing.[119]

Theoretical calculations[4] were performed by density functional theory, DFT, using the plane-wave pseudo-potential approach, with ultrasoft pseudopotentials and Perdew Burke Ernzerhof exchange - Wu-Cohen correlation functional, as implemented in the CASTEP code in Material Studio software (Version 4.5). A 8x8x1 Monkhorst-Pack grid and planewave basis set cutoff of 500 eV were used for the calculations. Exfoliation was modeled by first removing Al atoms from the Ti_3AlC_2 lattice. Exposed Ti atoms located on the bottom and top of the remaining Ti_3C_2 layers were saturated by OH or F groups followed by full geometry optimization until all components of the residual forces became less than 0.01 eV/Å. Equilibrium structures for exfoliated layers were determined

[3] Solving the crystal structure was carried out by Dr Volker Presser.
[4] DFT calculations for modeling the resulted structure after etching Al from Ti_3AlC_2 were carried out by Dr Murat Kurtoglu.

by separating single Ti_3C_2 layers by a 1.2 nm thick vacuum space in a periodic supercell followed by the aforementioned full geometry optimization. Band structures of the optimized materials were calculated using a k point separation of 0.015$Å^{-1}$.

3.5 Thermodynamic Calculations

Thermodynamic calculations were carried out using FactSage 6.2 (Gibbs minimization software). EpH calculations module was used. For all calculations, a closed system was assumed. All calculations were carried out at pressure of 1 atm. The construction of isothermal E *vs.* pH (Pourbaix) diagrams was carried out on two metals systems (M and A metals in different MAX phases) at 298.15 K in water that contains fluorine, F with molality of 0.1.

3.6 Electrodes Preparation and LIBs Assembly

To investigate how the various materials resulting from this work behaved as electrode materials in LIBs, they were prepared as follows:. Cast electrodes were made by mixing the MXene powders with 10 *wt.* % acetylene carbon black (Alfa Aesar, Ward Hill, MA, USA) and 10 *wt.* % polyvinylidene fluoride, PVDF, (Alfa Aesar, Ward Hill, MA, USA) dissolved in 1-methyl-2-pyrrolidinone (purity 99.5%, Alfa Aesar, Ward Hill, MA, USA). The mixture was spread on a copper, Cu, foil (thickness 0.025mm, purity 99.8%, Alfa Aesar, Ward Hill, MA, USA) using a doctor blade and dried at 70 ºC for 12 – 18 h in a drying oven. After dying the film, 12 mm diameter discs were punched and weighed. To determine the weight of the active material 5 uncoated Cu discs with 12 mm diameter were weighed and the average weight was calculated and subtracted from the

weight of each punched disc of the coated Cu foil. The electrodes' loading was in the range of 2-8 mg/cm^2.

Other electrodes forms were used as well such as CP electrodes and additives free MXene paper electrodes. Before placing these electrodes in the glove box for testing, they were heated to 120-140 ºC for 12-18 h under a mechanical vacuum (<1.3 kPa).

A stainless steel coin cell (CR-2016, MTI, Richmond, CA, USA) configuration was used to test the electrochemical performance. Lithium, Li, metal foils (thickness 0.75 mm, purity 99.9%, Alfa Aesar, Ward Hill, MA, USA) were used as counter electrodes. The Li foil was rolled using a glass rod to reduce its thickness and to remove any surface oxide layers. Borosilicate glass fibers (thickness: 0.26 mm, pore size: 1.6 μm, Whatman GF/A, Buckinghamshire, UK) were used as separators. The electrolyte used was 1M lithium hexafluorophosphate $LiPF_6$, solution in a 1:1 by weight mixture of ethylene carbonate (EC) : diethyl carbonate (DEC). The purities of $LiPF_6$, EC, and DEC were 99.8 *wt.* %, 99.95 *wt.* % and 99.98 *wt.* %, respectively (Novolyte Technologies, Independence, OH, USA). Stainless steel spacers 0.2 mm thick (EQ-CR20-Spacer304-02, MTI, Richmond, CA USA) were used in some cases to increase the height of the stack to achieve the 1.1 mm height that results in optimum contact in the coin cells. The latter were assembled using a crimping machine (EQ-MSK-110, MTI, Richmond, CA USA) in an Ar-filled glove box, fitted with a circulating system that kept the O_2 and H_2O contents to < 1 ppm.

3.7 Electrochemical Testing

For electrochemical testing, three different potentiostats/galvanostats were used. A VMP3 and MPG2 (Biologic, Knoxville, TN, USA) were used for cyclic volatmmetry (CV) and galvanostatic charge-discharge cycling (GC). A BT-2143-11U (Arbin, College Station, TX, USA) was used only for GC testing as a battery cycler to find the capacity and study the cyclabilities at different rates.

3.7.1 Cyclic Volatmmetry Testing:

Cyclic volatmmetry (CV) tests were conducted by applying a potential sweep rate of 0.2 mV/s, over a certain voltage range, while recording the resulting current, *I*, versus potential, *V*. Plotting *I vs. V* gives cyclic voltammograms. For easier comparisons between the various electrodes, *I* was divided by the electrode's weight to obtain a specific current.

3.7.2 Galvanostatic Cycling Testing:

Galvanostatic cycling (GC) testing was carried out by a applying constant current, *I*, between certain two voltage limits. Once the voltages reached their set limits the current direction was reversed to reach the other voltage limit, *etc.* Meanwhile, the functional dependence of *V*, on time, *t*, was recorded to obtain the voltage profiles for each electrode material. The specific capacities, Q in mA·h/g of the active materials in each electrode for certain cycle was then calculated according to

$$Q = (I \times t)/m \tag{2}$$

where *I* is the constant current applied in mA, *t* is time needed to reach the voltage limit for a certain cycle in h, and *m* is mass of the active material in g. The number of ions, *y*,

stored in the host material to achieve a certain specific capacity, *Q,* is calculated, based on Faraday's law *viz*:

$$y = (Q \times 3.6 \times M)/(z \times F); \quad (3)$$

Q is the specific capacity (mA·h/g), M is molecular weight of the host material in g/mol (*e.g.* for $Ti_3C_2(OH)_2$ it is about 201.6 g/mol), z is valence of the ions (*e.g.* for Li and Na, z = 1, while for Ca, z = 2), and F is Faraday constant (96485 C/mol). The 3.6 factor is used to convert the units of Q from mA·h/g to A·s/g in order to match Faraday's constant units.

Since the maximum theoretical capacities of the MXenes are not well determined so far, the cycling rate is determined experimentally by finding the time needed to reach a voltage limit during GC. For example, if using a certain current results in fully charged or discharged cells in 2 h, then the cycling rate is assumed to be *C*/2; if it takes 0.5 h the cycling rate is 2 *C* and so on.

3.8 *In Situ* and *ex situ* Characterization Technique During Electrochemical Lithiation and De-lithiation of MXene:

3.8.1 In situ X-ray Diffraction:[5]

Electrochemical *in situ* X-ray diffraction patterns of Ti_2CT_x powders were collected on a Brucker D8 diffractometer using a Cu Kα radiation (λ = 1.5406 Å) in the range 2θ = 7-40° with a 2θ step of 0.02°. The sample was placed in a Swagelok-type cell equipped with a beryllium, Be, window which also acted as a current collector, allowing in-situ X-Ray recording (cell from LRCS, Amiens University, France). The scans were

[5] *In situ XRD* was carried out at Université Paul Sabatier, Toulouse, France. Reproduced with permission from *J. Electrochem. Soc.*, **159**, A1368 (2012). Copyright 2012, The Electrochemical Society.

recorded every insertion/extraction yield of $x = 0.2$ upon lithiation and delithiation, using a rate of $C/10$.

3.8.2 In situ Dilatometer:

For the *in situ* dilatometry study during lithiation and delithiation of $Ti_3C_2T_x$, an electrochemical dilatometer (ECD-nano-DL, EL-Cell GmbH, Hamburg, Germany) was used with resolution < 5.0 nm. The electrode used in this study was prepared as described above in section 3.6 (page 30). In other words it was cast on Cu foil. The electrolyte used was 1M $LiPF_6$ in EC:DEC 1:1, *wt.* ratio. The dilatometer was assembled in an Ar filled glove box with O_2 and H_2O contents of < 1 ppm. After assembly, the dilatometer was placed in a temperature controlled chamber and the temperature was maintained at 20 ± 1 °C for electrochemical cycling that was carried out using a potentiostat (VSP-300 Biologic, Knoxville, TN, USA). The displacements during electrochemical cycling were recorded with a data acquisition system (34972 A, Agilent Technologies Inc, Santa Clara, CA, USA). The initial thickness of the electrode was measured using a SEM to be about 60 μm.

3.8.3 In situ Ti K-edge X-ray Adsorption Spectroscopy: [6]

In situ Ti K-edge X-ray adsorption spectra (XAS) spectra were measured in transmission mode at beamline X19A at the National Synchrotron Light Source (NSLS) of the Brookhaven National Laboratory (BNL) using a Si(111) double-crystal

[6] *In situ* XAS measurements were carried out by Dr. Xiqian Yu, Dr. Kyung-Wan Nam, and Dr. Xiao-Qing Yang at Brookhaven National Lab (BNL). Reprinted with permission from *J. Am. Chem. Soc.*. DOI: 10.1021/ja501520b. Copyright 2014 American Chemical Society.

monochromator, detuned to 45% of its original maximum intensity to eliminate high-order harmonics.

A standard 2032 coin cell, with two 3 mm diameter coaxial holes drilled on either side, was used for the *in situ* XAS measurements. The holes were sealed with polyimide (Kapton®) tape. The electrode was fabricated by slurry coating of a mixture of $Ti_3C_2T_x$: carbon black:polyvinylidene fluoride (PVDF) binder in a 8:1:1 weight ratio, onto a 6 μm thick Cu current collector.

The *in situ* XAS spectra were continually collected during lithiation/delithiation in an electrolyte of 1.2 M $LiPF_6$ dissolved in ethylene carbonate/dimethyl carbonate (3:7, vol.%). During lithiation, a current density of 36.5 $mA \cdot g^{-1}$, based on the active material, was used. At 76.8 $mA \cdot g^{-1}$, the discharging current density was higher in order to complete the measurement in the limited beam time available. Reference spectra of a metallic Ti foil were simultaneously collected with the corresponding in situ spectra for energy calibration. X-ray Absorption Near Edge Structure (XANES) and Extended X-ray Absorption Fine Structure (EXAFS) data were analyzed using the ATHENA software package.[120] The photoelectron energy origin, E_0, was chosen at the first inflection point of the absorption edge jump. The extracted EXAFS signal, $\chi(k)$, was weighted by k^2 to emphasize the high-energy oscillations and then Fourier-transformed in k-ranges of 3.0 ~ 10.0$Å^{-1}$ using a Hanning window function to obtain the magnitude plots of the EXAFS spectra in R-space (Å). The Fourier-transformed peaks were not phase corrected, and thus the actual bond lengths are approximately 0.2-0.4 Å longer.

3.8.4 Ex Situ X-ray photoelectron spectroscopy (XPS):

Electrodes of $Ti_3C_2T_x$ films on Cu foil were prepared and assembled in the coin cells configurations as described above in section 3.6 (page 30). The cells were lithiated/delithiated using MPG2 potentiostats/galvanostats with a current density of ~ 37 mA/g of active material. Five different cells were lithiated/delithiated as follows: i) lithiated from open circuit voltage (OCV) to 1.0 V; ii) lithiated from OCV to 0.005 V; iii) lithiated from OCV to 5.0 mV then delithiated to 3 V; iv) cycled between 3 V and 5 mV for eight cycles and stopped at 5 mV, and, v) cycled between 3 V and 5 mV for eight cycles and stopped at 3 V.

The coin cells were then moved directly to an Ar filled glove box and disassembled. Another electrode was soaked in the electrolyte (1M $LiPF_6$ in EC:DEC 1:1 *wt.* ratio) for 48 h at RT in the glove box. The electrodes were rinsed by immersing them in DEC, dried in the glove box and placed onto the XPS sample holders. The latter were transferred from the glove box to the XPS machine in a vessel filled of Ar that was sealed in the glove box. The time it took to transfer the sample holder from the vessel to the XPS vacuum chamber was less than 30 s.

XPS instrument (VersaProbe 5000) was used in this study, employing monochromatic Al-kα X-rays with a 100-μm spot size. Photoelectrons were collected by a 180° hemispherical energy analyzer at a 45° takeoff angle between the sample surface and the path to the analyzer. Survey spectra were taken at a pass energy of 117.4 eV and with a step size of 0.500 eV. High-resolution spectra were taken at a pass energy of 23.5 eV and with a step size of 0.05 eV. Spectra were taken before and after the samples were

sputtered with an Ar beam operating at 4 kV and 7 μA for 10 minutes. All binding energies were referenced to that of aliphatic carbon at 284.8 eV.

CHAPTER 4: SYNTHESIS OF TWO-DIMENSIONAL TRANSITION METAL CARBIDES "*MXenes*"

4.1 Synthesis of MAX Phases

The MAX phases were used, in this study, as MXene precursors. Thus, it was preferred to have them in powder form to accelerate the extraction of A-group layers. Since there are very few reports on synthesis of MAX phases in the powder form, optimizing the pressureless synthesis conditions to synthesize loosely compacted MAX phases with the highest possible purity was needed.

In many cases in order to avoid formation of transition metal binary carbides, the initial concentration of the A-group element was slightly higher than stoichiometric. XRD was used to determine the resulting phases. The conditions listed in Table 2 resulted in the formation of MAX phases with the least amounts of secondary phases.

4.2 Unsuccessful Attempts to Exfoliate MAX Phases

4.2.1 Molten Salt Treatments:

A detailed discussion of the materials characterization after the molten salt treatments of the MAX phases by KF and cryolite is given in Appendix A. Briefly, by immersing Ti_2AlC or Ti_3SiC_2 in molten salt, the A-group atoms diffused out of the structure and reacted with the molten salt leaving behind the $M_{n+1}X_n$ layers. As shown in schematic in Figure 7, after the Al etching from Ti_2AlC at 900 °C in LiF, de-twining of the hexagonal structure occurred forming the cubic phase (with rock salt structure). The de-twining was thermally activated. We published the results on reacting Ti_2AlC with LiF in a paper titled "On the Topotactic Transformation of Ti_2AlC into a Ti–C–O–F Cubic Phase by Heating in Molten Lithium Fluoride in Air." [121]

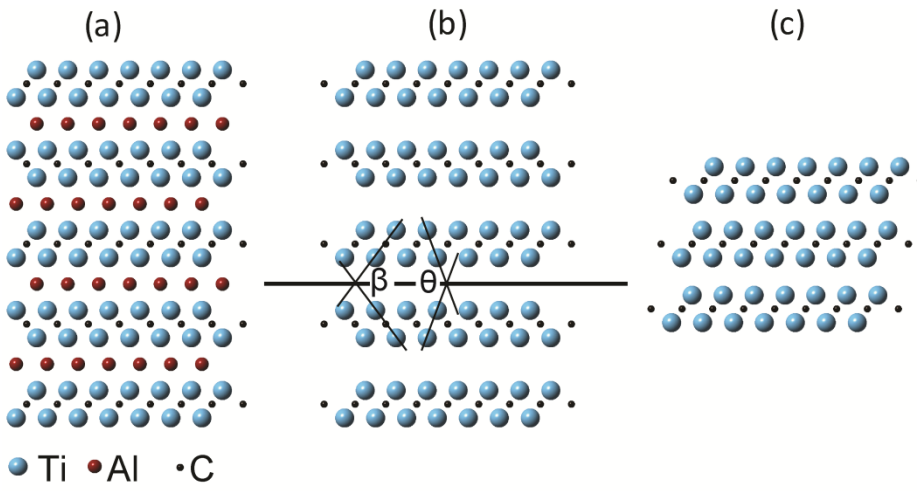

Figure 7: Schematic describing the process of transformation of Ti_2AlC in Ti_2C (a) Ti_2AlC $(1\bar{2}10)$ plane; (b) same as (a) but after removing the Al from the structure and, (c) same as (b) but after de-twinning of every other Ti_2C slab. Angles θ and β in (b) are the angles between de-twined planes. Reproduced with permission.[121]

From the aforementioned work, it became clear that the selective etching of A-group atoms from MAX phases is feasible, but needed to be done at relatively low temperatures to avoid the conversion of the the $M_{n+1}X_n$ 2D layers into a cubic – rock salt - 3D structure.

4.2.2 Fluorination Treatments:

Chlorination of MAX phases at relatively high temperatures (300-1100 °C)[122] results in etching both the M and A atoms out from MAX phase resulting in a highly porous amorphous carbon called carbide derived carbon, CDC. [112] Batisse and *et al.*[123] showed that, successful fluorination of titanium carbide can be carried out at much lower temperatures (130-300 °C) than what is used in chlorination.

Fluorinating different MAX phases powders – *viz.* Ti_2AlC, Ti_2SC, Ti_3AlC_2, and Ti_3SiC_2 - using 5% F_2 at 200 °C, did not result in any changes in their structure, as shown in the XRD patterns (Appendix A). Treating the same MAX phases powders with A-HF

using the conditions listed in Table 3 resulted in two different outcomes. In the case of Ti_2SC, Ti_3AlC_2 and Ti_3SiC_2, XRD patterns (Appendix A) evidenced the formation of titanium trifluoride, TiF_3 that coexisted with unreacted MAX phases. In case of Ti_3SiC_2 and Ti_2SC, it is most likely that silicon and sulfur formed gaseous fluoride phases such as silicon fluoride (SiF_4) and sulfur tetrafluride (SF_4) were formed during treatment. For Ti_3AlC_2, it is not clear what happened to Al, possibly formed amorphous phase that was not detected by XRD. While in case of Ti_2AlC that was treated with A-HF at 55 °C for 2 h, a new phase was formed. The XRD, SEM, TEM, SAED, results together with the crystal structure solution *via* simulated annealing, confirmed the formation of a new nanocrystalline ternary metal fluoride, Ti_2AlF_9, with a trigonal structure belonging to the R3 space group. More information about this new phase can be found in our published paper titled "Synthesis of a new nanocrystalline titanium aluminum fluoride phase by reaction of Ti_2AlC with hydrofluoric acid." [124] Small amount of Ti_2AlF_9 was observed also in case of Ti_3AlC_2.

Although forming a new nanocrystalline ternary fluoride phase may be useful for many applications, this process did not result in the exfoliation of the MAX phases

4.2.3 Wet Chemical Treatments:

As listed in Appendix B treating MAX phase powders with several aqueous reagents, resulted in either their dissolution with a leftover of unreacted phase, or no reaction. An exception was using HF. During the reaction of Ti_2SnC powder (- 400 mesh) with 50 % HF at RT, for ≈ 12 h, a strange sound was noted. Sound of metal beads hitting each other (sound like cabasa instrument) was coming from the reaction vessel. After 24 h, the reaction was stopped and the products were washed, large metallic beads (~1-3

mm) in addition to small amount of powders were observed. As shown in Figure 8a, the XRD of this mixture showed Sn metal in addition to unreacted Ti_2SnC. The weight loss after the reaction was ~ 40%. Considering that Sn in Ti_2SnC represents ~ 52 *wt.* %, it is reasonable to conclude that both Ti and C were dissolved in the suspension, and the Sn agglomerated forming metal beads.

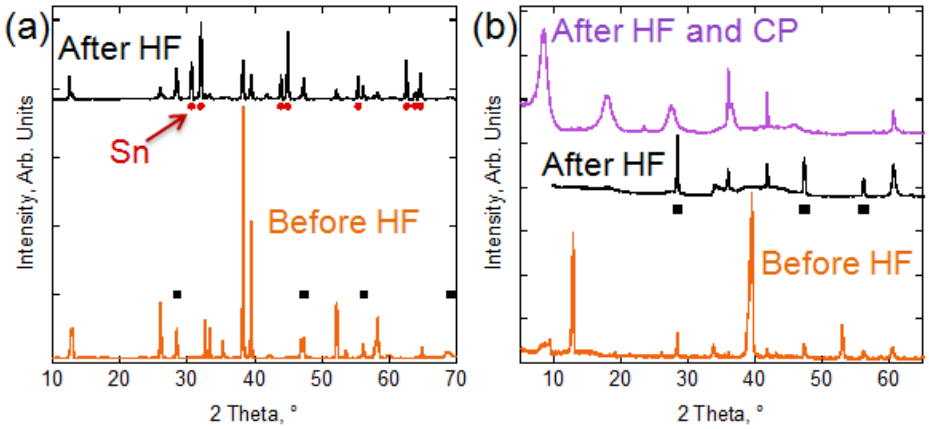

Figure 8: XRD patterns for (a) Ti_2SnC before and after treatment with 50% HF at RT for 24 h. (b) Ti_2AlC before and after treatments with 50% HF at RT for 5 minutes, the top XRD patterns is the for CP sample after HF treatment. The black squares represent the peaks positions of Si that was used as an internal reference, the red circles in figure a represent the peaks position for Sn [PDF# 04-0673].

Immersing Ti_2AlC powders (Kanthal, Sweden) in 50% HF at RT resulted in an aggressive exothermic reaction accompanied with extensive amounts of gas evolution, When the reaction was stopped after 5 minutes, by adding 300 mL of DI water to the reaction vessel, the color of the resulting powders after washing and drying turned much darker than the starting Ti_2AlC powder (the color turned from dark grey to black).

The weight loss was ~ 90%. EDX of the powders after the reaction showed significantly less Al than the stoichiometric Al ratio in Ti_2AlC. In addition to Ti, Al, and C, both O and F were detected with the following the atomic ratios: Ti : Al : C : O : F

were ~ 1.0 : 0.06 : 0.6 : 0.6 : 1.2, respectively. Also, the C to Ti ratio was higher than the stoichiometric ratio in Ti_2AlC. However, it is not suggested to rely on EDX to quantify C, because it may come from sources other than the sample itself.

Figure 8b shows that all the peaks related to Ti_2AlC vanished after the HF treatment. Only TiC peaks at 2θ ~ 35.98°, 41.8°, and 60.6°, present as an impurity in the as received MAX phases powders, and very low intensity peaks of TiC can be observed in the XRD of the as received powder (bottom pattern in Figure 8b). Also, it has never been reported on crystallization of crystalline titanium carbide at RT. Thus, it can be concluded that TiC was in the starting materials but its amount was very small relative to the MAX phase and its peaks were not relatively strong. Only after cold pressing the treated powders at 1 GPa, the XRD (top pattern in Figure 8b) were new broad peaks at 2θ ~ 8.49°, 17.96°, 27.56°, and 36.43° appear Since those peaks appeared only after pressing, it is reasonable to conclude that this phase has certain preferred orientations. Assuming a hexagonal structure (the same as the MAX phase), the preferred orientation would be along {000*l*} plane, and those peaks would be corresponding to (0002), (0004), (0006) and (0008). The resulted average *c*-lattice parameter, *c*-LP, based on this assumption is ~ 19.92 Å.

This *c*-LP value , is closer to the *c*-LPs of the 312 MAX phases rather than their 211, counterparts. For example, the *c*-LP of Ti_3AlC_2 was reported to be 18.487Å [125] while that of Ti_2AlC is 13.364 Å.[18] This observation, together with the fact that only 10 *wt.*% remained after the reaction, which is almost the same amount of Ti_3AlC_2 that existed as a secondary phase in the as-received Ti_2AlC powder, directed my attention

toward the former. In other words, I reached surmised that under those conditions, all the Ti_2AlC dissolved and that the leftover is the product of reacting Ti_3AlC_2 with HF.

This hypothesis was proven to be true by treating pure Ti_3AlC_2 powders in HF (see next section). Although this experiment was a failed experiment to exfoliate Ti_2AlC (since all of it dissolved), it was the key experiment for discovering an entire new family of 2D materials that we labeled "*MXenes*" discussed in the rest of the thesis.

4.3 Synthesis of Ti_3C_2 –Based MXene

When - 400 mesh Ti_3AlC_2 powders (synthesis parameters listed in Table 2) were immersed in 50% HF, the reaction was much less aggressive than what observed in the case of Ti_2AlC. Bubbles, presumed to be H_2, were observed during the reaction, suggesting a chemical reaction. After 2 h, the reaction was stopped and the powder was washed using DI water. The weight loss was negligible - it was almost zero. EDX analysis of the resulting powders showed a significant reduction in the Al content, and a concomitant increase in the O and F concentrations. The Ti : Al : C : O : F atomic ratio was ~ 3.0: 0.1 : 1.4 : 1.7 : 1.9. This implies that the Al layers were replaced by oxygen (*i.e.* OH) and/or fluorine, F. A SEM image of a Ti_3AlC_2 particle after HF treatment (Figure 9a) shows how the basal planes fan out and spread apart as a result of the HF treatment compared to as synthesized Ti_3AlC_2 (Figure 9b). This open morphology, after HF treatment, resembles exfoliated graphite. [82]

Figure 9d-e show the XPS spectra for Ti and Al before and after HF treatment. The Ti 2p region of the as synthesized Ti_3AlC_2 (top spectrum in Figure 9d) showed the existence of Ti-Al,[126] Ti-C and Ti-O peaks in locations that were quite similar to what

was reported for Ti_3AlC_2 by Myhra *et al.*[127]. After HF treatment (bottom spectrum Figure 9d), the Ti-Al peak vanished, while Ti-C signal was still there and the Ti-O shifted to higher binding energy, which could represent a Ti with a higher oxidation state or Ti-F.[128] The peak in the Al spectrum before HF treatment around 73 eV (top spectrum in Figure 9e) can be assigned for Al in Ti_3AlC_2.[127] This peak almost vanished while another broad peak around 75 eV, that can be assigned to mixture Al of oxide and fluoride, appeared after HF treatment.

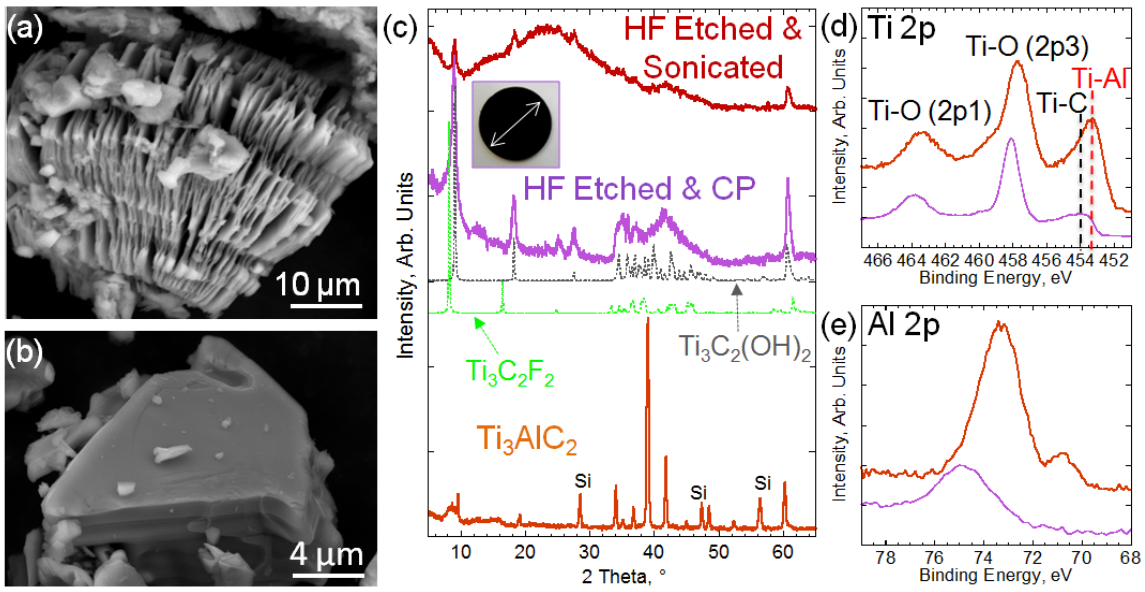

Figure 9: Analysis of Ti_3AlC_2 before and after HF treatment. SEM images of, (a) sample after HF treatment and (b) sample before any treatment. (c) XRD pattern for Ti_3AlC_2 before any treatment, simulated XRD patterns of $Ti_3C_2F_2$ and $Ti_3C_2(OH)_2$, measured XRD patterns of cold pressed Ti_3AlC_2 after HF treatment, and after HF and sonication. The inset shows a cold pressed 25 mm disk after HF treatment. XPS spectra of (d) Ti 2p, and. (e) Al 2p for Ti_3AlC_2 before (top spectra) and after HF treatment (bottom spectra). Reproduced with permission from[129] and [130].

Based on the results discussed above it is reasonable to conclude that the following simplified reactions occur when Ti_3AlC_2 is immersed in HF:

$Ti_3AlC_2 + 3HF \rightarrow AlF_3 + 3/2\ H_2 + Ti_3C_2$ (1)

$Ti_3C_2 + 2H_2O \rightarrow Ti_3C_2(OH)_2 + H_2$ (2)

$Ti_3C_2 + 2HF \rightarrow Ti_3C_2F_2 + H_2$ (3)

Reaction (1) is essential and is followed by reaction (2) and/or (3). For simplicity, $Ti_3C_2T_x$, - where T_x represents the chemical groups that replaced the A- layers - will be henceforth to refer to Ti_3AlC_2 after HF treatment.

When the powders were cold pressed to 1 GPa, into free-standing, 300 μm thick and 25 mm diameter discs (inset Figure 9c), their XRD patterns showed that most of the non-basal plane peaks of Ti_3AlC_2 - most notably the most intense peak of $(10\bar{1}4)$ at ≈ 39° - disappear (purple curve in Figure 9c). On the other hand, the {000*l*} peaks, such as the (0002), (0004) and (0006), broadened, lost intensity, and shifted to lower angles compared to their location before treatment. The *c*-LP shifted from 18.55 Å to 19.57 Å upon the reaction.

To identify the peaks we simulated XRD patterns of hydroxylated, *viz.* $Ti_3C_2(OH)_2$, (grey curve in center of Figure 9c) and fluorinated, $Ti_3C_2F_2$, structures (lemon green curve in center of Figure 9c).[7] Clearly, both were in good agreement with the XRD patterns of the pressed sample (purple curve in Figure 9c); the agreement was better with the former. The disappearance of the most intense diffraction peak of Ti_3AlC_2 at 39° and the good agreement between the simulated XRD patterns for $Ti_3C_2(OH)_2$ and the experimental results provides strong evidence of the formation of the latter. Using the Scherrer formula[131] the average domain size, in the [000l] direction, after treatment is estimated to be 11±3nm, which corresponds to roughly ten $Ti_3C_2(OH)_2$ layers.

[7] The DFT calculations were carried out by Dr Murat Kurtoglu.

Geometry optimization of the hydroxylated and fluorinated structure resulted in 5% and 16% expansion of the original Ti_3AlC_2 lattice, respectively. If Al were simply removed, and not replaced by functional groups, the DFT optimization caused the structure to contract by 19 %, which is not observed. This is quite reasonable since the exposed Ti atoms on the MXene surfaces are unstable in air and should be satisfied by suitable termination.

Ultrasonication of the reaction products in methanol for 300 s and dropping few droplets of the suspension on a glass slide that was dried at RT in air afterward, resulted in significant weakening of the XRD peaks and the appearance of an amorphous broad band around 24° (top pattern in Figure 9c). The corresponding TEM images of a sonicated sample are shown in Figure 10.

TEM analysis of HF treated and sonicated $Ti_3C_2T_x$ flakes (Figure 10 a,b) showed them to be quite thin and electron transparent since the carbon grid is clearly seen below them. This fact strongly suggests a very thin foil, especially considering the high atomic number of Ti. The corresponding SAED (inset in Figure 10b) shows the hexagonal symmetry of the basal planes. EDX of the same flake showed the presence of Ti, C, O, and F with no Al. Figure 10c,d show cross-sections of single- and double-layer MXene sheets. Figure 10e,f show high-resolution TEM micrographs and a simulated structure of two adjacent OH-terminated Ti_3C_2 sheets, respectively. The experimentally observed interplanar distances and angles are found to be in good agreement with the calculated structure. The exfoliated layers can apparently also be rolled into conical shapes (Figure 10g); some are bent to radii of < 20 nm (Figure 10h).

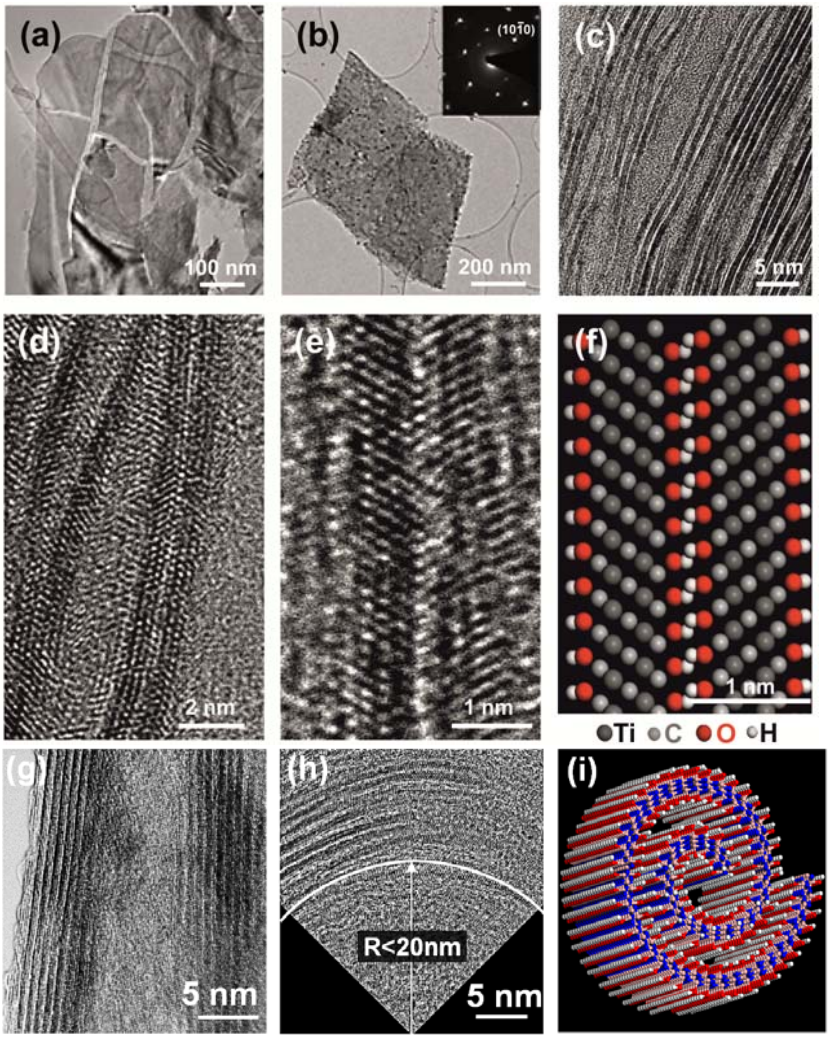

Figure 10: Exfoliated MXene nanosheets. (a) TEM micrographs of 2D nanosheets of Ti-C-O-F. (b) Exfoliated 2D nanosheets; inset SAED shows hexagonal basal plane. (c) Single and double layer MXene sheets. (d) HRTEM image showing the separation of individual sheets after sonication. (e) HRTEM image of bilayer $Ti_3C_2(OH)_xF_y$. (f) Atomistic model of the layer structure shown in e). (g) Nanoscroll of about 20 nm in outer diameter. (h) Cross-sectional TEM image of a scroll with an inner radius of less than 20 nm (i) Schematic for OH terminated Ti_3C_2 scroll. Reproduced with permission.[129]

Figure 11 summarize the process of synthesis of 2D layers of $Ti_3C_2T_x$ from Ti_3AlC_2. Immersing the latter in HF resulted in etching the Al (reaction1) and replacing it by mixture of O, OH, or/and F terminations (reactions 2 and 3). Sonicating the HF treated sample in methanol resulted in breaking the bonds between the $Ti_3C_2T_x$ layers resulting in delaminated 2D layers. We labeled those 2D layers "*MXene*" to denote that fact that

the A-group atoms were etched from the parent MAX phase and the suffix *ene* to emphasis their similarities to graphene.

Note that if the Al atoms had been replaced by C atoms, the concomitant formation of strong Ti-C bonds - as when, for example, Ti_3SiC_2 reacts with cryolite at 900 °C - [110] exfoliation would not have been possible. It follows that the reaction must have resulted in a solid in which the Ti-Al bonds are replaced by much weaker hydrogen or van der Waals bonds. This comment notwithstanding, the EDX results consistently show the presence of F in the reaction products implying that, as noted above, the terminations are most likely a mixture of F and OH.

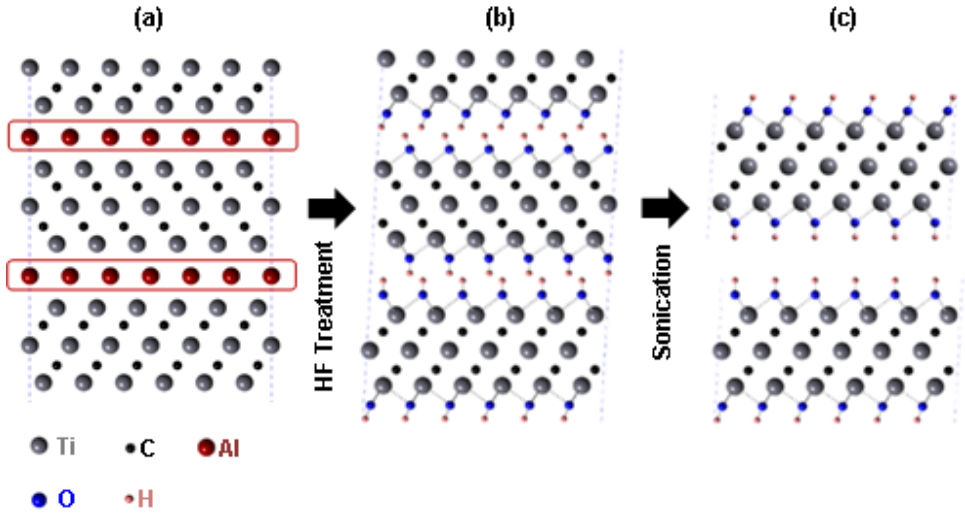

Figure 11: Schematic of the exfoliation process for Ti_3AlC_2. (a) Ti_3AlC_2 structure. (b) Al atoms replaced by OH after reaction with HF. (c) Breakage of the hydrogen bonds and separation of nanosheets after sonication in methanol.[129]

4.4 Synthesis of Other MXenes:

To discover whether $Ti_3C_2T_x$ was just a single, new 2D material or if – like the MAX phases - it is a member of a larger family the same approach, *viz.* HF etching, was explored for other MAX phases. The phases listed in Table 5 were selected to represent the different subgroups in the MAX phases family, *i.e.* 211, 312, 413, solid solutions on M sites and carbonitrides.

If a MAX phase is fully transformed to MXene, all but the {000*l*} peaks in the XRD patterns will weaken or vanish, especially in the case of the thinner M_2X structures. Furthermore, the (000*l*) peaks broaden and downshift to lower angles, an indication of a larger *c*-LP. Also noteworthy is that the *c*-LP value (column 8 in Table 5) of each MXenes varies slightly from one batch to another, depending on the drying conditions.

In case of incomplete conversion, MAX phase peaks coexist with the MXene {000*l*} peaks. Along the same lines, and primarily because XRD peak intensities tend to fade with increasing degree of exfoliation (decreasing number of layers in the MXene lamellas), XRD cannot be used to accurately quantify the fraction of unreacted MAX phase in a sample. Instead EDX was used to quantify the A:M atomic ratio. In a fully converted sample, this ratio would be zero. However, this method tends to overestimate the MAX phase concentration because, in addition to its presence in the MAX phase, the A element could also be present in the MXene samples in the form of salts containing the A element, if the etching products are not completely removed during washing.

Table 5: Process conditions, weight loss, *c*-lattice parameters for MXene synthesis from MAX phases, and domain size along [0001]. Also listed are the *c* values of the parent MAX phase.

	MAX	MXene	RT etching conditions		*wt.* loss %	*c* lattice parameter, Å		Δ *c*-LP, Å	Domain size along [0001], nm
			HF conc. %	Time h		MAX	MXene[§]		
211	Ti_2AlC*	Ti_2CT_x	10	10	40	13.6	15.04	1.44	6
	V_2AlC*	V_2CT_x	50	8[a] 90	45 40	13.13	23.96 19.73	10.83 6.60	14 10
	Nb_2AlC	Nb_2CT_x	50	90	~ 0	13.88	22.34	8.46	5
	$(Ti_{0.5},Nb_{0.5})_2AlC$	$(Ti_{0.5},Nb_{0.5})_2CT_x$	50	28	20	13.79	14.88	1.09	5
	$(Ti_{0.5},V_{0.5})_2AlC$*	$(Ti_{0.5},V_{0.5})_2CT_x$	50	4[a] 19	40 35	13.41	20.40 20.76	6.99 7.35	7 7
	Mo_2GaC*	Mo_2CT_x	50	96	NA	13.17	20.21	7.04	15
312	Ti_3AlC_2	$Ti_3C_2T_x$	50	2	~ 0	18.42	20.51	2.09	11
	$(V_{0.5},Cr_{0.5})_3AlC_2$*	$(V_{0.5},Cr_{0.5})_3C_2T_x$	50	69	30	17.73	24.26	6.53	28
	Ti_3AlCN	Ti_3CNT_x	30	18	20	18.41	22.28	3.87	7
	$(Ti_{0.5},V_{0.5})_3AlC_2$	$(Ti_{0.5},V_{0.5})_3C_2T_x$	50	18	~ 0	18.15	21.73[b] 27.85	3.58 9.70	5 10
413	Ta_4AlC_3	$Ta_4C_3T_x$	50	72	10	24.08	28.43[b] 30.34	4.35 6.26	18 38
	Nb_4AlC_3 [c]	$Nb_4C_3T_x$	50	90	NA	24.19	30.47	6.28	27
	$(V_{0.5},Nb_{0.5})_4AlC_3$[d]	$(V_{0.5},Nb_{0.5})_4C_3T_x$	50	33	NA	23.87	30.35	6.48	29

[§] The *c*-LP values for each MXene varies slightly from one batch to another
* Incomplete conversion from MAX to MXene, *i.e.* some unreacted MAX phase co-existed with MXene.
[a] Attrition-milled powders.
[b] The (0002) peak was deconvoluted in two distinct peaks.
[c] Nb_4AlC_3 was present as a secondary phase in the Nb_2AlC sample.
[d] $(V_{0.5},Nb_{0.5})_4AlC_3$ was present as a secondary phase in the $(V_{0.5},Nb_{0.5})_2AlC$ sample.

SEM images after HF treatment, in case of successful synthesis of MXene, showed an open morphology where the layers are clearly separated from each other compared to the unreacted powder, similar to exfoliated graphite [82] and the previously described exfoliated morphology for $Ti_3C_2T_x$. Typical SEM images for several MXenes are shown in Figure 12.

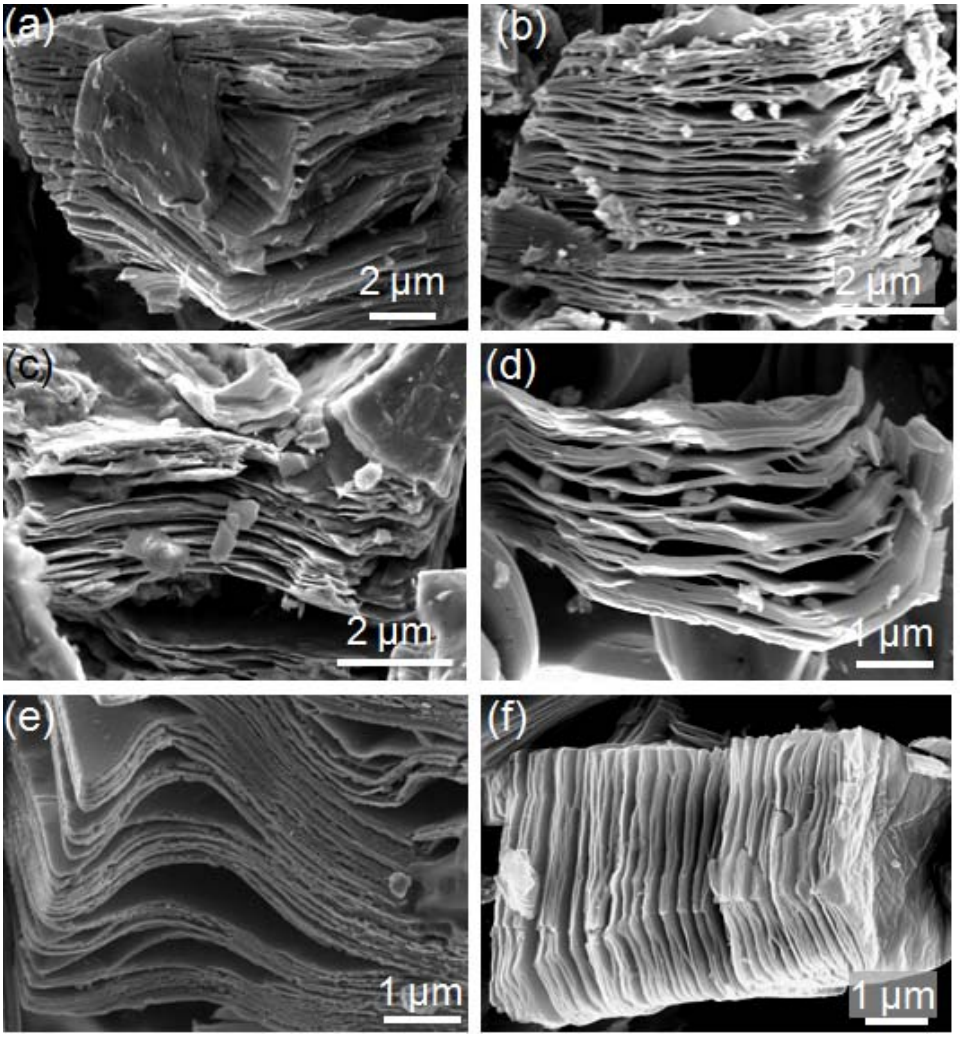

Figure 12: SEM images for, (a) Ti_2CT_x, (b) Nb_2CT_x, (c) V_2CT_x, (d) $Ta_4C_3T_x$, (e) $(Ti_{0.5},Nb_{0.5})_2CT_x$, and, (f) Ti_3CNT_x produced by HF etching for their corresponding Al containing MAX phases. Reproduced with permission: for a, d-f from [130] and for b-c from [132].

The weight losses due to HF treatment varied between 0-45%. Note that since the atomic weight of Al is close to the combined weight of atoms in $(OH)_2$, if the two are interchanged and if the resulting MXenes do not dissolve in the etchant, little weight loss is expected, as observed for some MXenes (see column 6 in Table 5). The assumption of replacing each Al atom by two surface groups is reasonable, since one Al layer glues two $M_{n+1}X_n$ layers in the MAX phases (each Al layer is shared by two $M_{n+1}X_n$ layers) so after etching, surface groups terminate the surface of each exposed MXene layer.

The etching times and HF concentrations needed to fully convert a given MAX powder depend primarily on its particle size, time, temperature, and HF concentration.[130, 133] Tuning the etching conditions is important to minimize the weight loss and maximize the conversion of MAX into MXene. Prolonged etching results in either dissolving the MXene or formation of defects, such as holes observed in Figure 13a in $Ta_4C_3T_x$. Similar, atomic defects were reported in functionalized graphene,[134] that act as nucleation sites for metal oxides which are useful in many applications.[135, 136]

In addition to providing direct evidence for defects in the 2D layers, HRTEM analysis combined with EDX or EELS, and SAED are used to give very useful information. As shown in Figure 13b, the presence of carbon in the 2D layer after HF treatment of Ta_4AlC_3 was confirmed by EELS. HRTEM SAED (Figure 13c and Figure 13d), however, show that the crystallinity of the basal planes of the MAX phases is preserved. These images confirm the hexagonal structure of the $Ta_4C_3T_x$ layers. Measurements of the *d*-spacings shown in the figure resulted in 0.269 nm and 0.155 nm for $(01\bar{1}0)$ and $(\bar{2}110)$ lattice planes, respectively. When these values are used to calculate the *a* lattice parameter, the value obtained, 3.1 Å, is in excellent agreement with that of the *a* parameter of the non-exfoliated Ta_4AlC_3 MAX phase, *viz.* 3.11 Å.[137] It is thus reasonable to conclude that the MAX crystal structure of the basal planes is maintained in the MXenes.

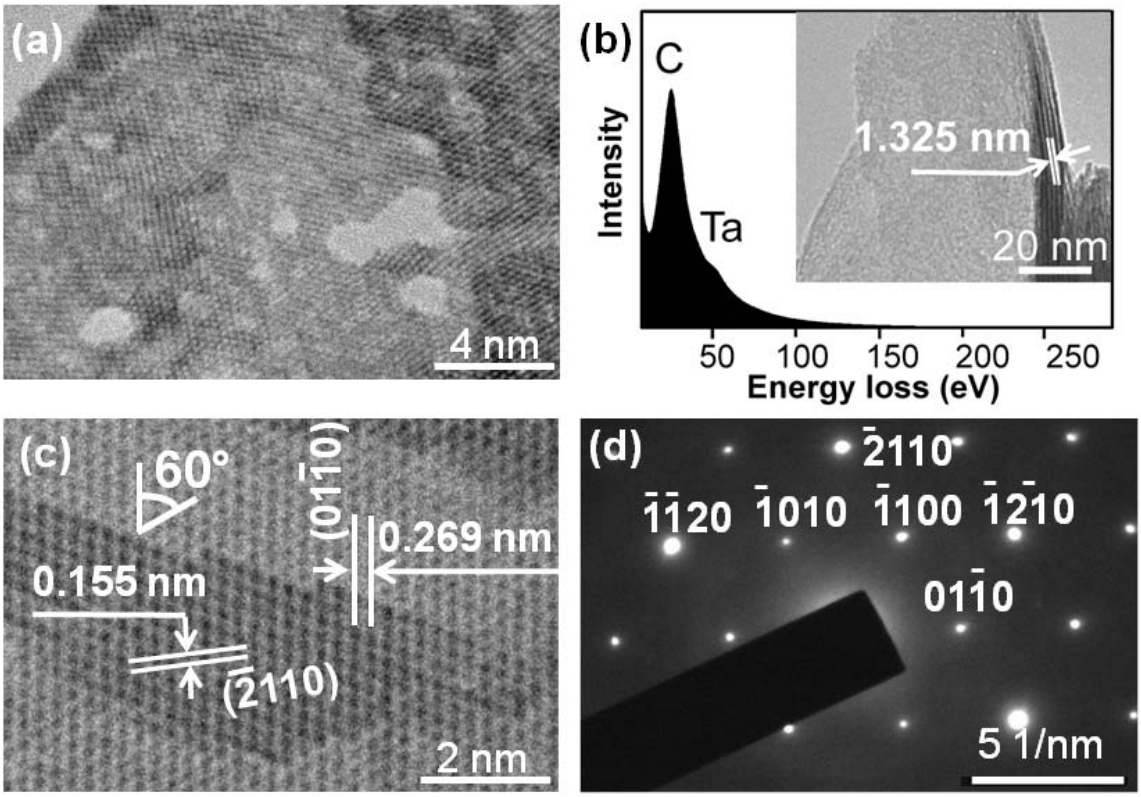

Figure 13: Electron microscopy analysis of Ta_4AlC_3 after HF treatment, (a) TEM image, (b) EELS and inset showing a low magnification TEM image, (c) HRTEM of multilayer MXene, and, (d) SAED. Reproduced with permission.[130]

TEM analysis of MXenes after sonication (Figure 14) showed thin electronically transparent layers. Their thickness can be measured only if they are edge-on or cross-sectional samples were used, as shown in Figure 14a for Nb_2CT_x.

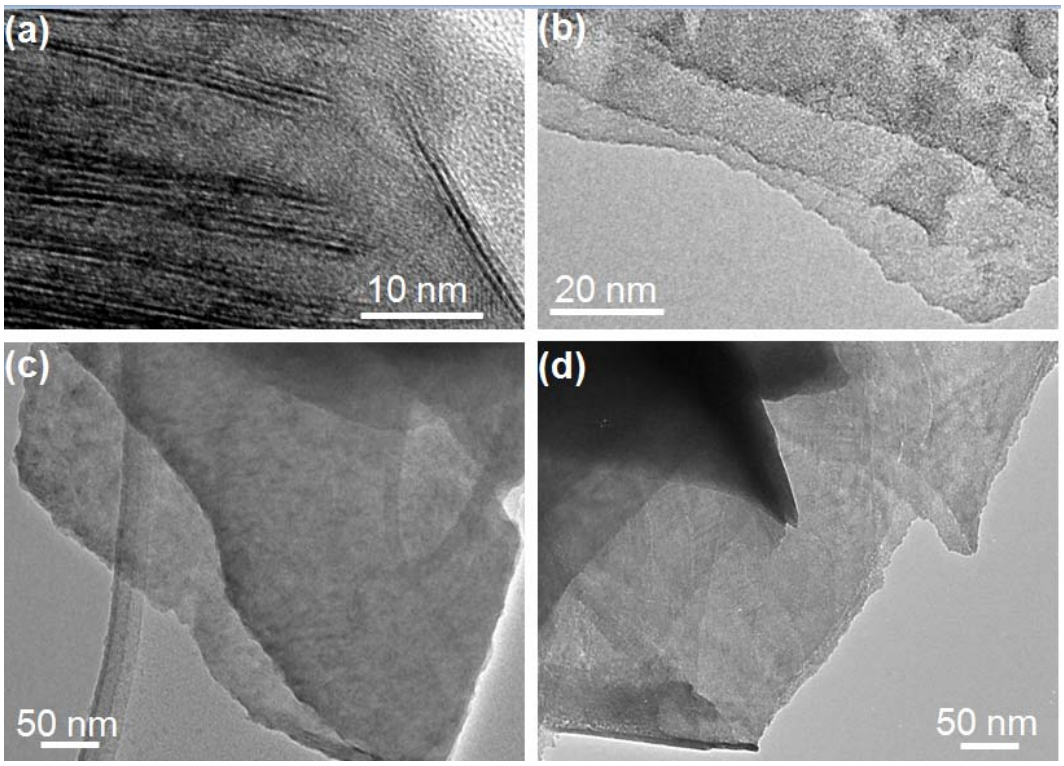

Figure 14: TEM images for (a) cross-section Nb_2CT_x layers, (b) layers of Ti_3CNT_x, (c) $(Ti_{0.5},Nb_{0.5})_2CT_x$, and (d) $Ta_4C_3T_x$ produced by HF treatment of their Al contained MAX phases. Reproduced with permission: for (a) from [132] and for (b)-(d) from [130].

Figure 15 shows that the MXene layers were not just electronically transparent, but also optically transparent under an OM in transmittance mode.

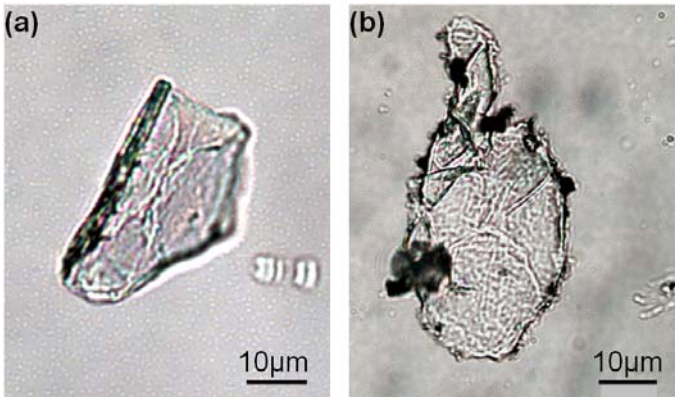

Figure 15: Transmitted light micrographs of exfoliated flakes of (a) $Ta_4C_3T_x$ and, (b) Ti_3CNT_x. Reproduced with permission.[130]

As shown in Figure 16, the nitrogen, N_2, sorption isotherms of HF treated Ti_2AlC powder (Figure 16a) and Ti_3AlC_2 (Figure 16b) powders have hysteresis loops with indications of the presence of mesopores and a shape typical for slit pores. [138] The SSA calculated using the BET equation, [113] for the HF treated Ti_2AlC was 23 $m^2 \cdot g^{-1}$; for the Ti_3AlC_2 it was ~ 8 $m^2 \cdot g^{-1}$. Those values are much higher than the as-received Ti_2AlC and Ti_3AlC_2 powders measured at ≈ 2.5 $m^2 \cdot g^{-1}$, and 1.2 $m^2 \cdot g^{-1}$, respectively.

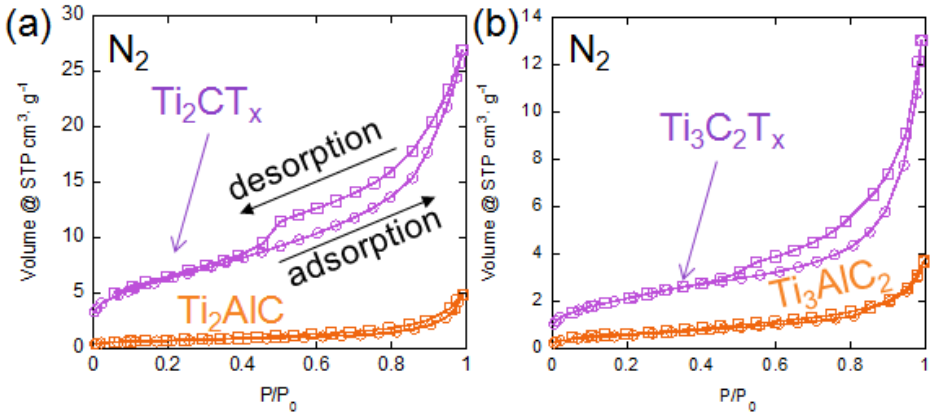

Figure 16: Nitrogen, N_2, adsorption-desorption isotherms of, (a) Ti_2AlC before and after HF treatment, (b) Ti_3AlC_2 before and after HF treatment. Circles refer to adsorption and squares refer to desorption. The bottom isotherms (orange lines) are for the MAX phase, the top ones (purple lines) are for MXene. (a) was reproduced with permission.[139]

The successful etching of the A-group element from several phases, represent the different subgroups of the MAX phase family, and subsequent exfoliation of the $M_{n+1}X_n$ layers prove that "*MXenes*" are a family of 2D materials.

4.5 Large-Scale Delamination of $Ti_3C_2T_x$:

Gardolinski and Lagaly [140] differentiated between exfoliation and delamination in clays and layered materials as follows: exfoliation is the decomposition of large aggregates into smaller particles, while delamination is the separation of the individual layers in the particle. With this definition, the as-synthesized MXene (just after HF treatment and before sonication) will be referred to as exfoliated MXene, since the MAX phase decomposed into smaller particles of multi layer MXene. From XRD, the thickness of those particles, along [000*l*] varies from 5 nm to 38 nm (see column number 10 in Table 5). After sonication and separation of the $M_{n+1}X_nT_x$ layers into single or few layers (< 10), they will be referred to as delaminated MXene. As described above in sections 4.3 and 0, the sonication of exfoliated MXene in alcohols results in delaminated layers of MXenes, but the amount of delaminated flakes was small. Thus, finding other techniques to delaminate MXenes was needed. The approach we used was through intercalation followed by sonication.

Intercalation is a well known phenomenon for many layered materials, such as graphite [141] and clays.[142] in which the bonds between the layers are not very strong. The same is true of MXenes: the weak bonds between the $M_{n+1}X_n$ layers allow for the intercalation of different species (organic, inorganic, and ionic) between the $Ti_3C_2T_x$ layers.[143, 144] In most cases, the intercalation results in an increase in the *c*-LP values. For example, the intercalation-induced changes in the *c*-LP of $Ti_3C_2T_x$, vary from 0.7 Å for sodium sulfate to 15.4 Å for dimethylsulfoxide, DMSO (Figure 17).[143, 144]

The large Δc in LP after DMSO intercalation is due to the spontaneous co-intercalation of ambient moisture. XRD patterns, taken 3 weeks after the initial DMSO

intercalation (top pattern in Figure 17), showed an even larger downshift of the (0002) peak positions corresponding to a *c*-LP of 44.8±0.1 Å. Based upon this result, combined with the observation that DMSO intercalated MXene powders are highly hygroscopic and become increasingly wet when stored in air over a few weeks, it is reasonable to assume that, over time, co-intercalation or capillary condensation of water from ambient air into the interlayer space, occurred.

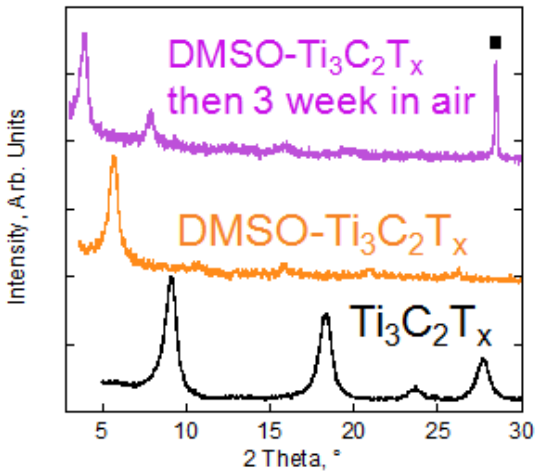

Figure 17: XRD patterns for $Ti_3C_2T_x$ (bottom black pattern), DMSO intercalated $Ti_3C_2T_x$ (middle orange pattern), DMSO intercalated $Ti_3C_2T_x$ then stored in air for 3 weeks (top purple pattern). The black square represents peak position of Si that was used as an internal reference. Reproduced with permission. [143] **Copyright 2013, Macmillan Publishers Ltd.**

This discovery, in turn, was exploited to fully exfoliate – what we term delaminate herein – $Ti_3C_2T_x$ sheets. After a weak sonication of DMSO intercalated MXene dispersed in DI water, fully delaminated – that we denote as d-Ti_3C_2 - flakes were obtained. After removal of large particles by centrifuging, the resulting aqueous colloidal solutions of MXene flakes were quite stable. The colloidal state of delaminated MXene flakes in aqueous solutions was also confirmed by the observation of the Tyndall

scattering effect when passing a red laser beam through the solution (Figure 18a). SEM images clearly showed thin, electron-beam transparent, single to a few MXene flakes precipitated from a drop of colloidal solution placed on a porous alumina membrane surface (Figure 18b).

Binder-free, MXene "paper" (inset in Figure 18c) was produced by filtering the aforementioned colloidal solution through a membrane. XRD patterns of the resulting "paper" (Figure 18c) clearly showed that the non-basal peaks at ~ 60° 2θ, vanished after delamintion. This result provides compelling evidence for the loss of order along all but the (0001) direction and consequently, full delamination. To date, the only MXene that has been successfully delaminated in large quantities is $Ti_3C_2T_x$.

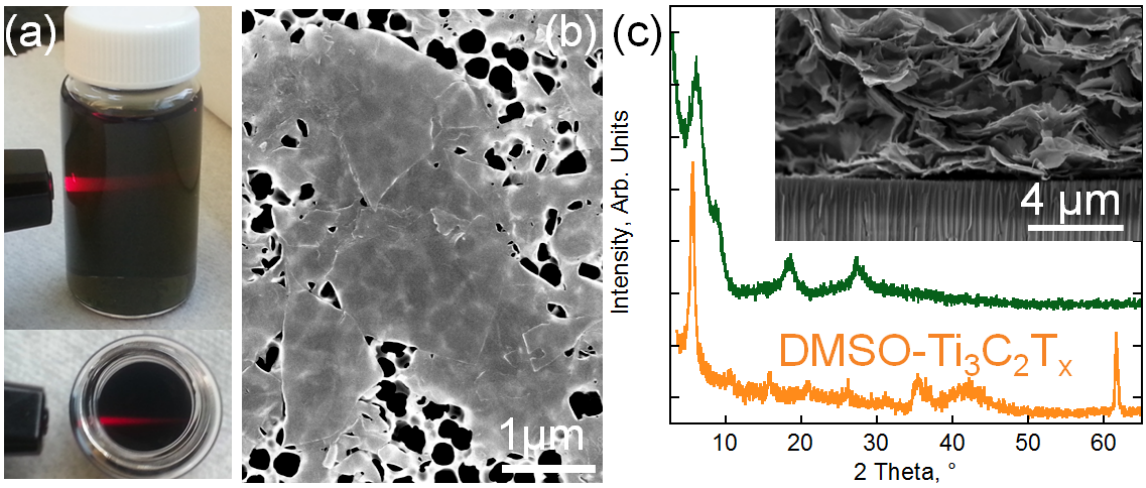

Figure 18: (a) Colloidal solution of delaminated $Ti_3C_2T_x$ showing Tyndall scattering effect of solution. (b) SEM images of $Ti_3C_2T_x$ flakes on the alumina membrane. (c) XRD patterns for DMSO intercalated $Ti_3C_2T_x$ and additive-free paper of d-$Ti_3C_2T_x$. Inset shows SEM image of an additive-free paper of delaminated $Ti_3C_2T_x$ synthesized by filtering the colloidal solution showed in (a) through the alumina membrane. Reproduced with permission[143] Copyright 2013, Macmillan Publishers Ltd.

The SSA of the MXene paper measured using N_2 was 98 $m^2 \cdot g^{-1}$, which is significantly higher than SSA before delamination. It is worth noting that the SSA of the MXene paper was higher when CO_2 and Ar (128 and 167 $m^2 \cdot g^{-1}$, respectively) were used that when N_2 was used which can be explained by the presence of small pores.

4.6 Surface Chemistry of Selected MXenes: [8]

A high-resolution XPS spectrum of the Nb_2CT_x layers in the Nb 3d region (Figure 19a) revealed the presence of photoemission which could be best fit with components corresponding to:

i) MXene, Nb_2C, (33.3% of Nb 3d photoemission; 202.8 eV, full width at half maximum, FWHM 1.2 eV, Nb $3d_{5/2}$; 205.5 eV, FWHM 1.2 eV, Nb $3d_{3/2}$),[145-147]

ii) functionalized Nb_2C and mixed oxide, $NbC_xO_yF_z$, species (35.5% of Nb 3d photoemission; 203.9 eV, FWHM 2.0 eV, Nb $3d_{5/2}$; 206.7 eV, FWHM 2.0 eV, Nb $3d_{3/2}$)[146, 148] and,

iii) oxidized Nb (31.2% of Nb 3d photoemission; 206.7 eV, FWHM 2.5 eV, Nb $3d_{5/2}$; 209.7 eV, FWHM 2.5 eV, Nb $3d_{3/2}$).[146, 148, 149]

The oxidized Nb is likely Nb_2O_5 forming a separate phase on the MXene's surfaces. The large FWHM of the peaks corresponding to $NbC_xO_yF_z$ and the oxidized Nb are likely due to the fact that a mixture of functional groups (O, OH, and F) are also present on the surface, while ~ 33.3% of the photoemission comes from Nb_2C, *i.e.* the MXene backbone.

[8] XPS measurements and analysis were carried out by Dr. Kevin Cook, and Mr. Joseph Halim

A high-resolution spectrum in the O 1s region (Figure 19b) could be fit by broad peaks (FWHM 1.6 eV) at 530.0, 531.8 and 532.4 eV. The component centered at 530.0 eV (72.6% of O 1s photoemission) is consistent with oxygen in Nb_2O_5.[147] The component centered at 531.8 eV (18.6% of O 1s photoemission) likely arises from O or OH groups bound to the surface of the MXene layers.[147] The peak centered at 532.8 eV (8.8% of O 1s photoemission) can be attributed to adsorbed water and most likely arises from water trapped between the MXene layers.[150, 151]

A high-resolution spectrum in the C 1s region (Figure 19c) was best fit by three components, the first being a low-binding energy peak corresponding to carbon in Nb_2C (37.2% of C 1s photoemission, 281.8 eV, FWHM 0.71 eV), non-stoichiometric C (*e.g.* near a defect) in Nb_2C (24.9% of C 1s photoemission, 282.0 eV, FWHM 1.1 eV) and a broad peak corresponding to adventitious contamination (37.4% of C 1s photoemission, 283.6 eV, FWHM 2.4 eV). Excluding the photoemission from the Nb_2O_5 and adventitious components, the Nb to C ratio was 2.00:0.68. The excess Nb signal is likely due to the added contribution of the mixed Nb-oxide species to the photoemission in this region.

The V_2CT_x layers were also analyzed by XPS. A high-resolution spectrum of the V 2p region (Figure 19d) revealed the presence of photoemission which could be best fit with components corresponding to:

i) unreacted V_2AlC (13.6% of V 2p photoemission; 513.4 eV, FWHM 1.5 eV, V $2p_{3/2}$; 521.0 eV, FWHM 1.5 eV, Nb $2p_{1/2}$)[151] and,

ii) oxidized vanadium (86.4% of V 2p photoemission; 516.4 eV, FWHM 2.4 eV, V $2p_{3/2}$; 523.8 eV, FWHM 2.4 eV, Nb $2p_{1/2}$).[151, 152]

The slight overestimation of the V $2p_{1/2}$ peak centered at 523.8 eV is due to overlap with the O 1s region resulting in increased background emission. It is clear though, that these data are consistent with a sample that contains both V_2C layers that are partially terminated in an oxygen monolayer, and some mixed vanadium oxide.[151]

A high-resolution spectrum in the O 1s region (Figure 19e) could be fit by broad peaks (FWHM 1.9 eV) at 529.9, 531.3 and 532.9 eV. The components centered at 529.9 eV (26.3% of O 1s photoemission) and 531.3 eV (57.5% of O 1s photoemission) are consistent the presence of a with mixed vanadium oxide (VO_x) and surface oxide groups,[151] while the peak centered at 532.9 eV (16.2% of O 1s photoemission) is again consistent with intercalated water.[150, 151]

A high-resolution spectrum in the C 1s region (Figure 19f) was best fit by four components with the first two corresponding to adventitious contamination (19.5% of C 1s photoemission, 286.1 eV, FWHM 1.5 eV; and, 61.7% of C 1s photoemission, 284.5 eV, FWHM 1.5 eV), a high-binding energy peak similar to a peak attributed to adsorbed methanol (10.1% of C 1s photoemission, 288.3 eV, FWHM 1.5 eV),[152] and – similar to Nb_2C – a low-binding energy peak (8.7% of C 1s photoemission, 281.8 eV, FWHM 1.5 eV) that corresponds to C in V_2C.[153] The large amount of contamination and low intensity of the Nb_2C signal is due to the lack of Ar sputtering. The source of the contaminant found at 287.2 eV is likely due to the ethanol used during the drying stage.

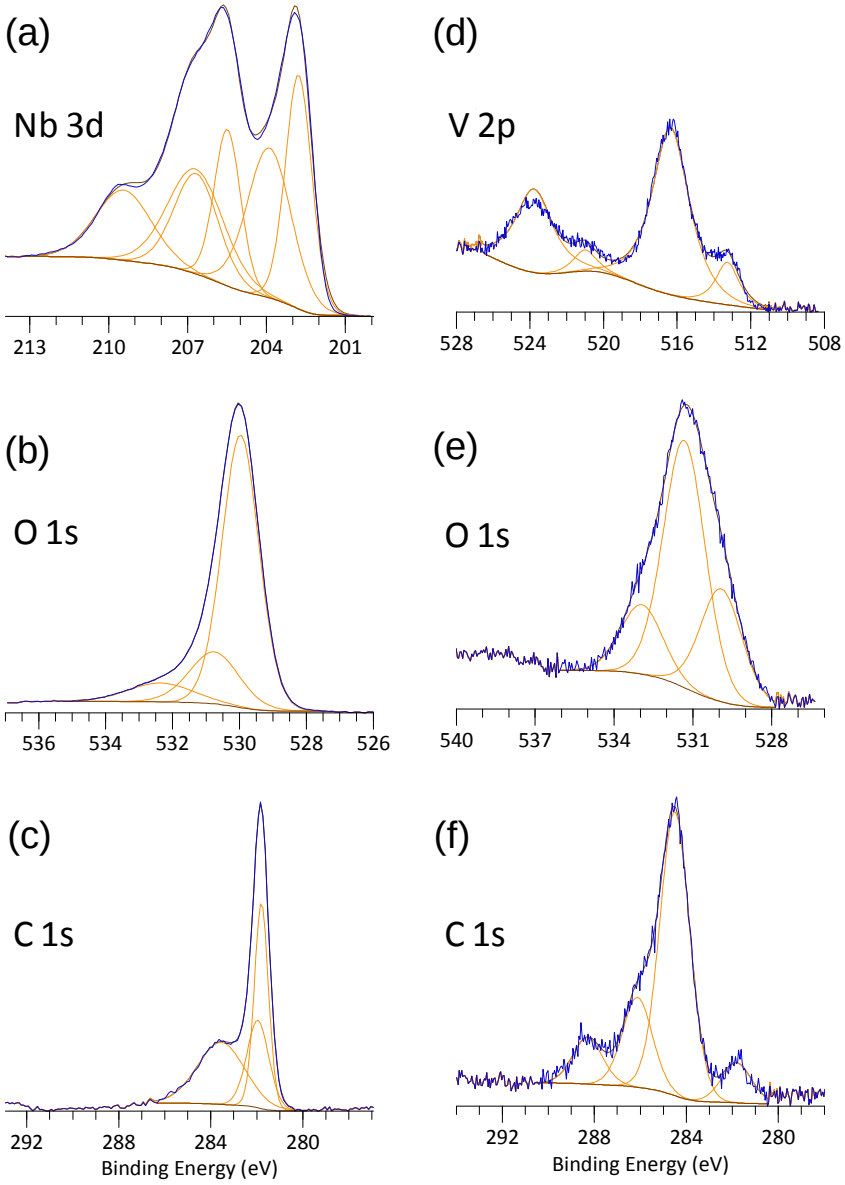

Figure 19: High-resolution XPS spectra of Nb_2CT_x films in, (a) Nb 3d region, (b) O 1s region and, (c) C 1s region, and V_2CT_x films in the (d) V 2p region, (e) O 1s region and, (f) C 1s region.[132]

4.7 Comments on Some Experimental Observations Regarding MXenes Synthesis

4.7.1 Etching Time:

Although all the MAX phases, except Mo_2GaC, listed in Table 5 contain Al as an A element, the etching conditions varied widely, a fact that most probably reflects the

different M-Al bond energies in the different MAX phases. For example, the Ti-Al and Nb-Al bond energies in Ti_2AlC and Nb_2AlC have been estimated to be 0.98 eV and 1.21 eV, respectively.[154] This difference in turn can explain the experimental finding that the etching of Al from Nb_2AlC requires longer times and higher HF concentrations than from Ti_2AlC (see Table 5). Similarly, Min *et al.*[155] predicted, using DFT calculation, that Ti-Al bond in case of Ti_2AlC is weaker than that for Ti_3AlC_2. Comparing the conditions needed to etch Al from Ti_3AlC_2 to those needed in case of Ti_2AlC, show more severe conditions for the former (50% HF for Ti_3AlC_2, and 10% HF for Ti_2AlC).

The etching time can be significantly reduced by attrition milling the MAX phase powder. For example, the required etching time for V_2CT_x decreased from 90 h to 8 h by milling V_2AlC at 700 rpm for 4 h. The time can also be decreased by increasing the temperature. For example increasing the temperature from RT to 55 °C reduced the etching time of Nb_2AlC from 90 h to 40 h to produce Nb_2CT_x.

4.7.2 Stability of MXenes

An important variable is the value of n for a given $M_{n+1}AlC_n$ phase. In general the higher the n, the more stable the MXene. For example, immersing Ti_2AlC in 50% HF - the same conditions that yielded MXene from Ti_3AlC_2 - resulted in its complete dissolution. It is only by reducing the HF concentration from 50% to 10%, that Ti_2CT_x was obtained from Ti_2AlC.[130] This experimental finding is in agreement with what Shein *et al.*[156] found using first principles calculations. They found that the stability of MXenes increase with increasing the n value from 1 to 3, *i.e.* M_4X_3 is more stable than M_3X_2 which is more stable than M_2X.

To date, all attempts to produce nitride-based MXenes, such as Ti_2N (Appendix B) have failed. In contradistinction, it is possible to selectively etch the Al from Ti_3AlCN to produce Ti_3CNT_x (see Table 5). Note that the calculated cohesive energies of $Ti_{n+1}N_n$ are lower than those of $Ti_{n+1}C_n$, whereas the formation energies of $Ti_{n+1}N_n$ from $Ti_{n+1}AlN_n$ are higher than those of $Ti_{n+1}C_n$ from $Ti_{n+1}AlC_n$.[156] The lower cohesion energy implies lower stability of the structure, whereas the higher formation energy of the MXenes from their corresponding Al containing MAX phases implies that the Al atoms are bonded more strongly in $Ti_{n+1}AlN_n$ compared to $Ti_{n+1}AlC_n$ and thus require more energy for their extraction. These two factors may explain the failures in producing nitride MXenes to date. Another distinct possibility is that the 2D nitride layers dissolve in the HF solution due to the lower stability of the $Ti_{n+1}N_n$ layers.

4.7.3 Variations in c-LP

As listed in Table 5 (column 9) the change in *c*-LP upon etching the A-group layers, Δ *c*-LP - as compared to the *c*-LP in the MAX parent phase - varies from 1.09 Å for $(Ti_{0.5},Nb_{0.5})_2CT_x$ to 10.83 Å for V_2CT_x. This Δ *c*-LP represents the change in the spacing between the $M_{n+1}X_n$ layers compared to their spacing in the MAX phases, so it is valid to compare their values for the different MXenes (211, 312, and 413). If the A-group layers were replaced by surface terminations only (OH, O, or/and F) in all the cases, then they should result in similar values of Δ *c*-LP. The exact reason for the large variation in Δ *c*-LP is not clear at the moment. However, many hypotheses can be considered. For example, the variation can be related to etching time, since most of the MXenes that have Δ *c*-LP > 6 Å were synthesized by HF treatments for long times, 33-90 h. Two exceptions for this finding are MXenes produced from attrition milled MAX

phases (V_2CT_x that was synthesized by an 8 h HF and $(Ti_{0.5},V_{0.5})_2CT_x$ was synthesized by 4 h HF treatment) and the second is Ti-V solid solution MXenes – *viz.* $(Ti_{0.5},V_{0.5})_3C_2T_x$ that was synthesized by HF treatment of $(Ti_{0.5},V_{0.5})_3AlC_2$ for 18 h and $(Ti_{0.5},V_{0.5})_2CT_x$ from $(Ti_{0.5},V_{0.5})_2AlC$ using HF for 19 h. Those two exceptions with the fact that the least Δ *c*-LP was noticed for $(Ti_{0.5},Nb_{0.5})_2CT_x$ that was synthesized by etching $(Ti_{0.5},Nb_{0.5})_2AlC$ using HF for 28 h which is not a short reaction time, suggest that the role of reaction time is not the key for understanding the variation in Δ *c*-LP.

The variations appear to be related more to the MXene composition. The large expansions suggest that significantly more water intercalates between the $M_{n+1}X_n$ layers when large Δ *c*-LP are observed. It is crucial to note here that without assuming that H_2O molecules are intercalated in between the MXene layers, it is difficult, if not impossible, to rationalize the large Δ *c*-LPs observed in some case. Spontaneous water intercalation has been reported for other layered materials.[157] Of course, co-intercalation of reaction products is also possible.

To test the idea of water intercalation, Nb_2CT_x powders were heated in vacuum at 400 °C for 40 h, which resulted in a shift of the (0002) peaks to higher angles in the XRD patterns (Figure 20a). These shifts correspond to a *c*-LP decrease from 22.34 Å to 15.85 Å. This large reduction in the *c*-LP for Nb_2CT_x, on the other hand, must thus be mainly due to de-intercalation of a compound - most probably water molecules - from between the layers. To confirm this conclusion, inelastic neutron scattering, INS, measurements for Nb_2CT_x were performed.[9] As shown in Figure 20b, the INS spectrum for Nb_2CT_x before annealing shows a strong broad peak between 65 and 110 meV that can be

[9] INS measurements were carried out by Dr. Alexander I Kolesnikov at Oak Ridge National Laboratory (ORNL). Reprinted with permission from *J. Am. Chem. Soc.*. DOI: 10.1021/ja501520b. Copyright 2014 American Chemical Society.

assigned to intermolecular librational band of bound water, $\nu_L(H_2O)$, two narrow peaks at 130 and 144 meV that can be related to O-H hydroxyl bending modes, a peak around 205 meV that can be assigned to ν_2 (H-O-H) scissor intramolecular vibration and another broad peak between 390 and 440 meV that can be explained by a combination of ν_1 & ν_3 s-OH & a-OH water intramolecular stretching modes and stretching modes of O-H hydroxyls. All these peaks indicate the presence of water and hydroxyl groups in Nb_2CT_x before annealing. Their disappearance after vacuum annealing (bottom spectra in Figure 20b) confirms their assignment and the concomitant loss of water and OH groups. The strongest band in the spectrum of the vacuum annealed sample, at energies below 30 meV, is probably due to lattice modes involving the heavy Nb atoms; contributions from C atoms are expected to be around 60-80 meV.

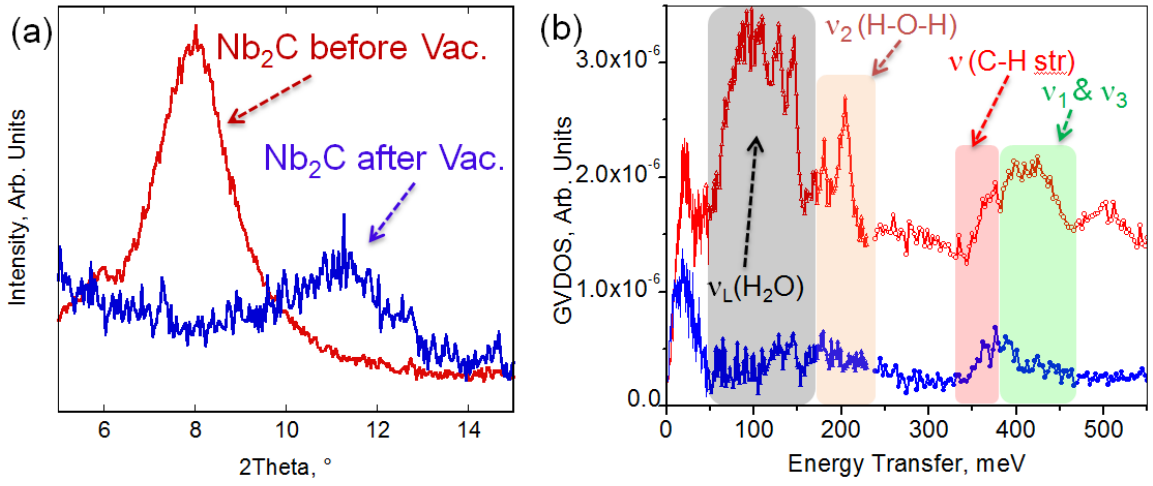

Figure 20: (a) XRD patterns for Nb_2CT_x sample before and after vacuum annealing at 673 K for 40 h, (b) The generalized vibrational density of states obtained from inelastic neutron scattering spectra for Nb_2CT_x sample before (red curve) and after (blue curve) annealing. Reproduced with permission [158] Copyright 2014, American Chemical Society.

In the energy range of intermolecular translational vibrations of bulk water/ice (below 40 meV) in the present data there is only one broad peak at around 20 meV, which is a characteristic feature of strongly *confined* water (for bulk water/ice the INS spectra should exhibit a peak around 6 meV due to transverse acoustic modes of a hydrogen-bonded water network).

There are two more peaks – at 175 meV and 370 meV - observed in the spectra before and after vacuum annealing. These can be assigned, respectively, to C-H bending and stretching modes of the ethanol that was used during MXene synthesis and is probably still present in the sample in trace amounts. Enyashin *et al.*[159] have computationally predicted that alkoxy functionalized MXene can form in contact with ethanol, thus the C-H modes could be from a small number of ethoxy functional groups that survived annealing. The origin of these bands is unclear at the moment, inviting further studies.

Table 6 lists the Nb:C:O:F:Al atomic ratios determined from EDX before and after vacuum annealing. The ratios are normalized to 2 Nb. Since no Nb_2AlC peaks were observed in the XRD patterns, it is reasonable to assume that all remaining Al in the etched powders is in the form of aluminum fluoride salts. In general estimating the C content from EDX spectra is problematic since C is readily found as a contaminant. The problem is exacerbated in Nb-containing materials because the K_α energy of C and the M_{IV} energy of Nb are close to each other in energy. Given that there is no external source for C in the etching process that could increase the C content, it is reasonable to assume that the Nb:C ratio is 2:1 instead of the 2:1.6 measured in EDX.

Table 6: Atomic ratio of Nb : C : O : F : Al normalized to 2 Nb, calculated from EDX analysis for Nb_2CT_x powders before and after vacuum annealing at 400 °C for 40 h.

	Nb	C	O	F	Al
Nb_2CT_x Before annealing	2.0	1.6	2.5	0.65	0.12
Nb_2CT_x after vacuum annealing (400 °C, 40 h)	2.0	1.8	2.0	0.35	0.11

The O:Nb atomic ratio is reduced from 2.5:2.0 before annealing to 2.0:2.0 after annealing, which is in agreement with INS results that shows significant reduction of water and hydroxyl groups due to annealing. Also, the atomic ratio of F dropped from 0.65 before annealing to 0.35, for every 2Nb, after annealing. Note that the F/Al ratio is ~ 3.1, which is quite close to the composition of aluminum fluoride, AlF_3. This means that not only water and hydroxyls are eliminated by annealing, but also about half the F content.

4.7.4 The role of MAX phase synthesis conditions

Two different Ti_3AlC_2 samples were synthesized starting with the same precursors (Ti_2AlC + TiC) but under different conditions. The first one (sample 1) was synthesized by hot pressing the mixture at 1400 °C for 4 h using a load that corresponded to stress of 30 MPa and a vacuum of 1.3 Pa. The resulting material was a fully dense Ti_3AlC_2 phase, with residual TiC (Figure 21a). Powders were obtained from the fully dense brick by milling using a TiN coated bit. The second sample (sample 2) was synthesized under Ar flow by heating to 1350 °C for 30 minutes with no pressure. This process resulted in powder compact of pure Ti_3AlC_2 (Figure 21b) that was easily ground into a powder by lightly crushing it in a mortar and pestle. In both cases powders were sieved, and only - 400 mesh (< 38 μm) powders were used. Although both samples were

treated with the same conditions - 50% HF at RT for a week - completely different products were obtained. In case of sample 1, the weight loss due to the HF treatment was ~ 10%, while for sample 2 it was ~ 70%.

As shown in Figure 21a, XRD pattern after HF treatment of sample 1 shows peaks for TiC that was present initially in the as-synthesized Ti_3AlC_2 sample, in addition to the {000*l*} peaks for MXene correspond to *c*-LP of ~ 19.67 Å. XRD pattern for sample 2 after HF treatment (top pattern in Figure 21b) shows a mixture of hydrated aluminum fluoride and oxide, and aluminum hydroxide. Also, the (0002) peak of MXene shifted to a much lower angle (2θ of ~ 6.78°), which translates to *c*-LP of 26.05Å. This large increase in the *c*-LP of sample 2 can be explained by intercalation of water or etching products between the layers similar to what was observed for Nb_2CT_x.

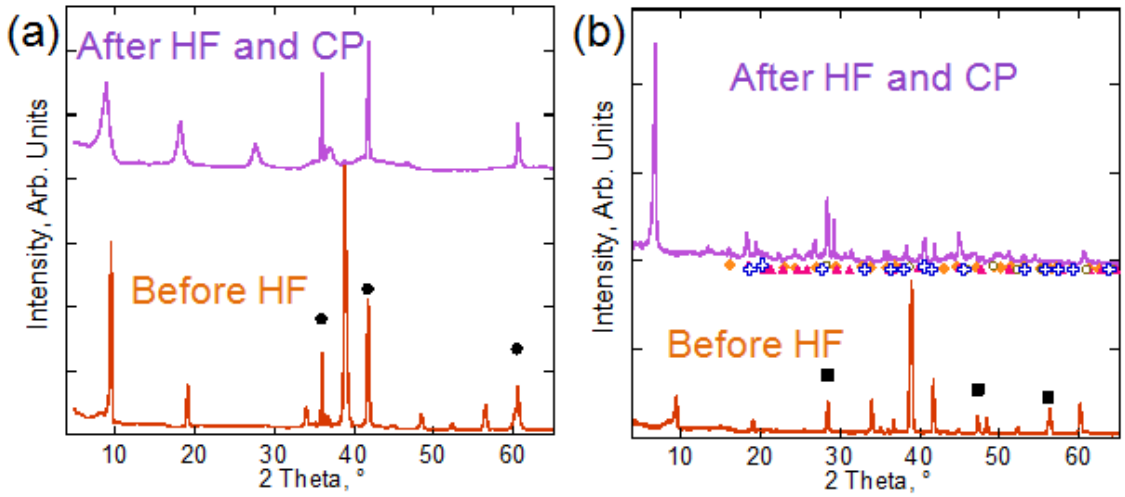

Figure 21 XRD before and after HF treatment using 50% HF for 1 week at RT for Ti_3AlC_2 synthesized by heating to, (a) 1400 °C for 4 h under 30 MPa in vacuum, (b) 1350 °C for 0.5 h under Ar flow and no pressure. The black circles in (a) represent the peaks position of TiC [PDF#32-1383], the black squares in (b) represent the peaks position of Si that was used as an internal reference, while the diamond, crosses, triangles, and circles represent peaks position for $AlF_3.3H_2O$ [PDF#46-1459], $Al(OH)_3$ [PDF#15-0136], $Al(OH)_3$ [PDF#18-0031], and $Al_2O_3.3H_2O$ [PDF#01-0774], respectively.

The exact reasons for the different behavior of the same MAX phase, synthesized differently, is not clear at the moment. One possible explanation could relate to the MAX phases' grain size of the. Grain growth in ceramics is known to be hindered by the presence of pores.[160] Thus, it is reasonable to assume that the fully dense sample had the larger grains. Also, the fact that TiC coexisted with Ti_3AlC_2 in the fully dense sample with no Al or Ti_2AlC means that all the starting materials (Ti_2AlC and TiC) were used to form Ti_3AlC_2. Then, the latter was partially dissociated into TiC, and Al that sublimated under high vacuum with the following reaction path: $Ti_2AlC + TiC \rightarrow Ti_3AlC_2 \rightarrow 3TiC_{0.66} + Al_{(g)}$.[161, 162]

Other possible reasons could relate to the presence of atomic defects (*e.g.* vacancies) or/and nonstoichiometric compositions of the MAX phases.

4.7.5 $Ti_3C_2T_x$ Shelf Life:

To shed light on the shelf life of $Ti_3C_2T_x$, powdered sample was placed in a glass vial that, in turn, was stored in a chamber that was kept at a pressure < 4 kPa at RT for 28 months. Comparing the XRD patterns for the freshly synthesized $Ti_3C_2T_x$ (orange solid line in Figure 22a) to the same sample after storing for 28 months (black dotted line in Figure 22a) showed them to be almost identical. This means that $Ti_3C_2T_x$ can be stored dry for a relatively long time. Note that a small amount of $TiOF_2$ (represented by blue diamond in Figure 22a) can be observed after storing for 28 months. The $TiOF_2$ crystals grew on $Ti_3C_2T_x$ as can be seen in an SEM image (see inset in Figure 22a).

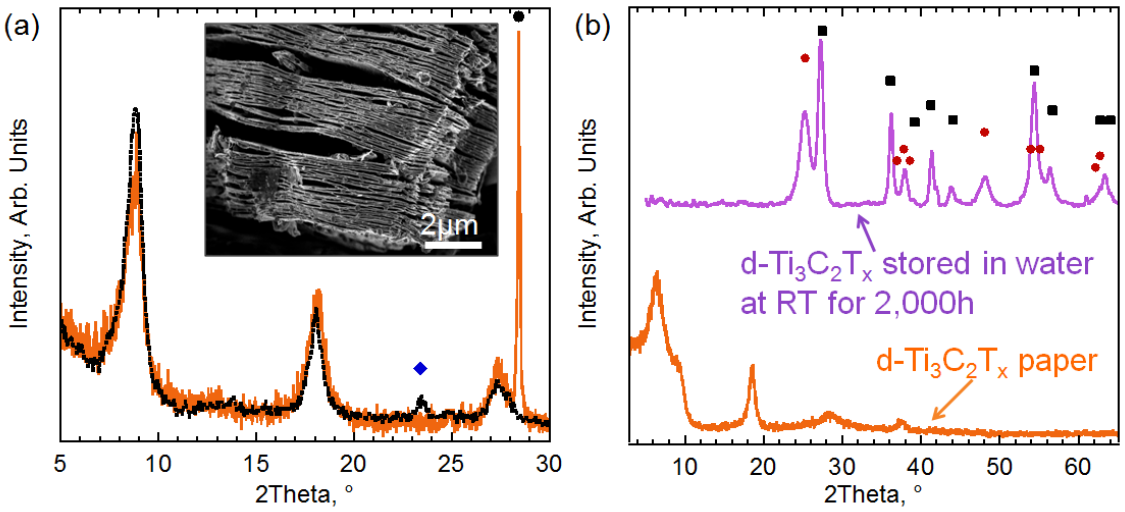

Figure 22: (a) XRD patterns for $Ti_3C_2T_x$ before (orange solid line) and after storing in a glass vial for 28 months (black dotted line). The black circle represents the peak position of Si that was used as an internal reference. The blue diamond represents peak position of $TiOF_2$ [PDF#01-0490] The inset is a typical SEM image of $Ti_3C_2T_x$ after storing in water for 28 months. (b) XRD patterns of d-$Ti_3C_2T_x$ "paper" and white sediment of d-$Ti_3C_2T_x$ after storing in water for 2,000 h at RT. Red circles represent anatase [PDF#21-1272]; black squares represent rutile [PDF#21-1276].

Storing d-$Ti_3C_2T_x$ flakes in water in a closed glass jar, however, for 2,000 h at RT resulted in the formation of both anatase and rutile (Figure 22b). Over that time, the colloidal suspension's color turned from black to white, before the white particles de-flocculated and the solution became clear. Typical SEM images (Figure 23a and b) of the material stored in water showed two main morphologies: i) agglomerates of small fragments of sheets (Figure 23a) and, ii) sheets of nano particles (Figure 23b).

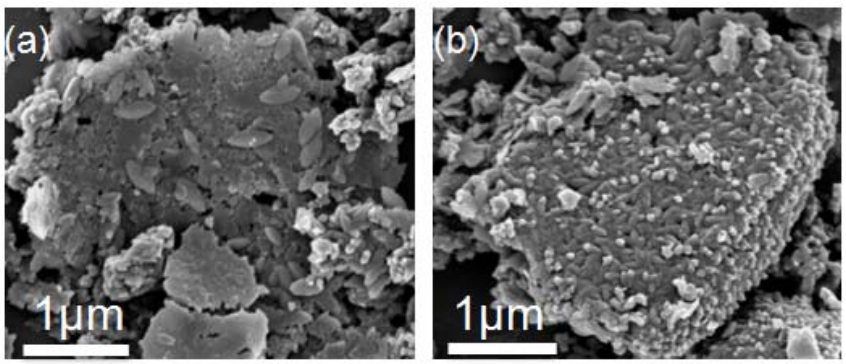

Figure 23: (a) and (b) SEM images for d-$Ti_3C_2T_x$ after storing in water for 2,000 h at RT

The two different morphologies can be assigned to the two different phases identified in the XRD patterns. To identify which morphology is anatase and which is rutile will require more work. What happens to the C is also unclear at this time, but it is most probably oxidized to CO_2. Rutile formation at RT was reported before by electrochemical anodiziation of Ti in fluoride contained electrolytes.[163] The oxidation of d-$Ti_3C_2T_x$ in water is an important result since it shows that water may not be the best storing medium for delaminated MXene, if oxidation is to be prevented. It also demonstrates the propensity of the delaminated flakes to oxidize. We note in passing that when the flakes are stacked they are much less prone to oxidation.

It is worth noting here that if the sample was not well washed and dried after HF etching (*i.e.* washed to pH < 4), the etching products, *viz.* hydrated aluminum fluoride ($AlF_3 \cdot 3H_2O$), crystallize in few days. As shown in Figure 24, annealing this sample at 200 °C under a mechanical vacuum of 1 kPa for 20 h results in the loss of peaks associated with $AlF_3 \cdot 3H_2O$; small peaks belonging to $TiOF_2$ are formed instead. The annealing resulted also in narrowing the 0002 peak of $Ti_3C_2T_x$ and shifting it from a 2θ of 8.6° to 9.0°. That shift corresponds to change of *c*-LP from 20.55 Å to 19.64 Å, which could be explained by removing water or etching products from the $Ti_3C_2T_x$ interlayer spaces.

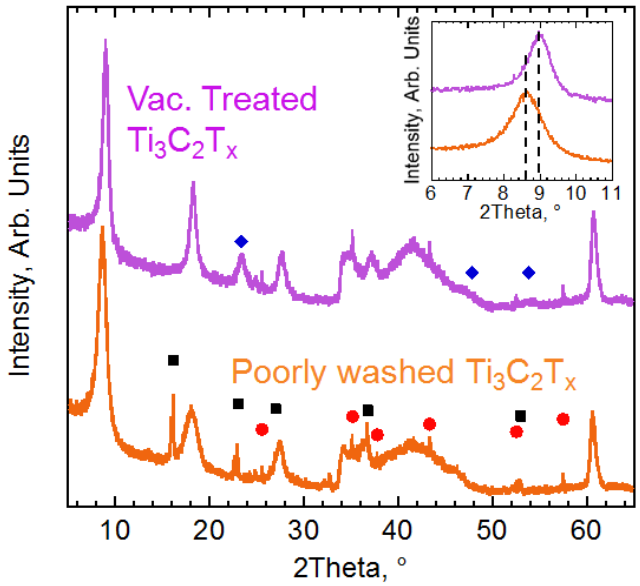

Figure 24: XRD patterns of, (a) poorly washed and dried $Ti_3C_2T_x$ after the HF treatment of Ti_3AlC_2 and, (b) the same sample after vacuum annealing at 200 °C for 20 h under vacuum pressure of 1 kPa. The black squares represent the peaks position of $AlF_3 \cdot 3H_2O$ [PDF#35-0827], the red circles those of Al_2O_3 [PDF#46-1212], and the blue diamonds those of $TiOF_2$ [PDF#01-0490].

4.8 Properties of MXenes

Since our first report on the synthesis of MXenes, many theoretical papers have been published on their electronic structure and properties. Here in this section a brief summary for the theoretically predicted properties is given, in addition to the experimentally measured properties in this work.

4.8.1 Theoretically Predicted Properties

The electronic properties of MXenes are of special interest as they, in principle, can be tuned by changing the MXene elemental composition and/or their surface terminations. The later can influence MXenes' electronic properties such as their band gaps. In our first report on the synthesis of $Ti_3C_2T_x$ [129] it was theoretically precited that while bare Ti_3C_2 surfaces would be metallically conducting, small band gaps of 0.05 eV

and 0.1 eV open up for $Ti_3C_2(OH)_2$ and $Ti_3C_2F_2$, respectively. At the time, we suggested that it would be possible to tune the electronic structure of MXenes by varying the surface terminations, T. It was further confirmed that the electronic structure of MXenes is sensitive not only to the type of surface terminations, but also to their orientation relative to the MXene sheets. The MXenes' band structure and electronic density of states (DOS) have been extensively studied by DFT. Bare MXene monolayers are metallic, with a high electron density near the Fermi level.[129, 156, 164-166] While terminated MXenes, especially O-terminated ones, have been predicted to be semiconducting.[164]

Some MXenes are predicted to be either ferromagnetic, such as Cr_2C, Cr_2N,[164] and Ta_3C_2,[167] or antiferromagnetic, such as Ti_3C_2, Ti_3N_2.[156] Although magnetism is an important property, for the most part it is only predicted for MXenes with bare surfaces. When surface terminations, T, (even when T = H) are present, the magnetism disappears. Prominent exceptions are Cr_2C and Cr_2N, which are predicted to retain significant magnetic moments in their terminated state (T = O, OH, F) up to nearly room temperature.[164] Unfortunately, Cr_2XT_x has not been experimentally produced yet to test this important prediction.

High thermoelectric Seebeck coefficients were predicted for MXenes using DFT calculations by Khazaei *et al.*.[164] The Seebeck coefficients values (~1000 μV/K) predicted for semiconducting Ti_2CO_2 and $Sc_2C(OH)_2$ at ~ 100 K are comparable to the reported giant Seebeck coefficients of $SrTiO_3$ (850 μV/K at ~ 90 K). This prediction opens a totally new area of potential applications for these surface terminated MXenes.

The mechanical properties of MXenes are of great interest since the M-C and/or M-N bonds are some of the strongest known. At this juncture the only information

available on how MXenes would respond to stress, are the elastic constants when they are stretched along the basal planes, *i.e.* c_{11}. An early DFT study of $Ti_3C_2(OH)_2$ predicted a c_{11} ~ 300 GPa.[129] A follow up study [168] predicted that the c_{11} values of different, bare or un-functionalized $M_{n+1}C_n$ layers, would be higher than in their parent MAX phases. This could be due to the strengthening of M-X bonds in the MXenes layers when the A atoms are removed and the electron density is more concentrated within the $M_{n+1}C_n$ layers. However, the enhanced mechanical properties could also be due to the difficulty in accurately estimating or defining the exact thickness of a single MXene layer.

4.8.2 Experimentally Measured Properties:

MXene powders are ductile enough to be cold pressed into free-standing thin discs. A picture of cold-pressed discs of different MXene compositions is shown in Figure 25. Their densities (Table 7) varied between 2.91 $g \cdot cm^{-3}$ for Ti_2CT_x to 6.82 $g \cdot cm^{-3}$ for $Ta_4C_3T_x$.. If one assumes the *c*-LP listed in Table 5, and T_x to be $(OH)_2$, then it is possible to calculate their theoretical densities. The last row in Table 7 lists the measured densities of the pressed discs. The numbers in parenthesis list the % of theoretical densities that range from 50 to ≈ 65%.

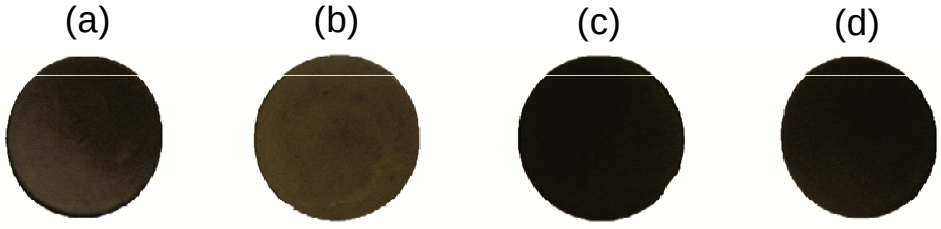

Figure 25: Photograph of cold pressed freestanding ~300 µm discs with a diameter of 25 mm of (a) Ti_2C, (b) Ta_4C_3, (c) TiNbC and, (d) Ti_3CN_x. Reproduced with permission.[130] Copyright 2014, American Chemical Society.

The sheet resistivity and resistivities of the various MXene discs are also shown in Table 7. Generally these values are comparable to multilayer graphene reported by Li *et al.*[169] and Blake *et al.*[170] The resistivity values are higher than the MAX phases before treatment (< 10 Ω/□) presumably because of the replacement of the A-layers with OH and/or F. Assuming that the surface groups are similar in all the exfoliated MAX phases, the difference in the resistivity between the different phases can be partially explained by the different number of atomic layers (3, 5, and 7 for M_2X, M_3X_2, and M_4X_3 phases, respectively). It is important to note here that the resistivity values reported in Table 7, are significantly higher than single MXene sheets because of the method by which the resistivity was measured. For example, the resistivity of bulk sintered Ti_3AlC_2 is 0.39 μΩ m.[171] When Ti_3AlC_2 powders were cold pressed at 1 GP, their resistivity increased to 1200 μΩ m; a roughly 3000 time increase.

Table 7: Resistivity and water contact angle on cold-pressed free standing discs for different exfoliated phases, and their densities.

Property of MXene	Ti_2CT_x	$TiNbCT_x$	Ti_3CNT_x	$Ta_4C_3T_x$	$Ti_3C_2T_x$
Resistivity, Ω/□	339	171	125	104	22
Resistivity, Ω m	0.068	0.052	0.037	0.021	0.005
Contact angle, (deg)	32	31	27	41	34
Density of the cold pressed discs, $g \cdot cm^{-3}$ (% of theoretical)*	2.91 (62%)	3.23 (52%)	2.95 (64%)	6.82 (53%)	3.12 (60%)

* The densities were estimated from the dimensions and weights of the cold pressed discs. Number in parenthesis is relative theoretical density assuming T_x to be $(OH)_2$ and the *c*-LP listed in Table 5.

Contact angle measurement results for the water droplets on the cold pressed discs are also listed in Table 7. These values are lower than those of the corresponding MAX

phases - also measured in this work on cold pressed samples, which were around 60º. The reduction in contact angle can be explained by the presence of OH surface groups after HF treatment. It is worth noting that graphene can be transformed from superhydrophopic to superhydrophilic by altering the surface groups.[172] The hydrophilicity of the MXenes is an advantage when using aqueous electrolytes in energy storage devices or dispersing them in water and alcohols for further processing.

CHAPTER 5: *MXenes* PERFORMANCE AS ELECTRODE MATERIALS FOR LITHIUM-ION BATTEREIS

The rich chemistries and unique morphologies of MXenes, in addition to their good electronic conductivity, render them strong candidates for many applications that range from sensors and electronic device materials, to catalysts in the chemical industry, conductive reinforcement additives to polymers, electrochemical energy storage materials, and many others. Here, I focus on the performance of MXenes as electrode materials for LIBs. The mechanisms of lithiation and delithiation are also discussed in this chapter.

5.1 Performance of MXenes Electrodes in LIBs

5.1.1 Effect of Carbon Additive:

To find out whether MXenes need conductive additives when used as electrodes, three electrodes were prepared and tested with the following compositions: (i) 90 *wt.*% $Ti_3C_2T_x$ with 10 *wt.*% PVDF, (ii) 80 *wt.*%$Ti_3C_2T_x$ with 10 *wt.*% PVDF and 10 *wt.*% CB, and, (iii) 90 *wt.*% CB and 10 *wt.*% PVDF. As shown in Figure 26, comparing the CVs of electrodes (i) and (ii) shows that adding 10 *wt.*% of CB to the $Ti_3C_2T_x$ electrode resulted in an increase in the CV area which is evidence for higher stored capacity. Also, new lithiation peak appeared at a voltage of ~ 1.35 V *vs.* Li/Li^+, and the lithiation peak at 0.68 V shifted to 0.83 V and became more intense. Similarly, during delithiation the intensity of the peak at 1 V became much higher and shifted to 1.07 V after adding 10% CB.

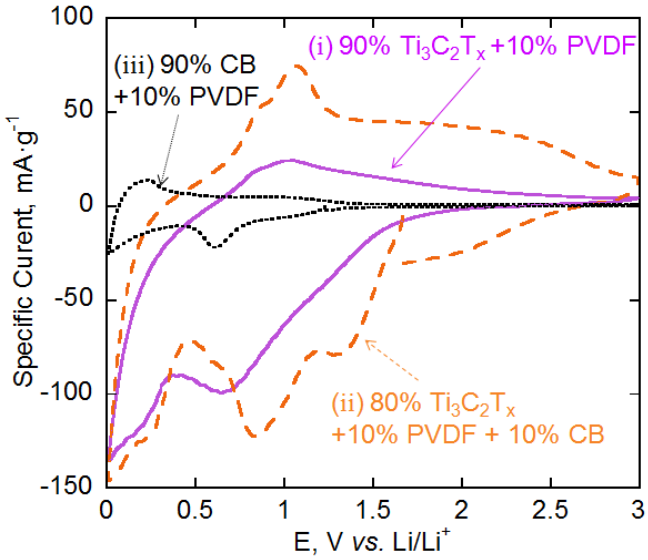

Figure 26: Cyclic voltammograms at 0.2 $mV \cdot s^{-1}$ for electrodes of (i) 90 *wt.*% $Ti_3C_2T_x$ with 10 *wt.*% PVDF (solid purple curve), (ii) 80 *wt.*%$Ti_3C_2T_x$ with 10 *wt.*% PVDF and 10 *wt.*% CB (dashed orange curve), and (iii) 90 *wt.*% CB and 10 *wt.*% PVDF (dotted black curve). The specific current of the carbon black electrode plotted here was 10% of the value measured for this electrode, which is the ratio of CB used in MXene electrode.

To find if the changes observed upon addition of CB are due to the contribution of the latter only, electrode (iii) was cycled using the same rate as (i) and (ii). The specific current of the CB electrode was normalized to match the 10 *wt.*% that was used in electrode (ii). The area of the CV for CB (black dotted curve in Figure 26) is almost negligible, specially at voltages higher than 1.5 V. Furthermore, the CV for electrode (iii) showed no peaks where the peaks for electrode (ii) were observed. Thus, it can be concluded with no doubt that increasing the area of the CV and the changes in the lithiation and delithiation peaks after adding CB are not due to the latter, but originated from the $Ti_3C_2T_x$ itself.

The enhancement in the performance of the $Ti_3C_2T_x$ electrodes after addition of CB can be explained by an increase in the conductivity. Unless otherwise stated, composite electrodes of 80 *wt.*% MXene + 10 *wt.*% CB + 10 *wt.*% PVDF were used in

this work. More work on the effect of different carbon additives and binders can be found in standalone master thesis by Mr. Dall'agnese.[173]

5.1.2 M_2C: Ti_2CT_x, V_2CT_x, and Nb_2CT_x:

Testing Ti_2CT_x, Nb_2CT_x and V_2CT_x (produced by HF treatment of attrition milled V_2AlC powders at RT for 8 h) as electrode materials (Figure 27a) showed that they are capable of handling high cycling rates. At 10*C*, capacities of 110 $mAh \cdot g^{-1}$ for Nb_2CT_x and 125 $mAh \cdot g^{-1}$ for V_2CT_x were obtained after 150 cycles. These values are much higher than what was reported for commercial graphite when charged and discharged at 10*C* (graphite loses more than 80 % of its theoretical capacity at 10*C*).[174] These values are ≈ 50 % higher than those for Ti_2CT_x at the same rate and are closer to capacities obtained at 1*C*. The higher capacity of V_2CT_x compared to Nb_2CT_x and Ti_2CT_x was explained by Xie *et al.*[158] as a result of lower Li diffusion barrier (calculated using theoretical calculations) for the former compared to the others. The coulombic efficiency at the reversible capacity was about 99.6% for Nb_2CT_x at 10*C*. For V_2CT_x it varied between 98% and 100%.

Although the reversible capacity of MXenes at high cycling rates (*i.e.*, 10*C*) is comparable to titania based anodes,[175] the latter have a maximum theoretical capacity of 170 $mAh \cdot g^{-1}$, even at slow scan rates, while V_2CT_x (produced from milled V_2AlC) has a reversible capacity of 280 $mAh \cdot g^{-1}$ at 1*C*.

Figure 27b-d show the voltage profiles for the Nb_2CT_x, Ti_2CT_x, and V_2CT_x electrodes. A common feature in the profiles of all the MXenes is the sloping nature of the curves, *i.e.* the absence of any plateaus especially after the first lithiation cycle. This

is an indication for presence of a single phase during Li addition/extraction.[176] In other words, it can be considered as a solid solution reaction of Li with MXene that involves no phase or structural transformation upon lithiation and delithiation. Similar sloping profiles were reported for many electrode materials such as amorphous silicon,[177] amorphous oxides [178] and some nano crystalline materials, *e.g.* titanate nanotubes.[179]

The voltage profile for Nb_2CT_x at a 1*C* cycling rate (Figure 27b) yields a first cycle capacity of ~ 422 $mAh \cdot g^{-1}$. The second cycle capacity was about 250 $mAh \cdot g^{-1}$. The reason for the first cycle irreversibility is not totally understood at this time. It could be due to solid electrolyte interphase (SEI) formation or due to irreversible reactions of Li with the surface groups and/or water molecules in the as-synthesized MXenes. In principle this irreversibility could be minimized by controlling the MXene's surface chemistry and/or by pre-lithiating the electrode material as reported for other systems.[180] After 100 cycles, a reversible capacity of 170 $mAh \cdot g^{-1}$ was obtained. And while 170 $mAh \cdot g^{-1}$ is comparable to what was reported for hollow niobium oxide nanospheres,[181] the average lithiation voltage is lower in our material.

Figure 27d shows the voltage profile, at 1*C*, for V_2CT_x that was produced from non-milled V_2AlC. The first cycle capacity was found to be ~ 380 $mAh \cdot g^{-1}$ and a reversible capacity ~ 210 $mAh \cdot g^{-1}$. Intriguingly, the V_2CT_x, produced by etching attrition milled V_2AlC, showed > 30 % enhancement in Li uptake (Figure 27a) compared to V_2CT_x produced from un-milled V_2AlC. This can be explained by the decreased particle size that enhances Li diffusion between the layers. At the same cycling rate of 1*C* and after 50 cycles, a reversible capacity of 288 $mAh \cdot g^{-1}$ was obtained for V_2CT_x produced

from milled V_2AlC instead of 210 mAh.g^{-1}. A reversible capacity of 260 mAh·g^{-1} was obtained for the V_2CT_x, produced by etching attrition milled V_2AlC, after 150 cycles.

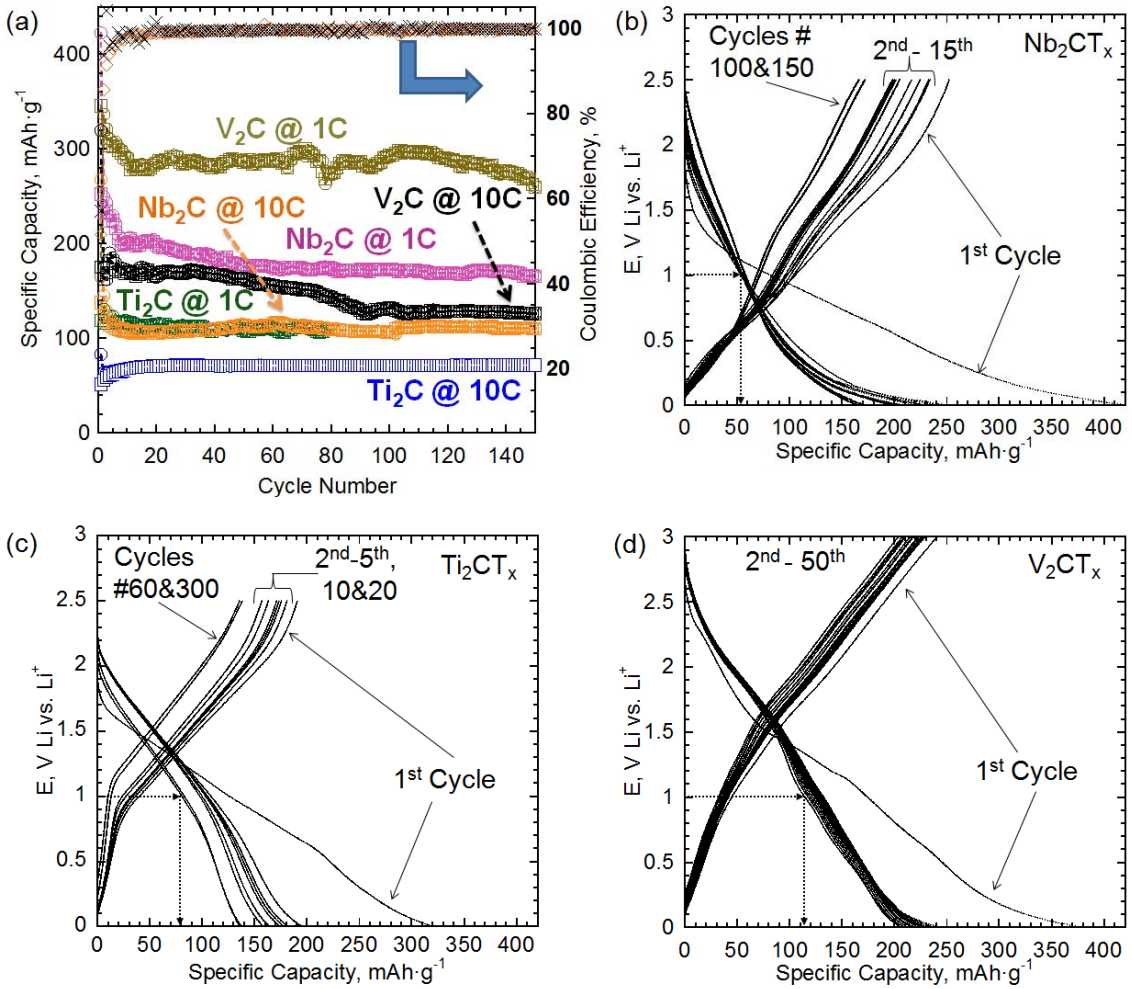

Figure 27: Electrochemical performance of Nb_2CT_x, Ti_2CT_x and V_2CT_x as electrodes in LIB. (a) Specific lithiation (circles.) and delithiation (squares) capacities (per mass of active material) *vs.* cycle number at different rates for Nb_2CT_x and V_2CT_x-based electrodes (produced by HF treatment of attrition milled V_2AlC at RT for 8 h) compared to Ti_2CT_x (produced from commercial Ti_2AlC powder). Voltage profiles *vs.* Li/Li$^+$ at 1 C cycling rate for, (b) Nb_2CT_x, (c) Ti_2CT_x (from Ti_2AlC synthesized from its elements), and, (d) V_2CT_x (from non milled V_2AlC), respectively. The horizontal and vertical arrows in b-d indicate the voltage at 1 V *vs.* Li/Li$^+$ and its corresponding capacity. Reproduced with permission. [132, 139]

More than 2/3 of the reversible lithiation capacity for Nb_2CT_x is below 1 V (Figure 27b), while for both Ti_2CT_x (Figure 27c) the capacities below 1V were about 1/2

of the reversible capacity. Conversely, in the case of V_2CT_x, less than 1/2 of the reversible lithiation capacity is below 1 V and more than 2/3 of the delithiation capacity is at voltages higher than 1.5 V (Figure 27d). The electrode's potential for transition metal based electrodes is known to depend on the energy of a redox couple for the transition metal.[182] Similar trend that V has higher lithiation voltage than Ti which is higher than Nb for the redox couple of M^{4+}/M^{3+} was reported for $M_2(PO_4)_3$ system, respectively, their potentials relative to Li were found to be 3.8 V, 2.5 V, 1.8 V. [183]

This is an important finding since it demonstrates that each MXene has its own active voltage window. With the variety of possible MXenes chemistries and surface terminations, selection of an optimum MXene for a required voltage window can in principle be achieved. Said otherwise, some MXenes could function better as anodes, while others could, in principle, be used as cathode materials for LIBs.

5.1.3 $Ta_4C_3T_x$:

CVs of $Ta_4C_3T_x$ between 0 and 3 V (Figure 28a) showed an irreversible sharp peak during lithiation around 1.1 V *vs.* Li/Li^+ during the first cycle. In subsequent cycles, three reversible lithiation peaks were observed: (I) around 1.5 V, (II) around 0.7 V, and (III) closer to 0 V. During lithiation three other peaks were observed (III') around 0.1 V, (II') around 1.4 V and (I') around 2.45 V. The peaks intensities increased with cycling.

The irreversible peak observed in the CV in the first cycle (Figure 28a), translated into a plateau in the voltage profile (Figure 28b), between 1.4 and 1.1 V during the first lithiation cycle in the GC (Figure 28b). In the first cycle, obtained at a *C*/12 cycling rate, 240 $mAh \cdot g^{-1}$ (inset in Figure 28b) was stored during lithiation, but only 150 $mAh \cdot g^{-1}$ was

recovered. The reversible capacity was ~ 140 $mAh \cdot g^{-1}$. It is worth noting that during delithiation, a significant decrease in the slope of the voltage profile can be seen in the 2.3 V to 2.6 V voltage range, *i.e.* a relatively high capacity can be extracted from the electrode in this range. Extending the voltage window in the CV (Figure 28c and d) after 25 cycles to 3.5 V instead of 3 V revealed two new lithiation peaks (IV) at ~ 2.8 V and (V) at ~3.25 V with corresponding delithiation peaks (IV') at ~ 3.1 V and (V') at ~ 3.4 V. This suggests $Ta_4C_3T_x$ could be a promising cathode material.

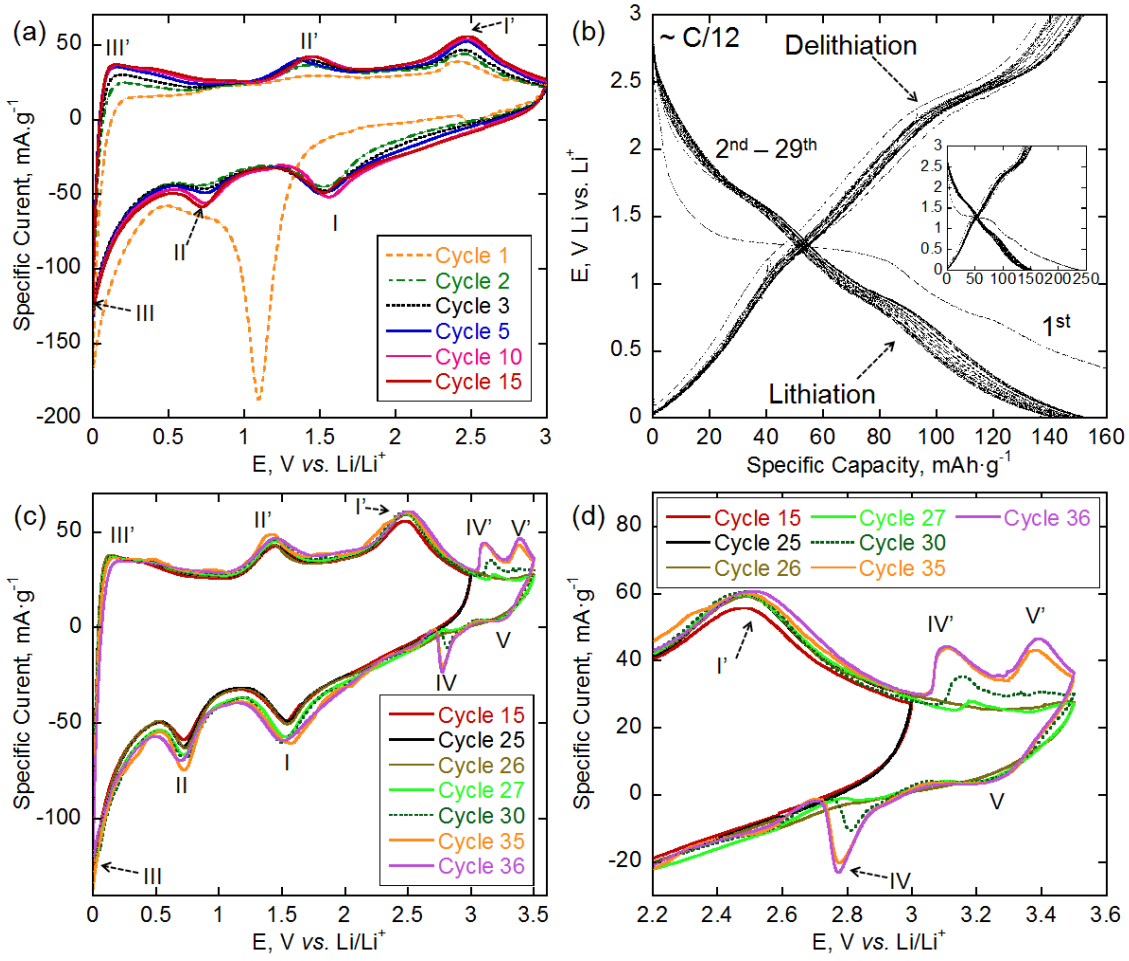

Figure 28: Electrochemical performance of $Ta_4C_3T_x$ as an electrode material for LIBs, (a) Cyclic voltammograms from 0 to 3 V *vs.* Li/Li^+ at a rate of 0.2 $mV \cdot s^{-1}$; (b) Voltage profile at C/12 cycling rate; inset shows the 1st lithiation cycle. (c) The same as (a) but extended to a voltage to 3.5 V instead of 3V after 25 cycles. (d) Same as (c) but with smaller X- and Y-axes ranges.

5.1.4 Effect of n: Nb_2C vs. Nb_4C_3

As will be discussed in detail in the *in situ* XRD section (5.2.1), we found that Li intercalates between the $M_{n+1}X_n$ layers. Thus, for a given chemistry, M_2X electrodes will have higher gravimetric capacities than their M_3X_2 or M_4X_3 counterparts, for the simple reason that the former have the least number of atomic layers per MXene sheet. However, it was interesting to investigate the gravimetric capacity and other lithiation and delithiation characteristics of $Nb_4C_3T_x$ and compare them to those of Nb_2CT_x.

The CVs of Nb_2CT_x (Figure 29a and b) show two reversible lithiation peaks (I) and (II) at voltages around 1.45 V and close to zero V, respectively. The corresponding delithiation peaks (I'), and (II') were found around 1.56 V and 0.65 V, respectively. The intensity of peak (II') decreased significantly after 20 cycles (dashed grey curve in Figure 29a and b).

For $Nb_4C_3T_x$, (Figure 29c and d) an extra lithiation peak around 2.26 V with a corresponding delithiation peak around 2.35 V was observed. The delithiation peak around 0.6 V vanished and a new peak (III') around 0.3 V appeared after 3 cycles.

The areas of the CVs corresponding to Nb_2CT_x are larger than those for $Nb_4C_3T_x$ (Figure 29 a and c). The estimated capacities from the CVs for both Nb_2CT_x and $Nb_4C_3T_x$ are shown in the inset of Figure 29c. If both electrodes store the same number of Li atoms, $Nb_4C_3T_x$ should have a capacity close to 50% of that for Nb_2CT_x. However, surprisingly, after 25 cycles $Nb_4C_3T_x$ showed a capacity as high as ~ 85 % of that for Nb_2CT_x (the capacities were 222 and 189 $mAh \cdot g^{-1}$ for Nb_2CT_x and $Nb_4C_3T_x$, respectively). Based on those capacities, and assuming that T_x in both Nb_2CT_x and $Nb_4C_3T_x$ stands for O_2 (this assumption is close to EDX results), the number of Li atoms

stored in those two phases are 1.9 and 3.1 for Nb_2CO_2 and $Nb_4C_3O_2$, respectively. The more Li atoms stored in case of $Nb_4C_3T_x$ can be correlated to the new peaks appeared in the CVs.

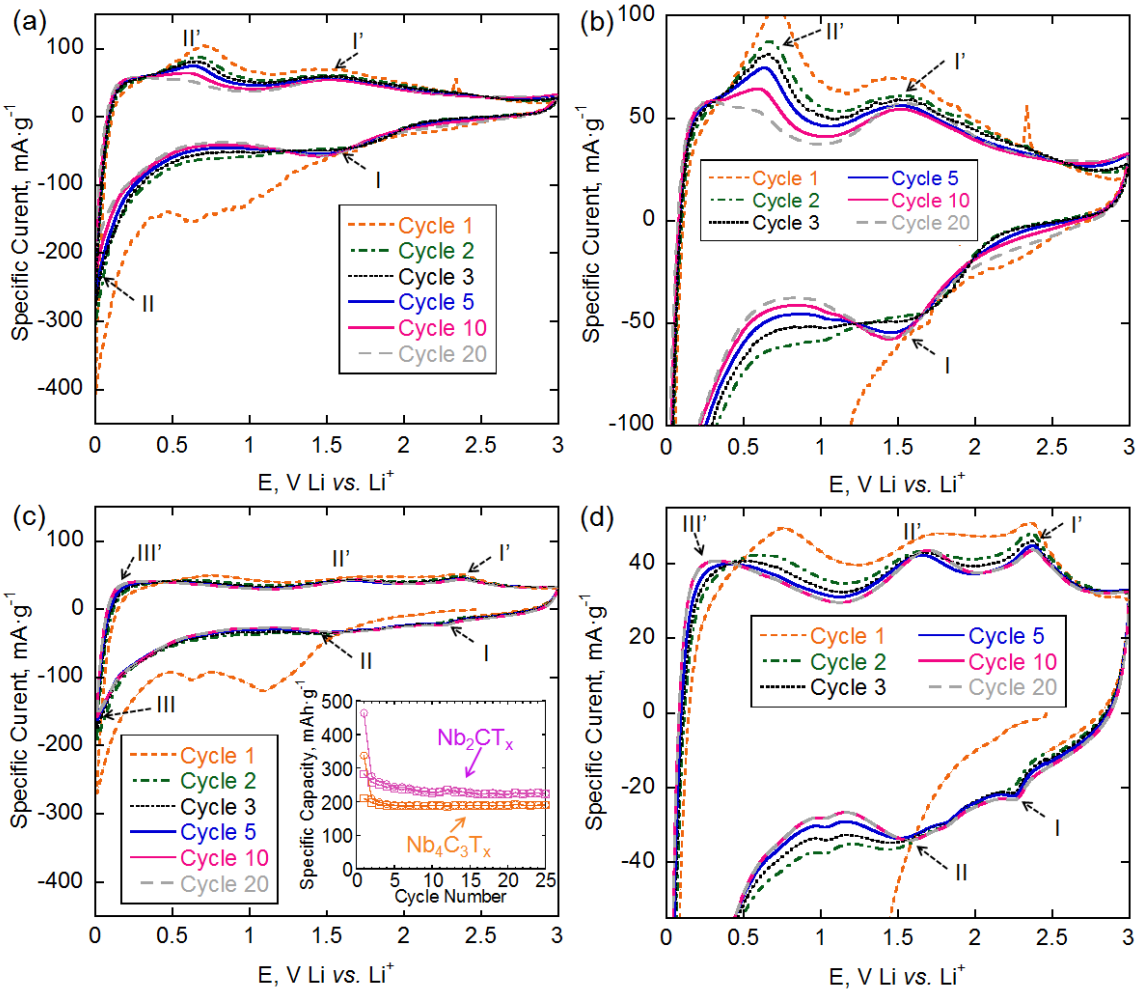

Figure 29: Cyclic voltammograms obtained at a rate 0.2 $mV \cdot s^{-1}$ for, (a) Nb_2CT_x and, (c) $Nb_4C_3T_x$. (b) and (d) are the same as (a) and (c) respectively, but with smaller Y-axes ranges. [132]

Since both Nb_2CT_x and $Nb_4C_3T_x$ are expected to have the same surface composition, the existing of new peaks and the higher number of Li atoms stored in case

$Nb_4C_3T_x$ compared to Nb_2CT_x can be explained only by the differences in the electronic structure and electrical conductivity. Xie and Kent [166] found using DFT calculations that increasing the *n* value in $M_{n+1}X_nT_x$ results in different electronic structure. They showed significant changes in the density of states, DOS, at the Fermi level depending on the *n* value (higher DOS for higher *n*).[166] Also, $Nb_4C_3T_x$ exhibited 100 times higher electrical conductivity compared to Nb_2CT_x (courtesy Mr. M. Ghidiu, Drexel University).

Our previous work, on the effect of carbon additives, showed a significant increase in the Li uptake for $Ti_3C_2T_x$ when onion-like carbon was used as a conductive additive.[173] This was explained by introducing new Li intercalation sites, which become accessible only upon increasing the electrode's conductivity. Thus, there is no reason to discount the conductivity effect in this as well.

5.1.5 Carbonitride: Ti_3CNT_x compared to $Ti_3C_2T_x$

Doping nitrogen was found to be a known an approach to enhance the performance of many LIBs electrode materials such as titanium oxide [184-187] and graphene.[188-190] In case of oxides the enhancement in the performance upon N-doping was due to increase in the conductivity and the diffusion rate of Li^+.[187] Enyashin and Ivanovskii [191] found, using DFT calculations, that unlike other terminated MXenes, Ti_3CN are still metallic-like even after termination. To check the effect of nitrogen on the performance of MXenes as electrode material in LIBs, both $Ti_3C_2T_x$ and Ti_3CNT_x were tested and compared.

The CV of the first cycle for Ti_3CNT_x (orange dashed curves in Figure 30a and b) showed a large irreversible lithiation peak can be noticed around 1.1 V, in addition to two

relatively smaller peaks around 2.4 V and 0.28 V. In the subsequent cycles three reversible lithiation peaks (I), (II), and (III) around 1.6 V, 0.75 V and close to zero V respectively, were observed. The corresponding delithiation peaks (I'), (II'), and (III') were found around 2.45 V, 0.96 V, and 0.18 V, respectively.

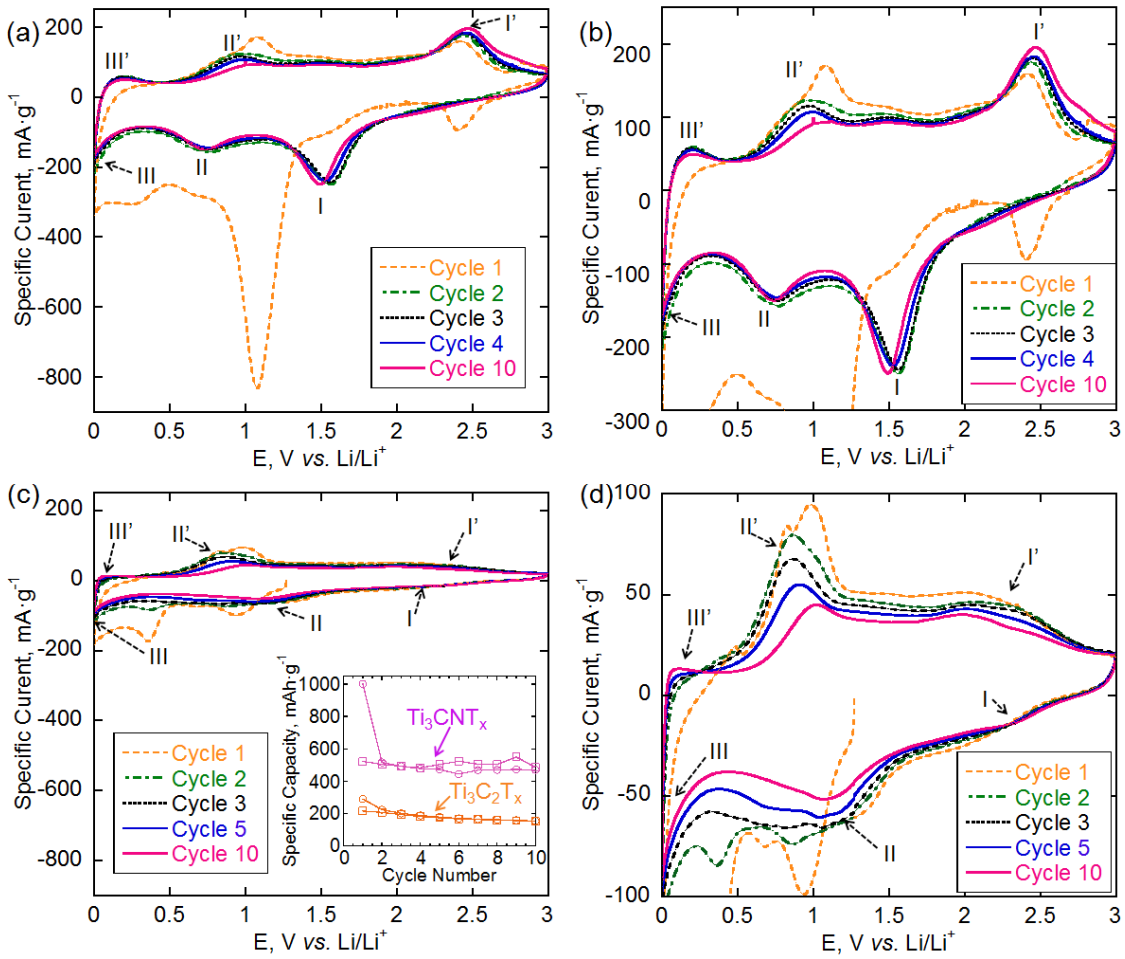

Figure 30: Cyclic voltammograms using 0.2 mV·s^{-1} for (a) Ti_3CNT_x, and (c) $Ti_3C_2T_x$. (b) and (d) are the same as (a) and (c) respectively, but with smaller Y-axes ranges.

In case of $Ti_3C_2T_x$ (Figure 30c and d) the reversible lithiation peaks (I), (II), (III) were around 2.3 V, 1 V, and close to zero V with corresponding delithiation peaks (I'), (II'), and (III') at voltages around 2.3 V, 0.9 V, and 0.1 V, respectively. It is worth noting that comparing the area of the CVs for Ti_3CNT_x (Figure 30a) and $Ti_3C_2T_x$ (Figure 30c) shows a significant difference in favor of the former for larger area. The estimated capacity from the CVs for both Ti_3CNT_x and $Ti_3C_2T_x$ is shown in the inset of Figure 30c, and it shows significant larger capacity for the carbonitride.

Figure 31a shows the voltage profile for Ti_3CNT_x at specific current of ~ 38 $mA \cdot g^{-1}$ (corresponding to *C*/8 after 15 cycles). Similar to the large irreversible peak around 1.1 V that was observed in Figure 30a, an irreversible plateau can be seen at voltage range of 1.4 - 1.2 V during the first cycle lithiation leg. The specific capacities *vs.* cycle number for both Ti_3CNT_x and $Ti_3C_2T_x$ are shown in Figure 31b.

As shown in the inset of Figure 31b, at the same cycling rate -*C*/8- Ti_3CNT_x showed two times higher capacity when compared to $Ti_3C_2T_x$ after 15 cycles (~260 $mAh \cdot g^{-1}$ for Ti_3CNT_x compared to ~130 $mAh \cdot g^{-1}$ for $Ti_3C_2T_x$). It is worth noting that to maintain the same cycling rate, much lower specific current was used for $Ti_3C_2T_x$ *viz.* 17.9 $mA \cdot g^{-1}$instead of 37.9 $mA \cdot g^{-1}$for Ti_3CNT_x. At 3*C* a specific capacity of ~130 $mAh \cdot g^{-1}$ was obtained for Ti_3CNT_x after 200 cycles.

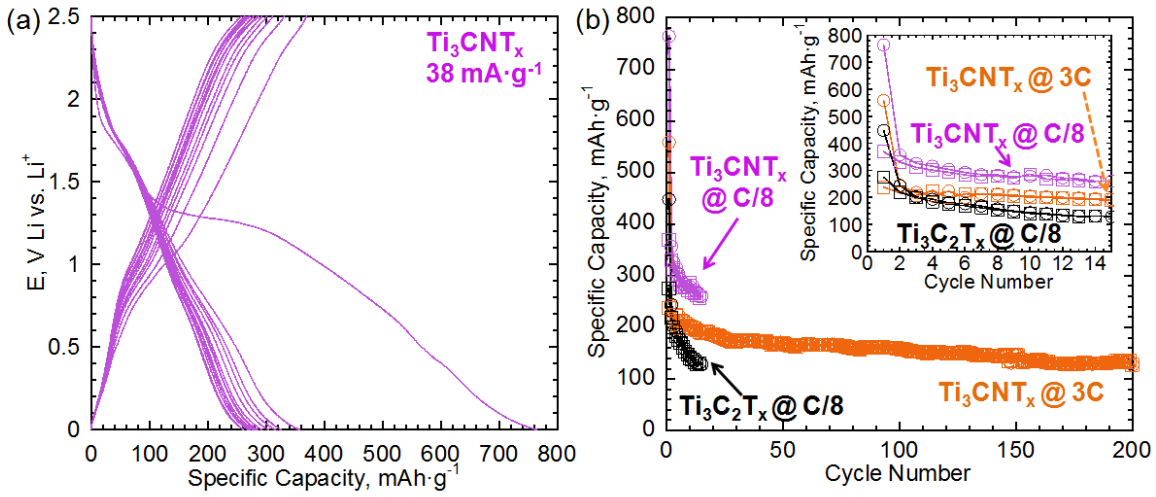

Figure 31: (a) Voltage profile for Ti_3CNT_x using a specific current of 38 $mA \cdot g^{-1}$, (b) Specific lithiation (circles.) and delithiation (squares) capacities (per mass of active material) *vs.* cycle number for Ti_3CNT_x and $Ti_3C_2T_x$ at cycling rate of C/8, and Ti_3CNT_x at 3C, the inset shows the first 15 cycles in (b).

5.1.6 M-sites solid solutions: $(Ti_{0.5},V_{0.5})_2CT_x$ compared to Ti_2CT_x and V_2CT_x

As discussed above, each MXene showed its own distinct behavior in LIBs. With the existence of M-sites solid solution MXenes (*e.g.* $(Ti_{0.5},V_{0.5})_2CT_x$ and $(Ti_{0.5},Nb_{0.5})_2CT_x$), it can be assumed that MXenes composition can be tuned to meet certain requirement. To check this assumption $(Ti_{0.5},V_{0.5})_2CT_x$ was tested and compared to its end member, *viz.* Ti_2CT_x and V_2CT_x (Figure 32). Comparing the CVs of the three phases it can be concluded that the solid solution phase has all the peaks of the end members, with no certain new peaks. In other words, $(Ti_{0.5},V_{0.5})_2CT_x$ behaves as a mixture of the end members (Ti_2CT_x and V_2CT_x).

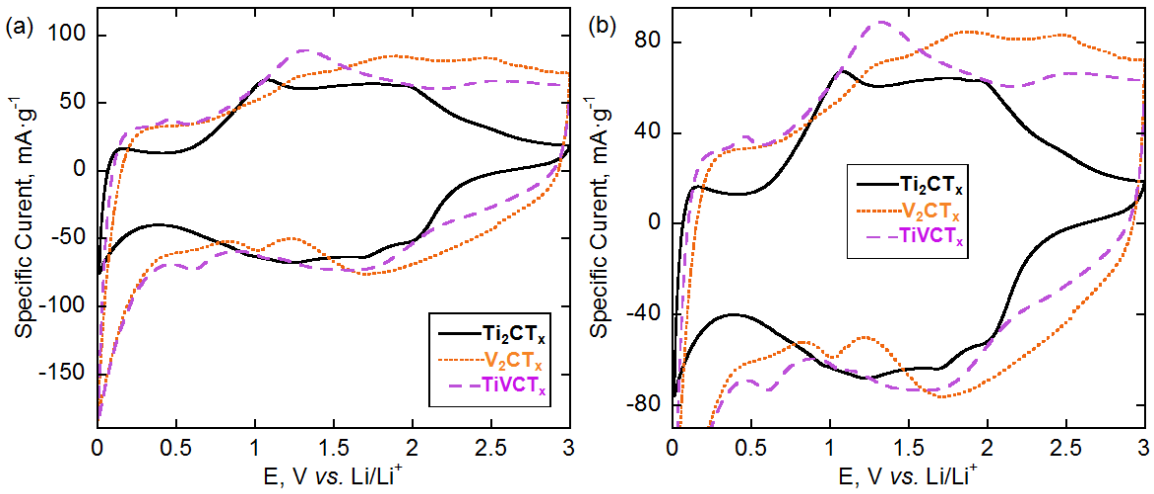

Figure 32: (a) Cyclic voltammograms using 0.2 mV·s^{-1} for the 3rd cycle of Ti_2CT_x, V_2CT_x, and $(Ti_{0.5},V_{0.5})_2CT_x$. (b) the same as (a) but with smaller Y-axis range.

5.1.7 Mo_2CT_x:

Soaking Mo_2GaC in 50% HF at RT for 96 h resulted in conversion of only ~ 17% of it into Mo_2CT_x (the conversion was estimated from EDX). The resulting material that had both MAX and MXene was tested as electrode material in LIBs (Figure 33). After 50 cycles the capacity was ~ 50 mAh·g^{-1} (per total weight of the electrode including the binder and carbon black) then the capacity started to increase gradually with cycling. This anomalous behavior was reported for multiwall carbon nanotubes (CNT) [192, 193] and it was explained by the distortion and breakage of the CNT during cycling that results in exposing new surfaces to Li. Since Mo_2GaC was not fully converted into Mo_2CT_x, it is reasonable to assume that the outer surface of some particles was partially etched. During cycling, Li intercalate between the layers of partially etched crystals and open the interlayer spacing that allow more Li to intercalate in the subsequent cycles. This explanation notwithstanding, further experimental evidences such as in situ XRD and other techniques are needed to confirm this possibility.

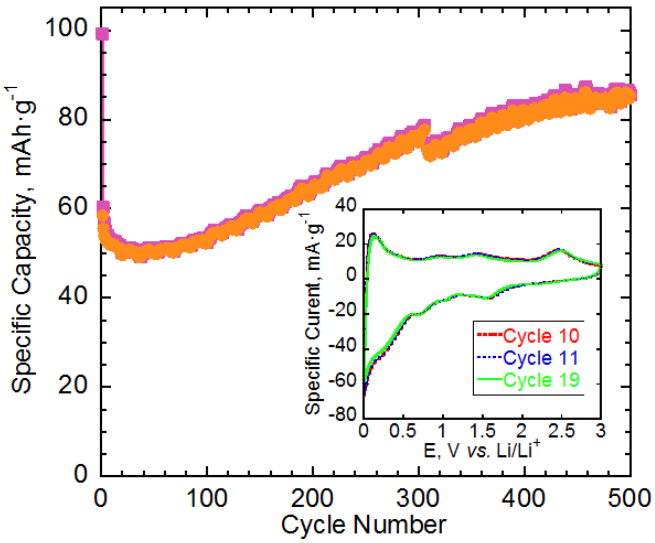

Figure 33: Specific capacity *vs.* cycle number for HF treated Mo_2GaC calculated from GC using specific current of 67.6 $mA \cdot g^{-1}$ (normalized by the weight the entire electrode) and cycled between 5 mV and 3 V *vs.* Li/Li^+. The inset shows the cyclic voltammograms for the same material cycled at 0.2 $mV \cdot s^{-1}$.

A reversible capacity of ~ 85 $mAh \cdot g^{-1}$ was obtained after 500 cycles. Assuming that carbon black contribute to the electrode by 15 $mAh \cdot g^{-1}$(the reversible capacity of carbon black electrode was about 135 $mAh \cdot g^{-1}$ at 20 $mA \cdot g^{-1}$) then the MAX/MXene mixture had a capacity of ~ 70 $mAh \cdot g^{-1}$. Since in this case the unreacted MAX phase is electrochemically inactive, the 70 $mAh \cdot g^{-1}$achieved was the contribution of only 17% of the electrode mass. It follows that the specific capacity of Mo_2CT_x exceeds 400 $mAh.g^{-1}$ at 1*C*.

5.1.8 Effect of Vacuum Annealing on the performance of Nb_2CT_x:

As discussed in section 4.7.3 annealing Nb_2CT_x at 400 °C for 40 h under high vacuum resulted in eliminating all the water from the structure. Samples before and after vacuum annealing were tested as electrode materials for LIBs. Specific currents of 99.5 $mA.g^{-1}$ and 108.5 $mA.g^{-1}$ were used to lithiate samples before and after vacuum

annealing, respectively. For delithiation, 50% higher specific currents were used (149.3 $mA.g^{-1}$ and 163.2 $mA.g^{-1}$ for samples before and after vacuum annealing respectively).[10]

The voltage profiles for the two samples are shown in Figure 34. Comparing the two voltage profiles show very small differences. For example, the vacuum annealed sample (Figure 34a) store ~ 50% of its capacity at voltages below 0.2 V while the as synthesized sample (Figure 34b) has < 40 % its capacity at the same voltage range. This difference can be due to the changes happened in the surface composition, *i.e.* converting the surface termination from $(OH)_2$ to O_2.

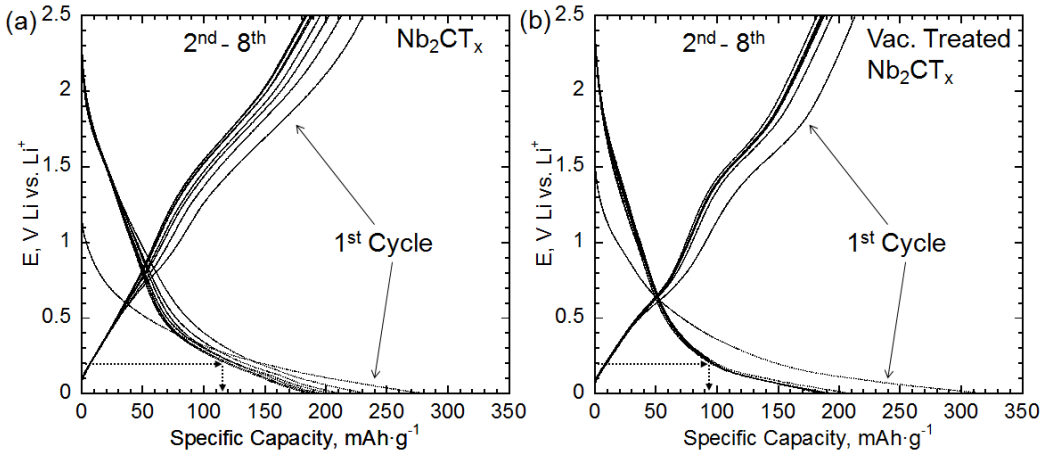

Figure 34: Voltage profiles for Nb_2CT_x *vs.* Li/Li^+ (a) before, and (b) after vacuum annealing at 400 °C for 40h

As shown in Figure 34b, the first cycle of the vacuum annealed sample showed a lithiation capacity of ~ 324 $mAh.g^{-1}$ but only 213 $mAh.g^{-1}$ was restored from electrode during delithiation which means that the 1st cycle irreversibility was about 34%. This

[10] It is recommended to use the same specific currents for comparing the performances. In our case the same current density was used instead of same specific current for reasons related to certain requirements from the funding agent of this work. However, the differences in the specific currents used for the two samples were less than 10%, so we can compare their performance at least qualitatively.

value is slightly lower than the 41% that was observed for as synthesized Nb_2CT_x (Figure 27b). It is worth noting that 1st cycle capacity for the sample with voltage profile shown in Figure 35a is not reliable since the lithiation was started at OCV of 1.2 V while it is usually higher than 1.5 V for all tested Nb_2CT_x samples. The reason for this low OCV is not clear, but it can be due to unintended short circuiting during connecting the cell to the batteries cycling machine. Also, it can be seen in the inset of Figure 35 that the 2nd cycle capacity of the sample before vacuum annealing is higher than that after vacuum annealing.

Figure 35 shows the specific capacities for the two electrodes *vs.* cycle number. The two samples- before and after annealing- showed very close capacities for the first 10 cycles, except 1st cycle. However, after 100 cycles the as synthesized sample showed a capacity of 156 $mAh.g^{-1}$ while the annealed sample had a capacity of 131 $mAh.g^{-1}$ The reasons behind this difference and the disturbance happened between cycle 35 and 80 for vacuum annealed samples are not obvious.

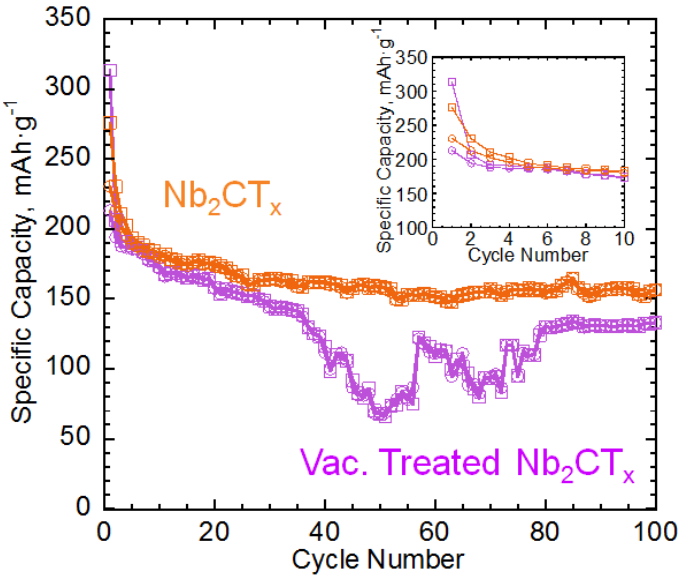

Figure 35: Specific capacities for Nb_2CT_x before and after vacuum annealing. The inset shows the first 10 cycles. Squares represent lithiation capacities, and circles represent delithiation capacities

5.1.9 Post Synthesis Treatments $Ti_3C_2T_x$:

Figure 36a shows the CVs of $Ti_3C_2T_x$ that was annealed under vacuum at 500 °C for 40 h. Compared to the CVs of the as synthesized $Ti_3C_2T_x$ (Figure 30c-d) treated, they both show very similar features but with slight differences. Three reversible lithiation peaks were observed at voltages *vs.* Li/Li^+ of 1.7 V and 0.9 V instead of 2.3 and 1 V before annealing in addition to one very close to zero volt in both cases. The change in the peaks position after annealing can be an evidence for changing the oxidation state of Ti corresponding to change in the surface chemistry.

Testing hydrazine, N_2H_4, intercalated $Ti_3C_2T_x$ [11] as electrode material in LIBs showed different features in the CVs (Figure 36b). Only two shallow reversible lithiation

[11] More details on the intercalation of hydrazine in $Ti_3C_2T_x$ can be found in elsewhere [O. Mashtalir, M. Naguib, V. N. Mochalin, Y. Dall'Agnese, M. Heon, M. W. Barsoum and Y. Gogotsi, Nat. Commun., 2013, 4, 171]

peaks were observed at 1.5 V and close to zero volt, and two delithiation peaks at 1.7 V and 1.27 V. The later appeared only after 3 cycles.

Intercalating hydroxide such as potassium hydroxide or ammonium hydroxide, NH_4OH, between $Ti_3C_2T_x$ were found to be an approach to reduce the F content.[144] Annealing ammonium hydroxide intercalated samples results in eliminating the ammonia and leaving behind oxygen terminated surface. Figure 36c shows the CVs of vacuum annealed sample after intercalation of NH_4OH.[12] The CVs are completely different compared to the as synthesized $Ti_3C_2T_x$ or treated hydrazine or annealed under vacuum. A broad lithiation peak at 1.6 V and two delithiation peaks at 1.65 and 2.1 V were observed. Lithiation peak at ~1.65 V with delithiation peak at 2.06 V were reported for anatase nanosheets.[194] The presence of anatase in the sample was confirmed by XRD shown in Figure 36d. Since the annealing was carried out under high vacuum with no source of external source of oxygen, it reasonable to assume that part of the highly oxidized surfaces converted into anatase, or leftover NH_4OH reacted with $Ti_3C_2T_x$ forming anatase. More work is needed to avoid the formation of anatase during annealing. The broad delithiation peak around 1.65 V is most likely related to the highly oxidized $Ti_3C_2T_x$ surface.

[12] NH_4OH intercalation followed by vacuum annealing was carried out by Mr. Boris Dyatkin at Drexel University

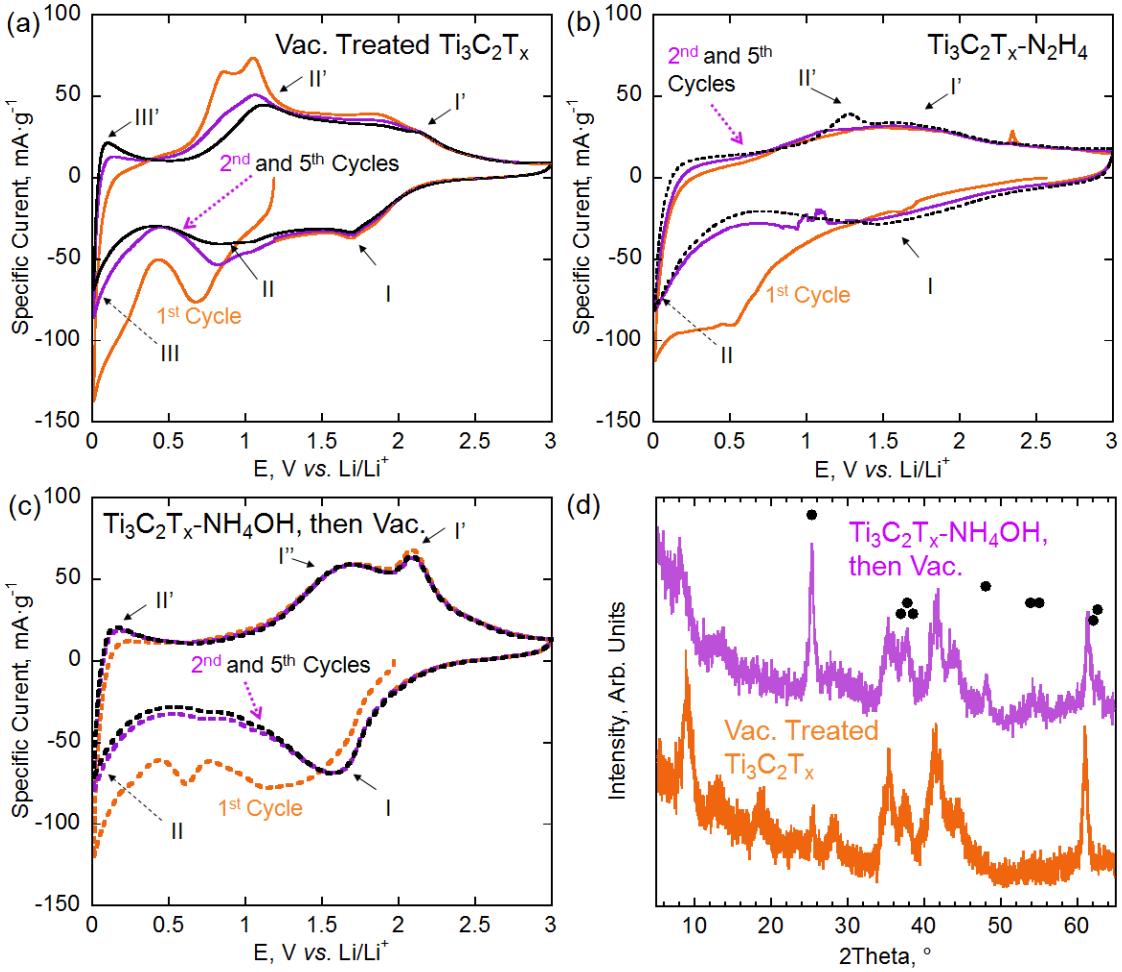

Figure 36: Cyclic voltammograms at 0.2 mV·s^{-1} for (a) vacuum annealed $Ti_3C_2T_x$ at 500 °C for 40 h, (b) hydrazine, N_2H_4, intercalated $Ti_3C_2T_x$, and (c) vacuum annealed ammonium hydroxide, NH_4OH, intercalated $Ti_3C_2T_x$. (d) XRD patterns for vacuum annealed $Ti_3C_2T_x$ at 500 °C for 40 h (bottom pattern), and vacuum annealed Ti_3C2T_x intercalated with NH_4OH (top pattern) at 450 °C. The black circles represent peaks positions of anatase [PDF#21-1272].

One of the main motivations behind testing several treated MXenes was to minimize the first cycle irreversibility. As shown in Figure 37, among different tested samples, hydrazine intercalated $Ti_3C_2T_x$ showed the least coulombic efficiency (~52%) in the first cycle. The lower efficiency in case of hydrazine compared to as synthesized $Ti_3C_2T_x$ (~74%), can be explained by the irreversible reaction between Li an dthe hydrazine that is between the layers. After vacuum annealing, the 1st cycle coulombic

efficiency was slightly higher than the as synthesized $Ti_3C_2T_x$ (79% instead of 74%). Although the NH_4OH intercalated sample that was annealed afterward showed lower efficiency than the as synthesized Ti3C2Tx, in the second cycle it showed the highest efficiency (~94%). After five cycles the coulombic efficiency of all samples reached > 95%.

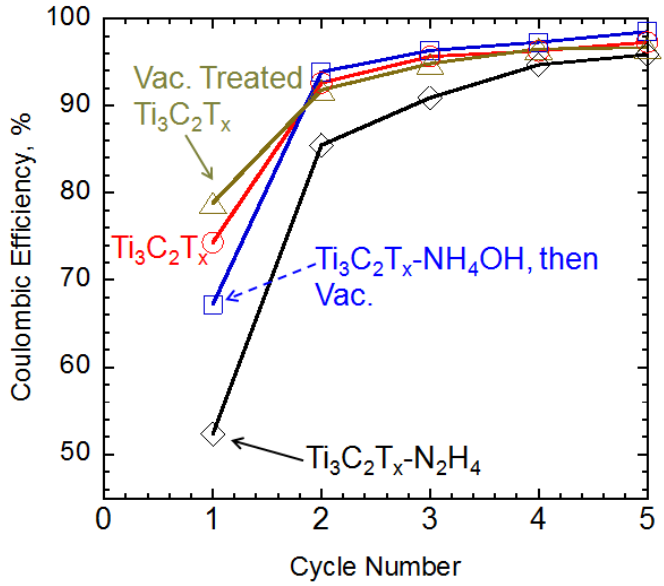

Figure 37: Coulombic efficiency of $Ti_3C_2T_x$, as synthesized (red circles), hydrazine intercalated (black diamond), vacuum annealed at 500 °C (dark olive triangles), and intercalated with NH_4OH followed by vacuum annealing at 450°C (blue squares).

5.1.10 Additive-Free Cold Pressed Electrode for High Areal Capacity:

For practical applications having anodes with high areal capacity is desired. Also, cycling below 1.0 V *vs.* Li/Li^+ where graphite can be used is important if the goal is to replace graphite in current batteries. To increase the areal capacity, Nb_2CT_x powders were cold pressed into 300 µm free-standing discs without any additives under 1 GPa at room temperature (Figure 38a) and tested between 5 mV and 1.0 V, using a lithiation

current of 0.5 mA·cm^{-2} and delithiation current of 0.75 mA·cm^{-2}. The areal capacity *vs.* cycle number obtained using the aforementioned conditions is shown in Figure 38b for two different cells with different loadings (cell I loading was 94 mg·cm^{-2}; cell II loading was 136 mg·cm^{-2}).

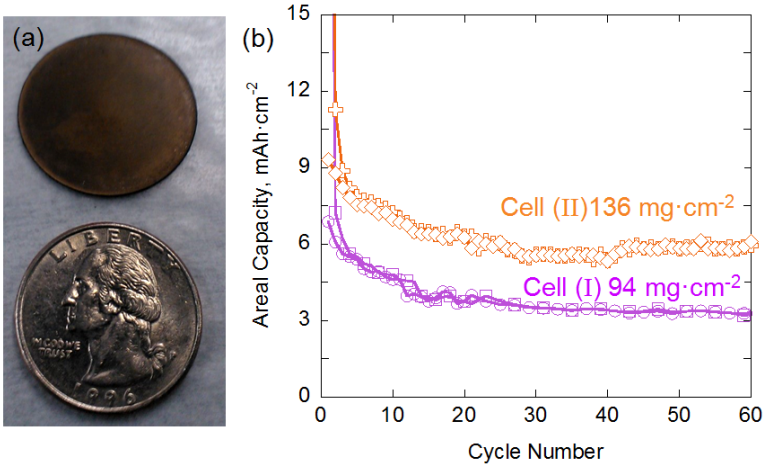

Figure 38: (a) Photograph for free-standing additive-free Nb_2CT_x disc. (b) Areal capacity *vs.* cycle number for pressed additives-free Nb_2CT_x for cells with two different loadings. Squares and crosses are for lithiation capacities, while the circles and diamonds are for delithiation capacities for two discs with loadings of 94 and 136 mg·cm^{-2}, respectively.

A reversible capacity of 3.3 mAh·cm^{-2} was obtained after 60 cycles for cell I. By increasing the loading to 136 mg.cm^{-2}, a reversible areal capacity of ~ 6 mAh·cm^{-2} was obtained after 60 cycles. The ratio of the areal capacity for the two cells was 6:3.3 which is even higher than the loading ratio for the two cells 136:94. This suggests that higher loadings can be achieved to further increase the areal capacity without deteriorating electrode performance, a crucial consideration for practical applications.

It is worth noting here that cold pressed MXenes discs were not able to handle the same high cycling rates that cast MXene electrodes were able to handle with good specific capacities. Also, the gravimetric capacities of the additive-free discs are lower

than those obtained for the cast electrodes. The lower gravimetric capacities can be explained by the lower conductivity that cold pressed discs have compared to the conventional cast electrodes that have conductive additive.

5.1.11 Delaminated MXene: d-$Ti_3C_2T_x$: [13]

As shown in Figure 39b, the capacity of the delaminated d-Ti_3C_2Tx "paper" is a factor of 4 higher than that of as-synthesized MXene. The "paper" showed a capacity of 410 $mAh \cdot g^{-1}$ at a 1*C* cycling rate (1*C* is equivalent to current density of 410 mAg^{-1}) and 110 $mAh \cdot g^{-1}$ at 36C (Figure 39b). As shown in Figure 39a, the 410 $mAh \cdot g^{-1}$ represents 3 Li per $Ti_3C_2(OH)_2$. The capacity obtained at 1C was higher than the maximum theoretical capacity of d-$Ti_3C_2T_x$ MXene predicted by Tang *et al.* using DFT (320 $mAh \cdot g^{-1}$)[195], although, the as-delaminated d-MXenes have OH and F on the surface that theoratically reduce the capacity. The reason for this mismatch is unclear at this time. However, a similar phenomenon observed on other nano-structured electrodes was explained by assuming the excess capacity was stored in a unique reversible solid electrolyte interphase (SEI).[196-198]

The results shown in Figure 39b are noteworthy since they show high Li capacities and a much better cyclabilities at 1*C* than graphite, used in commercial LIBs. For example, at 280 $mAh \cdot g^{-1}$, graphite's capacity at 1*C* is ≈ 75% of its theoretical capacity. [199] Similarly, lithium titanate is known for its capacity to handle high cycling rates. For example, at 1*C*, the capacity of $Li_4Ti_5O_{12}$ was less than 170 $mAh \cdot g^{-1}$. [200]

[13] Reproduced with permission. *Nat. Commun.* **2013** , *4* , 1716. Copyright 2013, Macmillan Publishers Ltd.

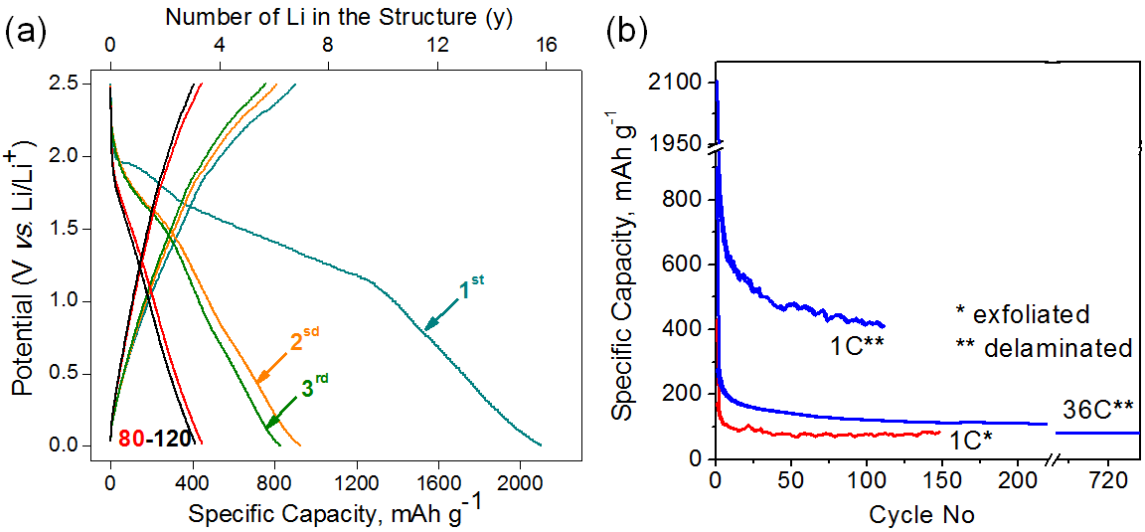

Figure 39: (a) The galvanostatic charge/discharge curves at a 1C rate for d-$Ti_3C_2T_x$, the "y" value was calculated assuming MXene chemistry of $Ti_3C_2(OH)_2$ (b) Comparison of performance of exfoliated and delaminated $Ti_3C_2T_x$ as anode material in Li-ion batteries. Reproduced with permission. [143] Copyright 2013, Macmillan Publishers Ltd.

5.2 *In situ* and *ex situ* Characterization of Electrodes

5.2.1 In situ XRD: [14]

XRD patterns were collected during lithiation -from OCV to 0 V- and delithiation -from 0 V and 3 V- of Ti_2CT_x cast electrode. The patterns shown in Figure 40 were recorded every insertion/extraction yield of y = 0.2 Li atoms upon lithiation and delithiation, using a rate of $C/10$. The virgin electrode before any cycling showed an XRD pattern (bottom blue curve in Figure 40) of unreacted Ti_2AlC and Ti_3AlC_2 together with a set of broad diffraction peaks that corresponds to Ti_2CT_x and $Ti_3C_2T_x$. During lithiation, the peaks corresponding to un-reacted Ti_2AlC (sharp peak at 2θ ~ 13°) and Ti_3AlC_2 (sharp peak at 2θ ~ 9.5°) did not change, confirming that they are electrochemically inactive. These peaks however, were useful as internal references

[14] *In situ XRD* was carried out at Université Paul Sabatier, Toulouse, France. Reproduced with permission from *J. Electrochem. Soc.*, **159**, A1368 (2012). Copyright 2012, The Electrochemical Society.

determining the position of the MXenes peaks. No extra peaks appeared during the electrochemical process, instead a reversible shift of the Ti_2CT_x diffraction peaks was observed. This result is consistent with an intercalation process of Li between the MXene layers, and no conversion reaction.

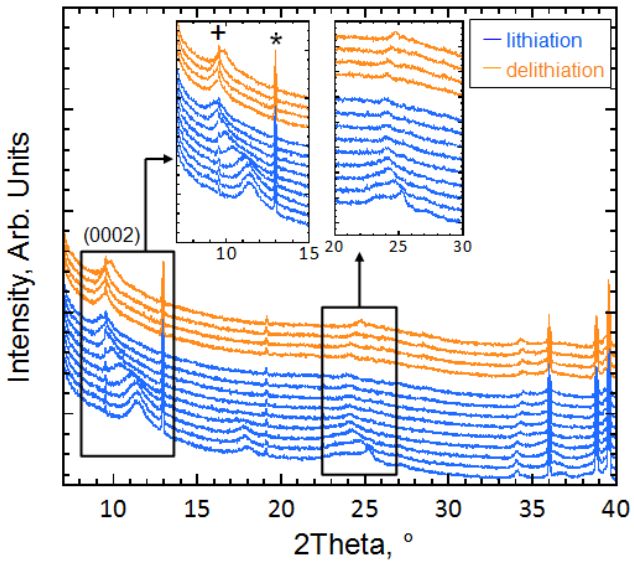

Figure 40: *In situ* XRD patterns of Ti_2CT_x collected each 0.2 Li^+ at a C/10 rate during charge and discharge, *: unreacted Ti_2AlC, +: unreacted Ti_3AlC_2. Reproduced with permission. Reproduced with permission.[201] Copyright 2012, The Electrochemical Society.

During Li insertion, the overall behavior can be divided into two domains. In the $0 < y < 0.4$ range (voltage from OCV to 1.3 V) the 0002 peak of Ti_2CT_x located at 2θ ~11.4° was not affected noticeably, while the peak located at 25° is shifted to lower diffraction angles. In the $0.4 < y < 1.4$ domain, the opposite is observed. The 25° peak can be assigned to anatase[202] that existed in the sample as a secondary phase. Comparing the relative intensities of the 0002 peak of Ti_2CT_x at 11.4° and the 25° peak shows that Ti_2CT_x is the main phase. As the domains are clearly separated, only the one corresponding to the electrochemical activity of Ti_2CT_x is detailed.

During lithiation, the progressive downshift of the 0002 peak from 2θ = 11.4° to 2θ = 9.4° corresponds to an increase of *c*-LP from 15.46 Å to 18.72 Å - 17.4% expansion - for Ti_2CT_x. During delithiation, the *c*-LP decreases to 17.96 Å, a value that is significantly higher than the value obtained during lithiation for the same Li content (Figure 41b). This can be related to the large irreversibility observed in the 1st cycle and interpreted as the trapping of Li^+ ions between the *MXene* layers. It could also be related to SEI formation between the layers not on the outer surface of the particles.

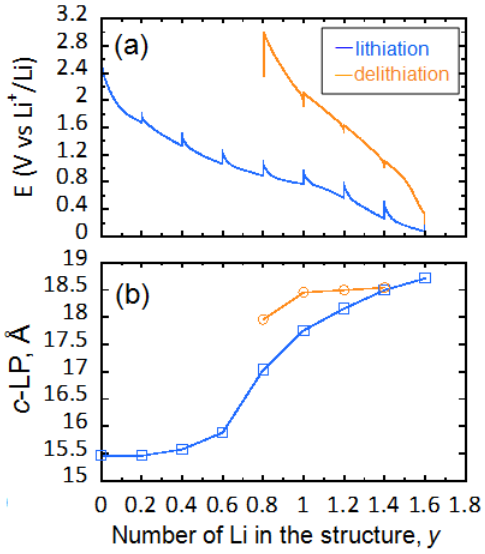

Figure 41: (a) Voltage profile during the in situ XRD study of Ti_2CT_x (b) The corresponding *c*-LP calculated from (0002) peak during lithiation and delithiation shown in Figure 40. Reproduced with permission.[201] Copyright 2012, The Electrochemical Society.

5.2.2 *In situ Dilatometry*:

In situ dilatometry results for a $Ti_3C_2T_x$ electrode (cast with 10 *wt.*% PVDF and 10 *wt.*% carbon black) during lithiation and delithiation are shown in Figure 42 and Figure 43. A current density of 77.7 $mA \cdot g^{-1}$ (based on the weight of MXene only) was

used to electrochemically cycle the electrodes while a dilatometer measured the changes in the electrode's height.

After the first lithiation cycle (Figure 42), the strain in the electrode height, *viz.* $\Delta H_{Li}/H_0$ x 100 where H_0 is the initial height of the electrode (~ 60 µm), was around 7.24%. After delithiation, the reduction in height was only ~ 2.5%. After around 20 cycles (Figure 43a), the height variations, were less than 1%.

As shown in Figure 42, the slopes of the height strain % curve (represented by inclined dashed lines) varied for different regions during the first lithiation and delithiation cycles. The changes in slopes can be evidence for different lithiation and delithiation reactions [203] or stages. [204]

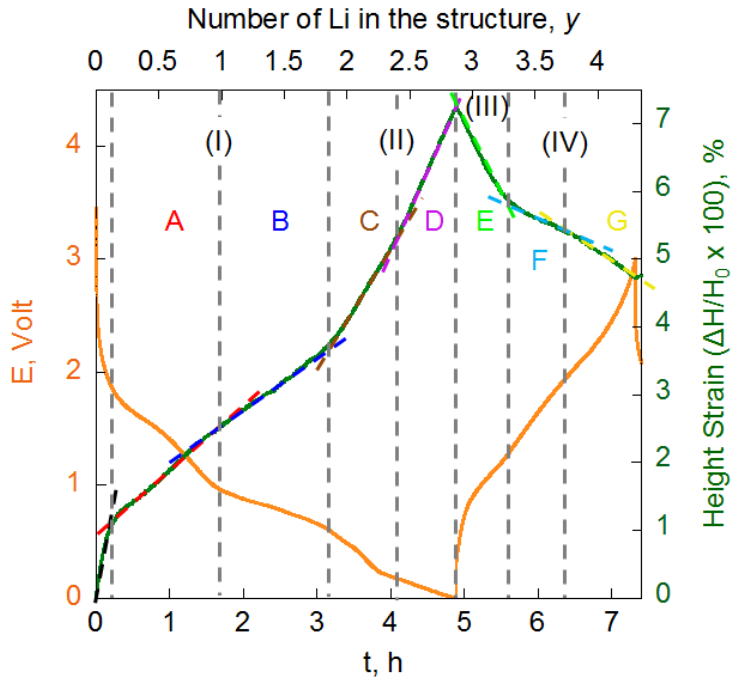

Figure 42: In situ dilatometry results for electrode height plotted as a strain in % (green curve, right side Y-axis) overlaid on corresponding voltage profile (orange curve, left side Y-axis) for the first lithiation and delithiation cycles. The number of Li ions *y* is calculated assuming the composition of $Ti_3C_2T_x$ to be Ti_3C_2OF. The dashed inclined lines represent different slopes for the height strain curve.

During lithiation, six different slopes were observed in the strain. Interestingly these coincided, with changes in slope in the voltage profile. The first one was a sharp increase in the height up to 1.1% during lithiation from the OCV to 1.9 V, with corresponding 0.11 Li per formula of Ti_3C_2OF. Similar sharp increase was reported by Ohzuku *et al.* [205] for graphite electrode; the reasons behind it are unclear. Beyond this region, four other regions labeled A, B, C, and D. The slopes in regions for A and B are close to each other; so are those of C and D. The slopes of regions A and B can be considered as one larger region (I). Similarly, regions C and D can be considered as region (II). Region (I) ends at voltage ~ 0.6 V and corresponds to the storage of 1.9 Li per Ti_3C_2OF formula unit. The total strain at the end of the region (I) is ~ 3.8%, which means that 2.7% expansion took place in region (I) alone. The expansion in region (II) was ~ 3.44% with an extra Li atom stored in the structure.

During delithiation, three slopes (E, F, and G) are observed. Slopes F and G are close to each other and significantly lower than slope E. Similar to the case during lithiation, F and G can be considered as one larger region (IV). E is a distinct region (III). In region (III) – from 0 V to 1.24 V – a ~1.45% reduction in height was obtained with extracting ~ 0.5 Li from the electrode. Delithiation from 1.24 to 3 V resulted in extracting another 0.9 Li, and a 1.05% reduction in electrode height.

Figure 43b shows the columbic efficiency *vs.* number of cycles in addition to % of reversibility in the change of the electrode's height during cycling in addition to reversibility of change in *c*-LP for the first cycle. The reversibility of the electrode height can be calculated by finding the ratio of change in electrodes height during delithiation of

a certain cycle ($\Delta H_{\text{delithiation}n}$) to the change in electrodes height during lithiation ($\Delta H_{lithiation}$) of the same cycle.

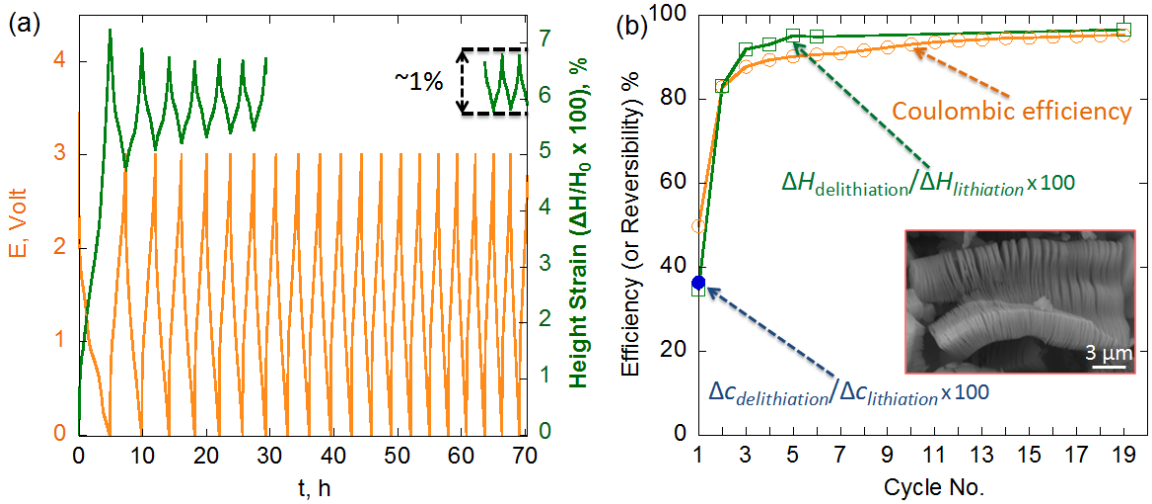

Figure 43: *In situ* dilatometry results for $Ti_3C_2T_x$ cast electrode, (a) electrode thickness expansion %, and voltage during lithiation and delithiation and, (b) coulombic efficiency [orange] and $\Delta H_{\text{delithiation}}/\Delta H_{\text{lithiation}}$ *100 [green] *vs.* cycle number. The blue point is the % of change of lattice parameter $\Delta c_{\text{delithiation}}/\Delta c_{\text{lithiation}}$ *100. The inset is a typical SEM image of $Ti_3C_2T_x$ particle; note accordion morphology.

The coulombic efficiency curve (orange curve in Figure 43b) shows good agreement with changes in $\Delta H_{\text{delithiation}}/\Delta H_{lithiation}$ (green curve in Figure 43b). *Ex situ* XRD results, however, showed that after lithiation, there was a 21.5% increase in *c*-LP, $\Delta c_{\text{Li}}/c_{\text{o}}$ where c_{o} is the *c*-lattice parameter prior to lithiation. Hahn *et al.*[204] reported, using dilatometry, an expansion of 4.2 % in height for a graphite electrode prepared in a fashion similar to ours (cast, with binder on Cu foil), while the *c*-LP expansion for graphite from XRD upon lithiation is known to be around 10 %.[206] They explained this discrepancy by the randomness of the graphite particles in the electrode. Recall, similar to graphite, the MXene expansion upon lithiation presumably only occurs along [0001]. Thus, there is no reason to exclude the randomness effect here as well. Also, the

accordion morphology of the as-synthesized MXene particles (inset in Figure 43b) allow for the accommodation of large expansions within the particle itself with minimum macro expansion for the electrode.

Furthermore, when the irreversibility of the first cycle as measured by $\Delta H_{\text{delithiation}}/\Delta H_{lithiation}$ (Figure 43a) is compared to that estimated by comparing $\Delta c_{delithiation}/\Delta c_{Li}$ (blue solid circle in Figure 43b), excellent agreement is found. In other words, most of the 1st cycle irreversibility is due to Li trapped between the MXene layers.

5.2.3 In situ XAS: [15]

To further understand the lithiation and delithiation mechanisms *in situ* XAS was performed on $Ti_3C_2T_x$ during the first lithiation and delithiation cycles (Figure 44). The Ti K-edge XANES spectra feature a relatively weak pre-edge peak, A, at ~ 4971 eV, and a strong main absorption peak, B, at around 4986 eV. Similar to transition metal oxides, the interactions in transition metal carbides involve the hybridization of the metal 3*d* and carbon 2*p* orbitals. The strong *p-d* hybridization in titanium carbides is confirmed both from band structure calculations and from experimental measurements.[207] Therefore, the first two peaks in the pre-edge, feature A, can be assigned to transitions of the l*s* electrons to the hybridized t_{2g} (Ti 3*d* + C 2*p*) and e_g (Ti 3*d* + C 2*p*) orbitals, respectively. The main absorption peak, B, is due to the dipole allowed transitions of the 1*s* electrons to unoccupied Ti 4*p* states.

The XANES for the Ti K-edge after lithiation (Figure 44b) showed a shift to lower energy, indicating a decrease in the average Ti oxidation state. Similar small shifts

[15] *In situ* XAS measurements were carried out by Dr. Xiqian Yu, Dr. Kyung-Wan Nam, and Dr. Xiao-Qing Yang at Brookhaven National Lab (BNL). Reprinted with permission from *J. Am. Chem. Soc.*. DOI: 10.1021/ja501520b. Copyright 2014 American Chemical Society.

in the XANES energy, and a reduction in the average Ti valence, were reported for amorphous titania upon the incorporation of 2.4 Li per TiO_2.[208] For nanocrystalline anatase, the shift is larger and equivalent to a reduction in valence from 4+ to 3+ due to incorporating one Li in per TiO_2.[209] After delithiation, the XANES spectrum shifted back to higher energies (higher Ti oxidation states), but *not* to the initial state. The changes during lithiation and delithiation are clear evidence for redox reactions. In agreement with our *in situ* XRD results during lithiation for a closely related MXene, Ti_2CT_x[139], there was no evidence for any Ti-conversion reactions.

The variations of the Ti edge energy during lithiation (Figure 44b) showed two distinct regions: Region I (> 0.51 V), where a continuous decrease in edge energy was observed, followed by region II (< 0.51 V), where the energy does not change with further lithiation. Similarly, during delithiation, region III showed a constant edge energy that did not change significantly with increasing voltage, followed by region IV, where the energy increased continuously with increasing voltage. It is worth noting that the boundaries for regions I, II, III, and IV observed in XANES (Figure 44) are close to those observed in dilatometric study and similarly labeled (Figure 42).

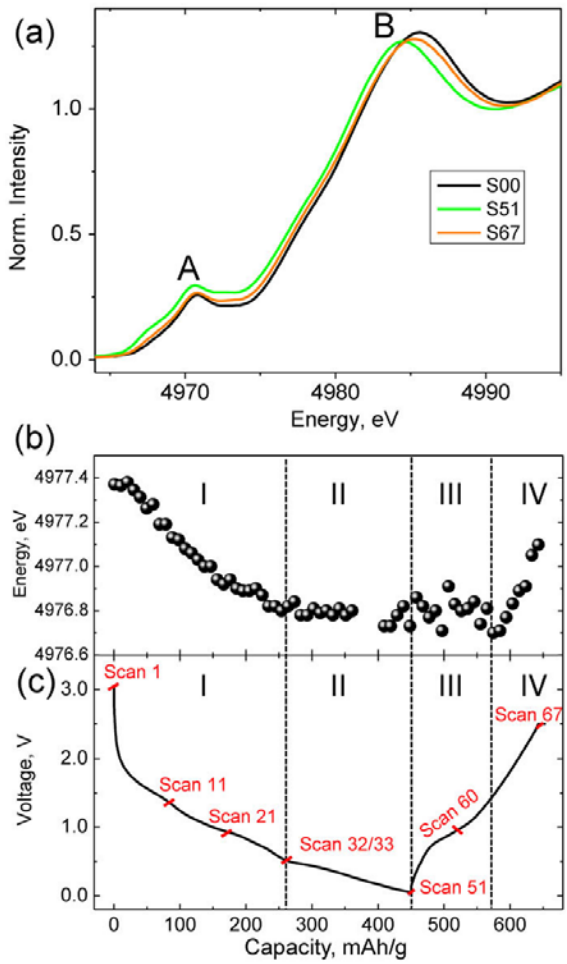

Figure 44: (a) *In situ* Ti K-edge XANES analysis during lithiation and delithiation of $Ti_3C_2T_x$, S00 is XANES before any electrochemical reactions, S51 and S67 refer, respectively, to the fully lithiated and fully de-lithiated states shown in (c). (b) Variation of Ti edge energy (at half height of normalized XANES spectra) *vs.* capacity during lithiation and delithiation combined with, (c) the corresponding voltage profiles using specific current of 36.5 $mA \cdot g^{-1}$ during lithiation and 76.8 $mA \cdot g^{-1}$ during delithiation. Reproduced with permission.[158] Copyright 2014, American Chemical Society.

It is important to note that region I ends at a voltage of 0.51 V where the corresponding capacity is 262 $mAh \cdot g^{-1}$(Figure 44c). This capacity corresponds to 1.98 Li, *i.e.* close to 2 Li, per Ti_3C_2OF. Moreover, at the end of region II the Li capacity reaches 449 $mAh \cdot g^{-1}$, which requires 1.4 extra Li per Ti_3C_2OF. Since the oxidation state of Ti is barely changed in region II (flat Ti edge energy), it is reasonable to assume that the extra

Li atoms do not *directly* interact with the Ti layers and may thus be stored on top of $Ti_3C_2OFLi_2$.

Upon delithiation, the Li capacity of $Ti_3C_2T_x$ is only 200 $mAh \cdot g^{-1}$. Since carbonate solvents were used in the electrolyte, they can be an additional source of capacity loss due to the formation of a SEI. The reduction in reversible capacity might therefore also be due to a reduction of Li diffusion due to reaction products, such as H_2O, SEI *etc.* trapped in the interlayer spaces, or at the edges. As discussed above, *in situ* XRD results for Ti_2CT_x showed an irreversible increase in the *c*-LP on lithiation, implying that there indeed are ions and/or molecules trapped between the MXene layers after the first cycle.

5.2.4 Ex situ XPS: [16]

XPS was also used to investigate Ti_3CT_x electrodes soaked in the electrolyte and electrodes that were electrochemically cycled. Since *in situ* XPS was not available to us, a the XPS spectra were recorded *ex situ*. As described in section 3.8.4, extra precautions were taken to minimize the exposure time of the electrodes to the air after electrochemical cycling and before loading into the XPS chamber.. Andersson *et al.*[210] found that exposing the electrodes to air for less than 2 minutes didn't alter their surfaces. It is worth noting that all electrode samples used in this study were sputtered using an Ar beam operating at 4 kV and 7 μA for 10 minutes, to avoid misleading information from surface contaminations.

[16] XPS measurements were carried out by Dr Kevin Cook and Mr Joseph Halim at Drexel University.

Figure 45 shows the XPS spectra for the different elements expected in the examined electrodes. As shown in Figure 45a, the Li 1s region is very close to the Ti 3s. However, a clear Li broad peak around 56.8 eV can be seen as a shoulder to the Ti 3s peak after lithiation from OCV to 1 V. The intensity of the Li peak increases and became stronger than the Ti 3s, and shifted to higher binding energy (57.3 eV) with further lithiation from 1 V to 5 mV.

Upon delithiation from 5 mV to 3 V the Li peak intensity decreased but did not vanish. Also the peak shifted back to 56.6 eV. The various components present under this peak are partially responsible for the 1st cycle irreversibility in MXene. The overlap of Li 1s with Ti 3s complicates the peak fitting of the former. However, these spectra can be used qualitatively to find out whether certain phases are present or absent. For example, Li_2O is has a Li peak at 54 eV,[211] but as shown in Figure 45a no peaks exist at this binding energy, so it can be excluded from the possible phases formed upon lithiation/delithiation.

Both Li_2CO_3 and LiOH have the same peak positions for Li 1s and O 1s at 55.2 eV and 532 eV, respectively.[211] Those peaks can be observed in MXenes electrodes after cycling (Figure 45a and e). Li_2CO_3 can be excluded due to the absence of a C 1s peak (Figure 45c) around 290 eV characteristic of the carbonate.[211] The Li 1s peak of LiF is known to be at 56.0 eV [211] which is close to the broad peak of Li that was observed upon lithiation to 1 V and exists after delithiation to 3 V (Figure 45a spectra II and IV). However, LiF can't solely explain the Li 1s peak in the tested $Ti_3C_2T_x$ electrodes specially the fully lithiated electrode (Figure 45a spectrum III) since the center of the broad Li peak is >1 eV higher than that of LiF.

Another fluoride phase *viz.* $LiPF_6$, which was used in the electrolyte, may also exist, it's Li 1s peak is at 57 eV.[212] The presence of $LiPF_6$ was confirmed by investigating the F 2s region (Figure 45d spectra II-IV) where $LiPF_6$ is known to have a peak at 688.5 eV.[212] The P 2p region (Figure 45f spectra II-IV) showed a very weak peak (notice the low peak to noise ratio) at 138 eV for $LiPF_6$, which means that the amount of $LiPF_6$ in the electrodes is quite small. Also, the intensity of $LiPF_6$ related peaks in both F 1s and P 2p regions for the electrodes after delithiation to 3V (spectra IV Figure 45d and f) is higher than those for fully lithiated electrodes (spectra III Figure 45d and f). Thus, the strong Li peak in (spectrum II Figure 45a) at 57.2 eV cannot be assigned as $LiPF_6$ only. Also, it cannot be assigned as Li in lithiated titania since the latter's peak is located at 55.3 eV in case of lithiated anatase electrodes[213] With no other possible phases – as far as I'm aware - at this binding energy, it is reasonable to conclude that this peak is related to the reversible Li adsorption on MXene. Upon delithiation the intensity of this peak decreased significantly, while a shoulder peak closer to the position of LiF and LiOH energies.

As shown in Figure 45b, there were no significant changes in the Ti 2p peaks upon lithiation or delithiation. The reason for this is not clear since change in the oxidation state of Ti was observed by *in situ* XAS, but it could be due to limited sensitivity of XPS compared to the powerful XAS. The C 1s region (Figure 45c) showed no significant changes between soaked electrode and lithiated electrode to 1 V, both showed Ti-C around 282 eV and C-C peak 284 eV that can be assigned for the carbon black that was used as a conductive additive. After lithiation to 5 mV a broad peak centered around 287 eV appeared. This peak can be assigned as a mixture of C-O-C,

C=O, and C-O-H which are located at 286.5 eV, and carboxylic groups (COOR) at 288.5 eV, those compounds were reported in the SEI of titania electrode.[214] The presence of those compounds was confirmed by investigating the O 1s region (Figure 45e).

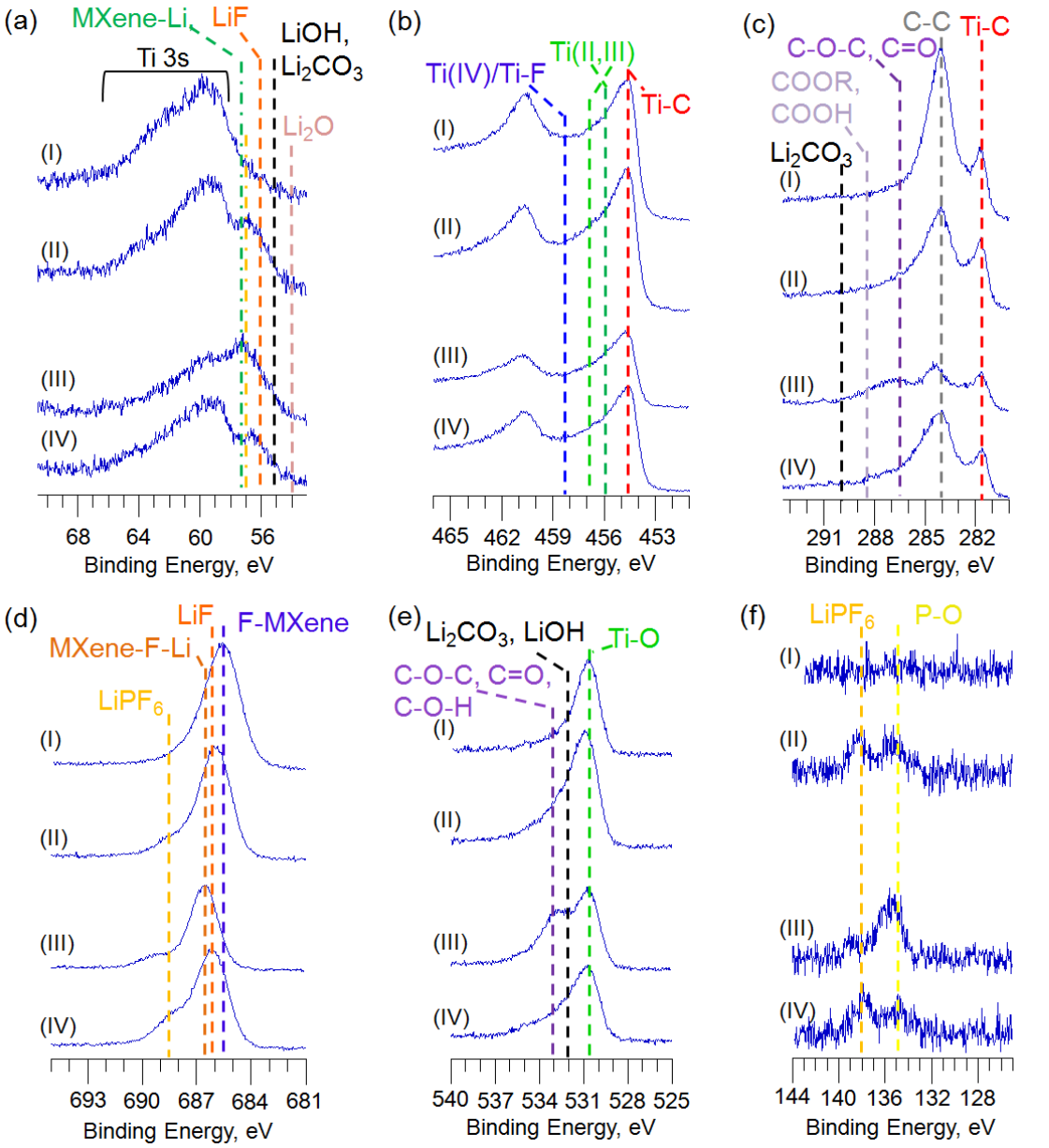

Figure 45: XPS spectra for Ti_3CT_x electrodes for regions (a) Li 1s, (b) Ti 2p, (c) C 1s, (d) F 1s, (e) O 1s, and (f) P 2p. Spectra denoted by (I) are for an electrode that was simply soaked in the electrolyte without electrochemical cycling,; those denoted by(II) are for an electrode that was electrochemically lithiated from OCV to 1 V; (III) for an electrode that was electrochemically lithiated from OCV to 5 mV and (IV) for an electrode that was electrochemically lithiated from OCV to 5 mV then further delithiated to 3V.

The F 1s region (Figure 45d) showed a shift in the F peak from 685.5 eV to 686 eV upon lithiation to 1 V and upshifted more to 686.6 eV by further lithiation to 5 mV, and after delithiation to 3 V it shifted back to the same location where it was at 1 V. At 686.2 eV, F 1s peak of LiF was reported by Eshkenazi *et al*.[215] Thus it is reasonable to assume that LiF was formed irreversible during the first cycle in the voltage range from OCV to 1 V.

Figure 46 shows XPS spectra of Li 1s region for electrodes after 8 cycles and electrodes in the first cycle.

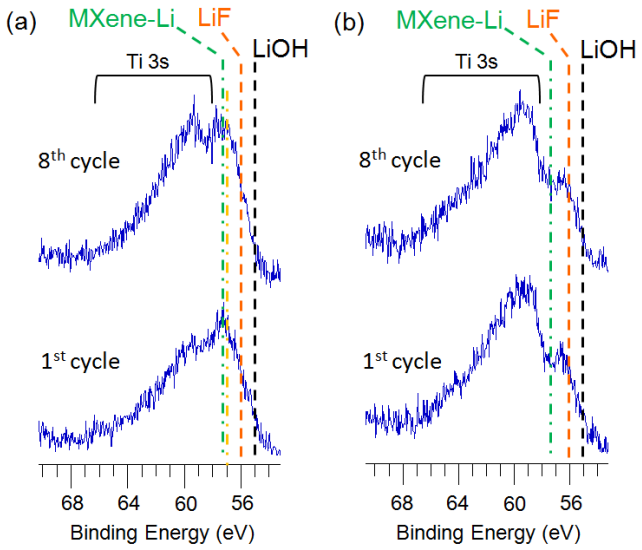

Figure 46: XPS spectra of Li 1s region for (a) electrodes fully lithiated to 5 mV, and (b) electrodes delithiated to 3 V. The bottom spectra are for 1st cycle, and the top ones are after 8 cycles.

The same Li peak at 57.2 eV was observed in Figure 46a in both cases after lithiation to 5 mV, and the intensity of this peak decreased significantly after delithiation to 3 V (Figure 46b). The absence of any changes between 1st cycle and 8th cycle is surprising, because the irreversibility in the specific capacity did not vanish completely after the first cycle

that can be seen in the coulombic efficiency curve shown Figure 43b. The reason behind this is not clear at the moment.

CHAPTER 6: SUMMARY AND OUTLOOK

In this work, a new family of 2D materials, comprised of early transition metal carbides and carbonitrides was produced by selectively etching the A layers from the $M_{n+1}AX_n$ - so called MAX - phases using HF at room temperature. The replacement of the strong primary A-M bonds in the MAX phases with O, OH and F surface terminations (the mixed terminations are referred to collectively as T_x) converts a 3D crystalline – albeit a layered–solid to a collection of 2D flakes that are typically stacked, but can also be delaminated. Sonication can be used to separate 2D $M_{n+1}X_nT_x$ layers from each other and produce single-layer and few-layered flakes. Sonication also results in nanoscrolls with inner radii of less than 20 nm.

This new family of 2D materials was labeled "MXenes" to denote the loss of the A-element from the MAX phases and emphasize their 2D structure and similarity to graphene. MXenes from different sub MAX phase groups were produced including M_2AX, M_3AX_2, M_4AX_3, solid solutions on the M-sites and a carbonitride. The following MXenes were synthesized:

M_2XT_x: Ti_2CT_x, Nb_2CT_x, V_2CT_x, Mo_2CT_x, $(Ti_{0.5},Nb_{0.5})_2CT_x$, $(Ti_{0.5},V_{0.5})_2CT_x$,

$M_3X_2T_x$: $Ti_3C_2T_x$, $(Ti_{0.5},V_{0.5})_3C_2T_x$, $(V_{0.5},Cr_{0.5})_3C_2T_x$, Ti_3CNT_x,

$M_4X_3T_x$: $Ta_4C_3T_x$, $Nb_4C_3T_x$, and $(Nb_{0.5},V_{0.5})_4C_3T_x$.

The yield of the synthesis process is high, and the process is simple and readily scalable. Also, the exfoliated MXenes have long shelf lifes if stored in a dry environment, but delaminated MXenes oxidize if stored in water for a long time. The synthesis process

of MXenes from MAX phases appears to be affected by the synthesis conditions of the latter.

XPS and EDX results indicate that MXenes are terminated with a mixture of O, OH and/or F groups. The as-synthesized MXenes are simultaneously electronically conducting and hydrophilic and relatively stable in aqueous environments, a rare combination indeed.

The changes in the *c*-LPs upon converting the MAX phases into MXenes was found to vary from one phase to another. Some MXenes showed large increase in the *c*-LP (> 6Å) due to the intercalation of water and possibly etching products between the MXenes' layers. The water can be eliminating by vacuum annealing at elevated temperatures. For example, annealing Nb_2CT_x under vacuum at 400 °C resulted in eliminating all the water from between the layers.

The space between the MXene sheets is extremely versatile and amenable to a host of compounds. For example, $Ti_3C_2T_x$ can be intercalated with various organic molecules, as well as, inorganic salts dissolved in water. Sonication of DMSO intercalated $Ti_3C_2T_x$ in deionized water resulted in large-scale delamination of the MXene layers into single- and few-layer MXene. Filtration of the latter results in thin, free-standing MXene "paper" that is flexible and conductive.

Outlook on the Synthesis of MXenes Front:

As described above, some of the etching by-products can coexist with the MXene after etching the A element. The effects of these etching reaction by-products and surface

contaminations on the performance and properties of various MXene layers need to be well investigated understood and ultimately controlled.

Other synthesis techniques need to be explored. For example, it would be beneficial to identify etchants that are less dangerous/toxic than HF. The use of non-aqueous etchants could, in principle, avoid O or OH terminations of the MXene sheets. All the MXenes reported in this work were synthesized from Al contained MAX phases, except Mo_2C that was produced from Mo_2GaC, but the latter was not fully converted into MXene. . Furthermore, the etching of A-elements other than Al needs to be explored to cover all possible transition metals carbides that form the MAX phases. For example, Al-containing Mo, Zr and Hf-based MAX phases currently do not exist. If other A elements can be etched from the MAX phases, it would be possible to synthesize MXenes based on these metals. The recent discovery of a Mn_2GaC magnetic MAX phase [216] is an exciting development. The possibility of obtaining 2D magnetic flakes is thus in principle feasible.

Experimentalists working with this emerging family of 2D materials should focus on addressing the following:

- Controlling and modifying MXenes' surfaces.
- Establishing the exact structure of $M_{n+1}X_nT_x$ as a function of T and x.
- Detailing and understanding the structure and properties of MXenes intercalated with various compounds.
- Determining the chemical and thermal stabilities of MXenes in different environments.
- Large-scale delamination of MXenes other than $Ti_3C_2T_x$.

- Finding alternative, robust, and safe routes of MAX phase exfoliation and MXene delamination.
- Synthesizing MXenes without surface functional groups.
- Direct gas phase synthesis of single-layer MXene films.
- Characterizing single-layer MXenes including electronic, magnetic, optical, thermal, and mechanical properties.
- Exploring MXenes in various applications, such as composite reinforcement, catalysis, transparent electronic conductors, sensors, *etc.*
- Expanding the family through synthesis of new MXenes.

Success in addressing these points should lead to numerous practical applications. These comments notwithstanding, the discovery of MXenes is an exciting development that greatly expands the 2D materials universe.

MXenes in LIBs:

MXenes were tested as electrode materials in LIBs. They showed an excellent ability to handle high cycling rates, with good gravimetric capacities. Among the investigated compounds, in exfoliated form (after HF etching and before sonication), V_2CT_x showed the highest capacity (280 $mAh \cdot g^{-1}$ at a rate of 1*C* and 125 $mAh \cdot g^{-1}$ at a rate of 10*C*). Although Nb atoms are heavier than Ti, the gravimetric capacity of Nb_2CT_x is higher than that for Ti_2CT_x at the same cycling rates (180 $mAh \cdot g^{-1}$ for Nb_2CT_x versus 110 $mAh \cdot g^{-1}$ for Ti_2CT_x at 1*C*). The carbonitride, *viz.* Ti_3CNT_x showed higher capacities than its carbide counterpart. $Nb_4C_3T_x$ showed more Li uptake than Nb_2CT_x per formula, but gravimetrically the latter had higher capacity. $Ta_4C_3T_x$ showed active delithiation

peaks at voltages higher than 3 V *vs.* Li/Li^+. HF treated Mo_2GaC showed an anomalous increase in capacity with increasing number of cycles. Areal capacities as high as of 6 $mAh \cdot cm^{-2}$ was obtained for additive-free cold pressed Nb_2CT_x electrodes. Additive-free paper of delaminated $Ti_3C_2T_x$ yielded a reversible capacity of 410 $mAh \cdot g^{-1}$ at 1*C* (~ 4 times higher than the capacity of cast $Ti_3C_2T_x$ film), and possessed an excellent ability to handle extremely high cycling rates (110 $mAh \cdot g^{-1}$ at 36 *C* after 200 cycles).

Although the MXenes' gravimetric capacities are not as high as Si,[217] they have the great advantage of combining high cycling rates with good capacities. The cycling rates were as good as, and probably better than, lithium titanium oxide based anodes.[175] Considering the rich chemistry of MXenes and solid solutions possibilities, it is may be in principle possible to fine tune and design them for specific battery applications. Thus some MXenes could function as anodes and some could be used as cathodes for lithium ion and other batteries.

In situ XRD, XAS, and dilatometry in addition to *ex situ* XPS were used to investigate the lithiation and delithiation mechanisms of MXene. It was found that the electrochemical lithiation and delithiation are due to redox intercalation and deintercalation reactions with no signs for any conversion reactions.

Both *in situ* XAS and dilatometry of $Ti_3C_2T_x$ exhibited two distinct regions during lithiation and delithiation of the first cycle. The first region during lithiation was from OCV to 0.51 V for XAS, and from OCV to 0.6 V for dilatometry, with corresponding ~ 2 Li stored in the structure. In this region XAS showed a reduction of the oxidation state of Ti upon lithiation while the second region showed no change in the oxidation state of Ti. Dilatometry showed slow expansion in the first region compared to the second one. Total

expansion in the first cycle was ~ 7.24% and after 20 cycles the reversible variation in thickness was ~ 1%. The irreversibility in the electrode's thickness during the first cycle was almost equal to the irreversibility in the *c*-LP and very close to the coulombic efficiency. Thus, it was concluded that the irreversibility was due to compounds trapped between the MXene layers.

XPS showed reversible Li 1s peak at 57.2 eV that was related to lithiated MXene. Formation of LiF, in addition to LiOH, in the first lithiation cycle was confirmed by XPS, and they are believed to have contributed to the firs cycle irreversible capacities observed for MXene. Also, evidence for the formation of carboxylic and carbonates in the SEI below 1 V was observed.

Outlooks on MXenes in LIBs:

All the work to date on MXene electrodes in LIBs was carried out on as-synthesized materials; no tailoring of their surface terminations was explored. Thus, many opportunities for enhancing the performance and reducing first cycle irreversibilities remain unexplored. For example, bare MXenes surfaces are predicted to perform better than terminated ones in LIBs.[165] First cycle irreversibility is a challenging problem in all tested MXenes so far. This problem, in principle, can be solved by pre-lithiation of the MXene electrodes, similar to what was reported for other nanostructured systems.[180] Also since MXenes are a new system for electrode materials, the optimum electrolyte has not established and needs to be studied to minimize the first irreversibility in addition to enhancing the stability over longer lifetime. Delaminating other MXenes may increase their Li uptake, similar to what was found for $Ti_3C_2T_x$.

The excellent capability to handle high cycling rates and the shape of the voltage profiles suggest MXenes to be excellent electrode materials for Li-ion capacitors.

APPENDIX A: DETAILED RESULTS ON MOLTEN SALTS TREATMENTS AND NON-AQUEOUS FLUORINATION OF MAX PHASES

A.1 Molten Salt Treatments:

Immersing bulk sample of Ti_2AlC in molten potassium fluoride, KF, for 2 h at 900 °C in air resulted in formation of a gray crust that flaked off very easily. XRD pattern of the sample's surface after treatment (Figure A1a) shows very strong peaks of K_3AlF_6 in addition to small amount of titanium carbide. The cross-sectional SEM image for the Ti_2AlC sample after the KF treatment (Figure A1b) shows a ring around the sample. The EDX of that ring showed mainly grains of titanium oxycarbide with no aluminum, in addition to potassium aluminum fluoride (the charging grains in the SEM). It is worth noting that the sample was rectangle but the reacted edges fall off.

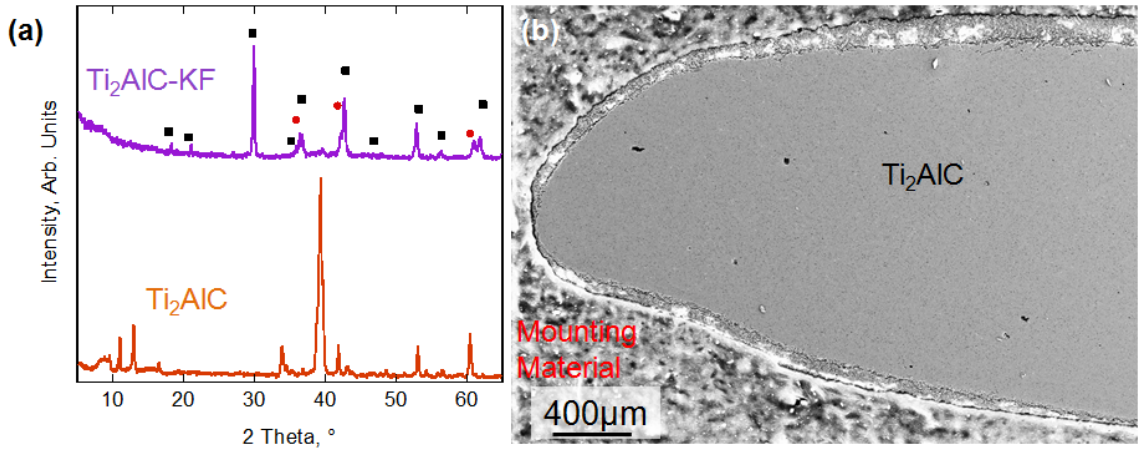

Figure A1: (a) XRD patterns for the surface of Ti_2AlC bulk sample before (bottom orange curve) and after KF treatment at 900 °C for 2 h (top purple curve). The black squares represent peaks position of K_3AlF_6 [PDF#03-0615], while the red circles represent TiC [PDF#32-1383] peaks position. (b) Cross-sectional SEM image for Ti_2AlC after KF treatment (900 °C for 2 h).

The same KF treatment was carried out but using Ti_2AlC powders instead of bulk followed by washing the fluoride salt allowed. Figure A2 shows TEM images after the KF treatments, in addition to unwashed salts, nano rods with diameter of ~ 5 nm were observed (Figure A2b).

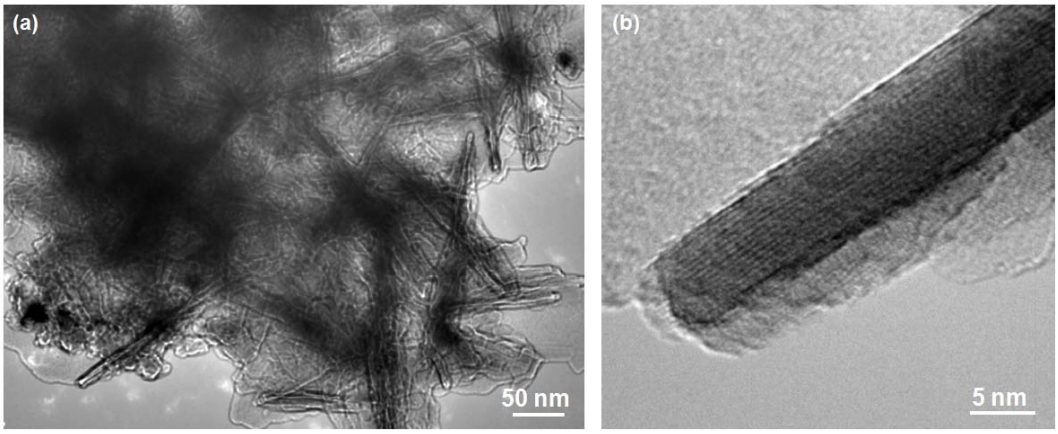

Figure A2: (a) TEM image for Ti_2AlC powders after KF treatment at 900 °C for 2h. (b) High magnification TEM image for one of the nano rods observed in (a).

Figure A3 shows the XRD patterns for bulk Ti_3SiC_2 sample before and after soaking in cryolite, Na_3AlF_6, at 1000 °C for 2 h or 4 h in air. After 2 h the XRD pattern shows coexistence of large amount of titanium carbide with Ti_3SiC_2. After 4 h, the XRD pattern for the surface of the sample showed that almost all the Ti_3SiC_2 was converted into titanium carbide.

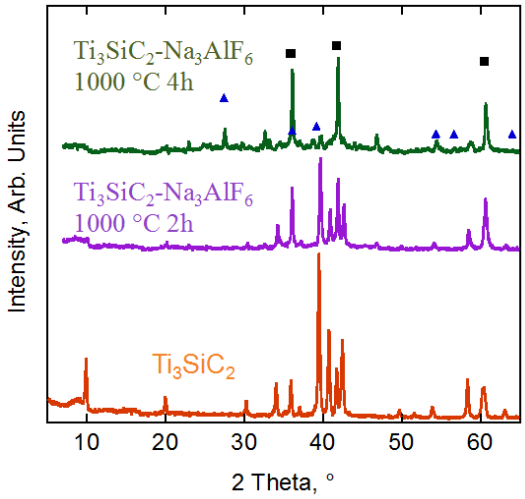

Figure A3: XRD patterns for bulk Ti_3SiC_2 before and after soaking in cryolite at 1000 °C for 2 h and 4 h. The while the black squares represent peaks position of TiC [PDF#32-1383], an the blue triangles represent peaks position of rutile [PDF#34-0180].

A.2 Nonaqueous Fluorination

Figure A4 shows the XRD patterns before and after fluorination using 5% F_2 at 200 °C for Ti_2AlC, Ti_3AlC_2, Ti_2SC, and Ti_3SiC_2. In all the cases, MAX phases were the dominant phases after the treatments. No changes were observed in the 0002 peak of Ti_2AlC and Ti_3AlC_2 (insets of Figure A4 a and b, respectively).

After F_2 treatment of Ti_2SC (Figure A4c), a low intensity peak located very close to the peak position of $TiOF_2$ was observed. Although, the fluorination process was carried out in an oxygen-free environment, formation of oxyfluoride may be formed due to a reaction between titanium fluorides formed during fluorination and oxygen in the air during handling the sample after fluorination. In case of Ti_3SiC_2, the XRD pattern (inset in Figure A4d) after fluorination showed a split in the 0002. The reason behind this split is not clear at the moment and needs further investigation.

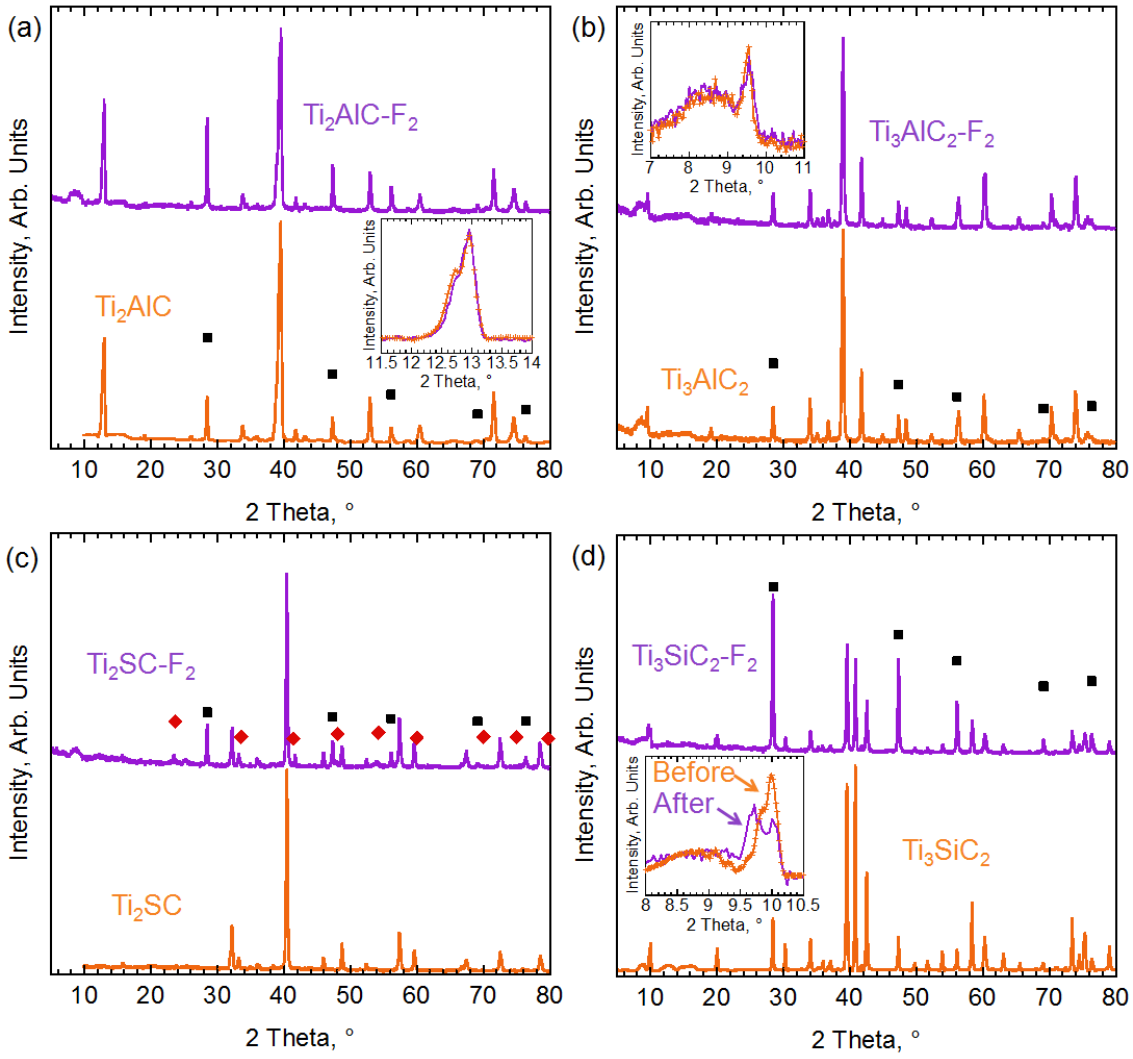

Figure A4: XRD patterns before (bottom orange curves) and after (top purple curves) F_2 treatment at 200 °C for 2 h (a) Ti_2AlC, (b)Ti_3AlC_2, (c) Ti_2SC, and (d) Ti_3SiC_2. The inset in (a), (b) and (d) shows smaller range o2 Theta showing the 0002 peak for MAX phases. The black squares represent the peaks for position for Si that was used as an internal reference. The red diamonds represent the peaks position of $TiOF_2$ [PDF#08-0060].

As shown in Figure A5, treating Ti_2SC and Ti_3SiC_2 using anhydrous HF for 1 h at 100 °C and 75 °C, respectively, resulted in formation of TiF_3. Also, unreacted MAX phases coexisted with the TiF_3.

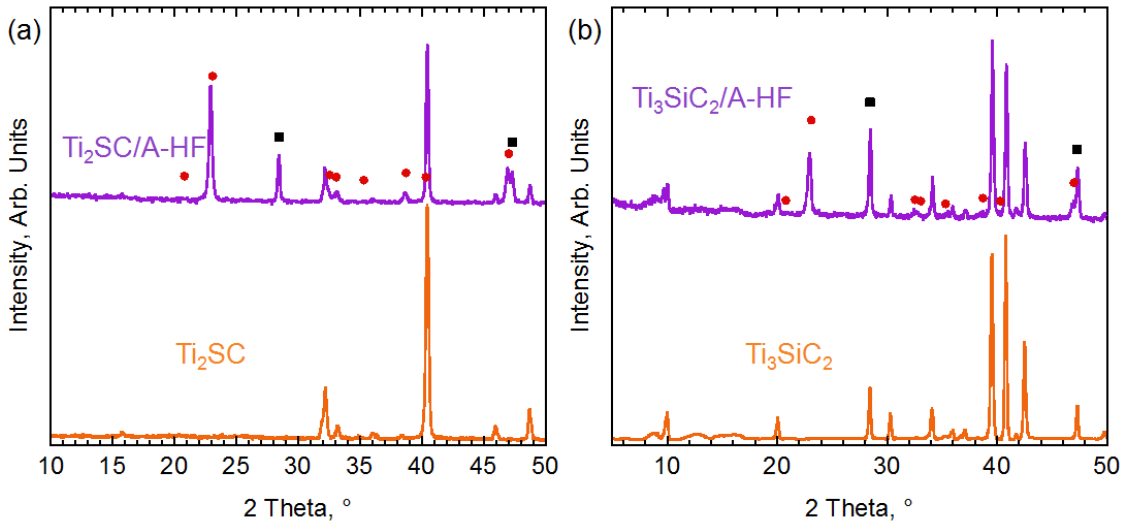

Figure A5: XRD patterns for (a) Ti_2SC before and after anhydrous hydrogen fluoride, A-HF, treatment at 100 °C for 1 h, (b) Ti_3SiC_2 before and after anhydrous hydrogen fluoride, A-HF, treatment at 75 °C for 1 h. The black squares represent peaks position of Si, the red circles represent peaks position for TiF_3 [PDF#37-1062].

The XRD patterns of Ti_3AlC_2 before and after A-HF treatment at 100 °C for 1h are shown in Figure A6. A broad peak around 2θ of 23.5° appeared after the treatment. This peak can be, partially, assigned to TiF_3 and $TiOF_2$. As shown in the inset of Figure A6, this peak overlaps with the peak of Ti_2AlF_9 that was produced by A-HF treatment of Ti_2AlC at 55 °C for 2 h.[124] Thus, formation of Ti_2AlF_9 cannot be discounted in case of Ti_3AlC_2.

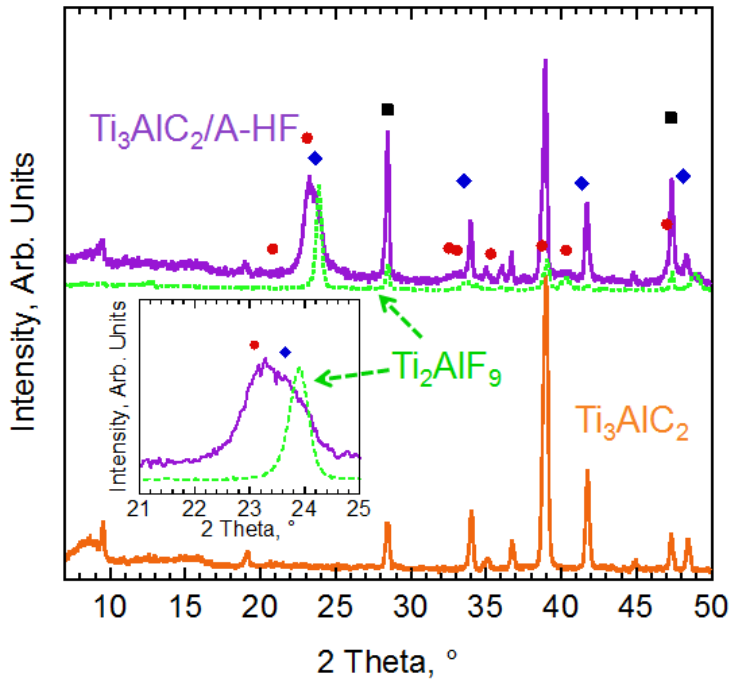

Figure A6: XRD patterns for Ti_3AlC_2 before (bottom orange pattern) and after (top purple pattern) A-HF treatment at 100 °C for 1 h. The dashed lemon green curves represent the XRD pattern of Ti_2AlF_9 produced by A-HF treatment of Ti_2AlC at 55 °C for 2h. The black squares represent peaks position of Si, the red circles represent peaks position for TiF_3 [PDF#37-1062], and the blue diamonds represent the peaks position of $TiOF_2$ [PDF#08-0060].

APPENDIX B: MORE UNSUCCESFULL ATTEMPTS TO PRODUCE MXENES AND DISCUSSION BASED ON THERMODYNAMIC CALCULATIONS

B.1 More Unsuccessful Attempts:

Many reagents were used to treat different MAX phases. Table B1 shows the conditions used for each experiment, using different reagents other than HF, and the corresponding *wt.* loss % and the outcomes from XRD analysis. In all the cases MAX phases peaks were observed after the reactions. No MXene peaks were observed in any of them.

Table B1: MAX phases treated with several reagents, other than HF, with the corresponding weight loss, and the outcomes from XRD

MAX Phase	Condition (conc., temp., and time)	~ *wt.* loss %	Outcome from XRD
Ti_2AlC	10% HCl, 50 °C, 69 h	22%	No changes in the MAX phase structure, and no new peaks
	15% HCl, 50 °C, 39 h	23%	
	37% HCl, 50 °C, 2 h	13%	
	37% HCl, 50 °C, 4 h	12%	
	37% HCl, 50 °C, 13 h	13%	
	60% Aqua Regia, RT, 5 min	95%	
	30% Aqua Regia, RT, 15 h	80%	
	18% Aqua Regia, RT, 15 h	34%	
	12% Aqua Regia, RT, 18 h	25%	
	50% NaOH, RT, 65h	20%	
	5% HNO_3, RT, 15 h	11%	
	20% HNO_3, RT, 15 h	50%	Small broad peak of anatase coexisted with MAX phase peaks
	69% HNO_3, RT, 18 h	75%	
Ti_3AlC_2	15% HCl, 50 °C, 39 h	10%	XRD showed no changes in the structure and no new peaks
	37% HCl, 50 °C, 39 h	10%	XRD showed no changes in the structure and no new peaks
	37% HCl, 50 °C, 69 h	15%	XRD showed no changes in the structure and no new peaks
	50% NaOH, RT, 16 h	5%	XRD showed no changes in the structure and no new peaks

Treating $(Nb,Zr)_2AlC$ using hydrofluoric acid (50 % for 70 h) resulted in forming small amount of MXenes in addition to unreacted MAX phases but EDX showed no Zr in the MXene particles. It is not clear whether the resulted MXene has vacancies in the M sites where Zr used to be, or all the Zr contained $M_{n+1}X_n$ layers were dissolved and the noticed MXene is only a result of etching Al from Nb_2AlC that may have segregated during synthesis of $(Nb,Zr)_2AlC$. Further work is needed to confirm any of those options. Forming MXene layers with high concentration of vacancies in the M site would be very interesting for many applications.

Immersing Cr_2AlC in 50% HF at RT resulted in dissolving the powder completely. As shown in Figure B1, when the concentration was reduced to 20% and soaked for18 h at RT, hydrated chromium trifluoride, $CrF_3{\cdot}3H_2O$, was formed and coexisted with unreacted Cr_2AlC. The *wt.* loss after this treatment was ~ 70%.

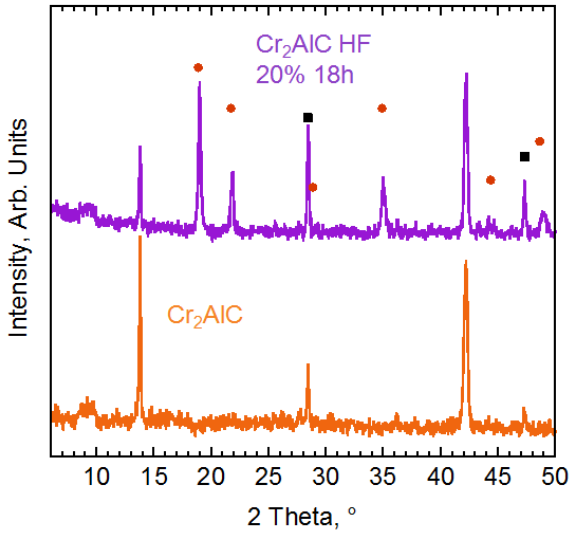

Figure B1: XRD patterns for Cr_2AlC before and after HF treatment at RT for 18 h using 20% HF. The black squares represent the peaks position of Si that was used as an internal reference, and the red circles represent the peaks positions of $CrF_3{\cdot}3H_2O$ [PDF#01-0300].

When Hf_2InC was immersed in 50% HF at RT an exothermic reaction took place and everything was dissolved except indium, In, that agglomerated forming metal beads similar to what was observed for Ti_2SnC. When the concentration was reduced to 10% at RT, after 18 h the *wt.* loss was more than 90%. The XRD pattern (Figure B2) after the treatment showed no more MAX phase, but HfC that existed as secondary phase in the starting material, in addition to HfO_2 and unreacted In and graphite. It is unlikely to form graphite at room temperature, thus it is reasonable to assume that graphite existed in the starting MAX phase.

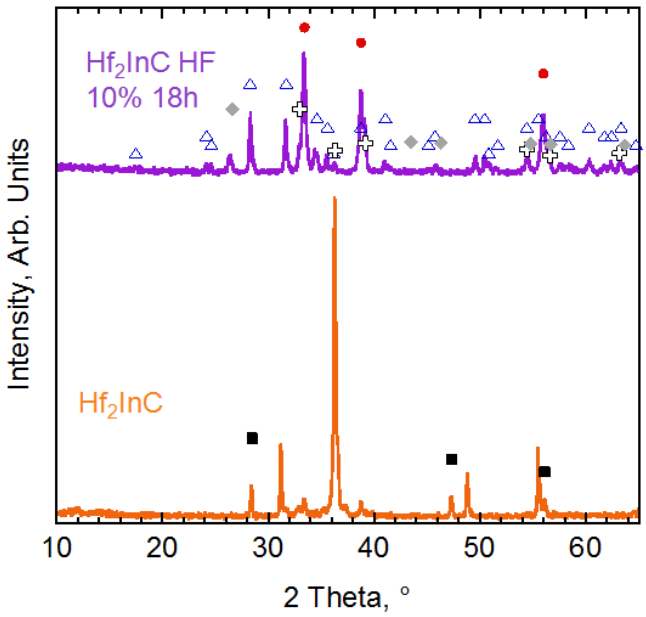

Figure B2: XRD patterns for Hf_2InC before and after treatment using 10% HF at RT for 18h. The black squares represent the peaks position of Si that was used as an internal reference, the red circles represent the peaks positions of HfC [PDF#09-0368], blue triangles are for HfO_2 [PDF#06-0318] peaks position, crosses for In [PDF#05-0642], and grey diamonds are for graphite [PDF#26-1079].

Although attempts to produce Ti_2NT_x from Ti_2AlN were not successful, interesting structures were obtained. After immersing T_2AlN in 10% HF for 18 h at RT,

and during washing using DI water the color of the suspension turned from semitransparent to whitish (milk-like) with increasing the pH. The XRD pattern (Figure B3a) of the resulted materials showed small broad peak of anatase that coexisted with Ti_2AlN peaks. However SEM images (Figure B3b) did not show any conventional particles of Ti_2AlN, only flowerlike particles were covering everything. So it is reasonable to assume that all the Ti_2AlN were covered with this nanostructure. The high magnification SEM image shown as an inset in Figure B3b, showed that those flowerlike particles consist of nanosheets. Similar anatase morphology was reported by Fang *et al.*[218] They produced this morphology by hydrothermal treatment of butyl alcohol with water, titanium(IV) butoxide and HF at 200 °C for 20 h.

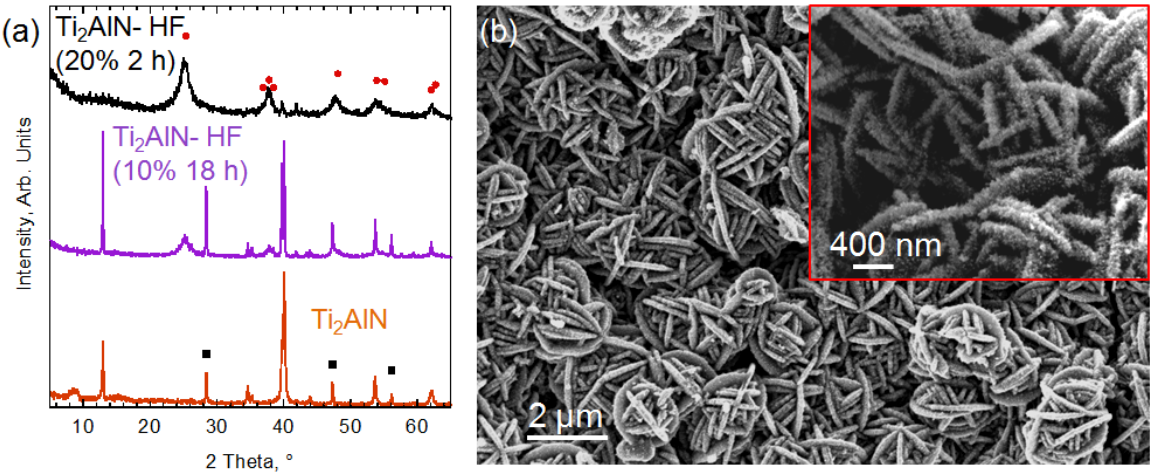

Figure B3: (a) XRD pattern of Ti_2AlN before (bottom orange pattern) and after HF treatments at RT using 10% HF for 18 h (middle purple pattern), and 20% HF for 2 h. The black squares represent peaks positions for Si that was used as an internal reference, while red circles represent the peaks positions of anatase [PDF#04-0477]. (b) SEM image for the sample that was treated using 10% HF for 18 h at RT. The inset shows higher magnification image for the same sample.

As shown in Figure B3a, by increasing the concentration of HF to 20 % and holding for 2 h only at RT, almost the Ti_2AlN was reacted and the XRD showed mainly

nanocrystalline anatase. There are two possible mechanisms for the formation of this structure. The first is simply dissolving of Ti_2AlN and during washing anatase crystallized and the process was catalyzed by the presence of F and N. The second mechanism is formation of Ti_2NT_x MXene upon etching the Al (EDX showed no Al after the HF treatment) from the Ti_2AlN and during washing and with increasing the pH, the Ti_2NT_x layers deflocculate/delaminate and then oxidize in water. More work is needed to find experimentally the certain mechanism behind this reaction. It is worth noting that if the second mechanism is the dominant, then in principle synthesis of $Ti_{n+1}N_nT_x$ is possible by avoiding using any oxidant in the washing step.

B.2 Discussion of Experimental Observation and Outlook for Future Experiments Based on Thermodynamics Calculations:

FactSage, thermochemical software, was used to calculate the Pourbaix (E *vs.* pH) diagrams. Only M and A atoms in MAX phases were included in the calculations due to limitation in number of variables allowed by the software. All the calculations were done at room temperature, 1 atm pressure. No kinetics calculations were considered. M and A atoms were behave as metals in the solution. The resulted transition metal compounds from the calculations was assumed to be the surface termination in case of MXene, if this compound is known to be soluble in water or acid[17] then no MXene of this transition metal is expected. If it was known to be stable in water and acid, then the corresponding MXene is expected to be stable. With all those assumptions, and since there is no

[17] Unless other references are cited, the information regarding the solubility of the formed compounds was extracted from: W. M. Haynes, ed., *CRC Handbook of Chemistry and Physics, 94th Edition*, Taylor & Francis, internet version, 2014.

tabulated thermodynamics data for MAX phases, the results shown here can be used only as a guiding tool for chemical and electrochemical treatments of MAX phases to synthesis MXenes, not to draw very concrete conclusions. This is a promising tool for finding the conditions needed to remove or replace F or O termination in MXene. For example, according to the predicted diagram (Figure B4), at voltages below -0.8 V, F termination is unstable in case of Ti contained MXene.

Figure B4 shows the E *vs.* pH diagrams for Ti-Al and Ti-Sn. Since all the experiments were carried out at 0 V, and the pH of HF was around 1, it is reasonable to compare the different diagrams at those conditions. For Ti-Al system, TiF_3 and AlF_3 are expected to exist at those conditions. While TiF_3 is insoluble in water AlF_3 is soluble (0.5 g /100 mL). It is worth noting that $AlF_3 \cdot 3H_2O$ was found in case of poorly washed MXene after HF treatment (Figure 24a). Contradicting with the calculations, the EDX of Ti contained MXenes, *viz.* Ti_2CT_x and $Ti_3C_2T_x$, showed -in addition to F- a significant amount of O (F:O ~ 1:1). Xie *et al.* [158] predicted, using theoretical calculations, that F termination in MXene is not stable in water and convert to OH termination.

In case of Ti-Sn system, TiF_3 and SnO_2 are expected to present in the system. SnO_2 is neither soluble in water nor acids. Although TiF_3 is not soluble in water, it is soluble in concentrated acids. If no F in the solution was consumed to form any tin fluoride compounds, then the concentration of the solution would be stay high, and TiF_3 may dissolve. This may explain the large *wt.* loss and the absence of MXene when Ti_2SnC was immersed in HF. The formation of Sn metal beads due to HF treatment cannot be explained using the thermodynamic calculations presented here. However, formation of SnO_2 may be hindered by kinetics of the reaction. According to Figure B4b,

to form soluble tin fluoride compound at 0 V, the pH needs to be reduced to values lower than 0.25.

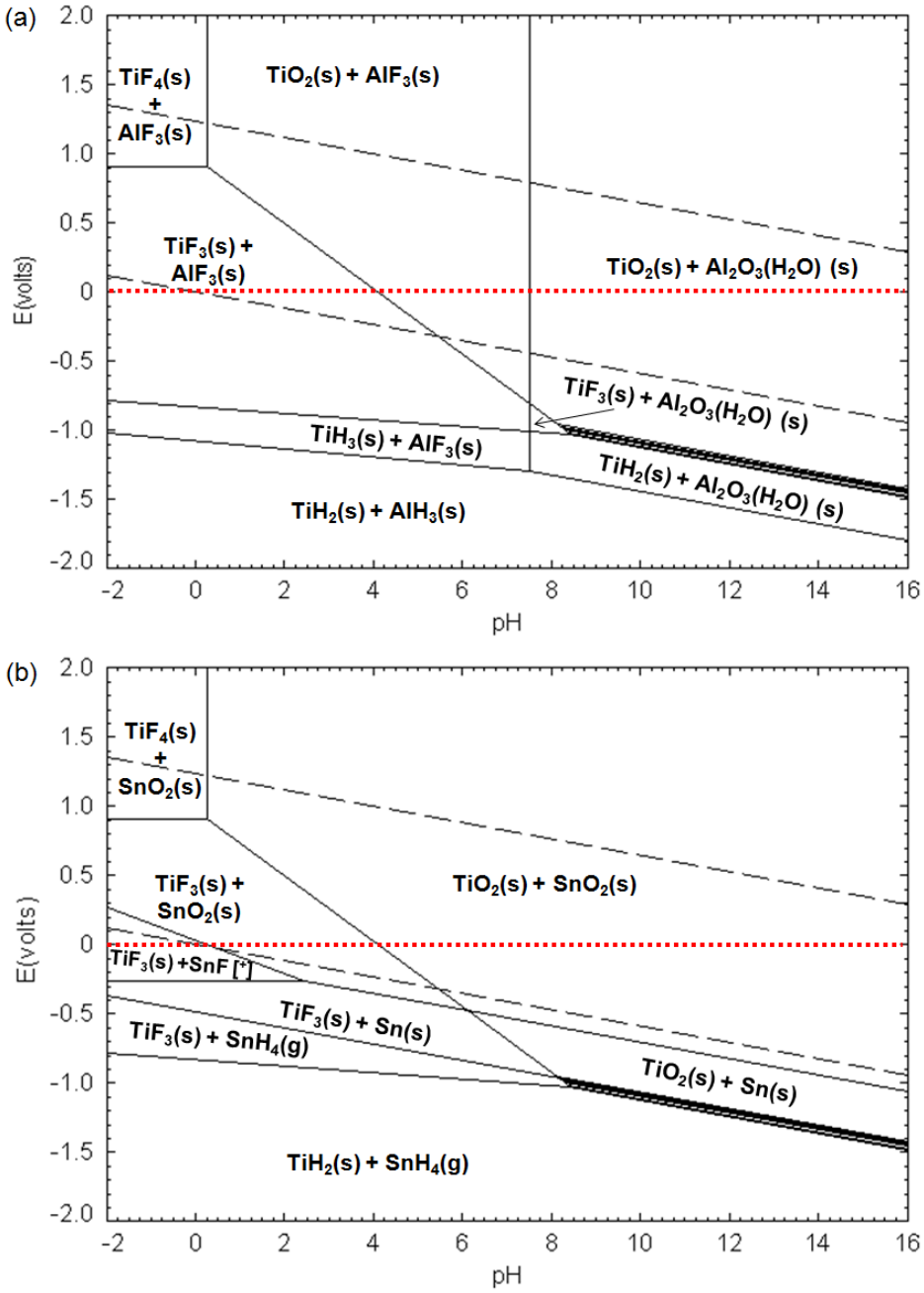

Figure B4: Pourbaix diagrams calculated using FactSage for (a) Ti-Al-F-H_2O and (b) Ti-Sn-F-H_2O at m F^{-1} = 0.1 mol/kg and under 1 atm pressure at room temperature. The horizontal red dotted line is an eye guide for the 0 V which is the condition at which all the chemical treatments were carried.

The E *vs.* pH diagram for Hf-In-F-H_2O system showed (Figure B5a) that at 0 V and pH below 2.25, HfF_4 and dissolved In are expected to be in the system. Considering that HfF_4 is highly soluble in HF, [219] then the large *wt.* loss observed in case of Hf_2InC and absence of MXene is justified. However, the presence of In metal after the reaction contradict with the calculations shown here.

As shown in Figure B5b, at 0V and pH values lower than 4.5, ZrF_4 and AlF_3 are the expected phases. ZrF_4 is known to be soluble in water (1.5 g /100 mL) even more soluble than AlF_3. This may explain the reason behind dissolving the Zr in case of $(Nb,Zr)_2AlC$. Based on Figure B5b , in principle, Zr contained MXene could be stable if the pH increased to >4.5 forming ZrO_2 surface that is insoluble in water, or by conducting electrochemical etching at negative potentials < -0.9 V to form hydrogenated surface that is insoluble in water as well.

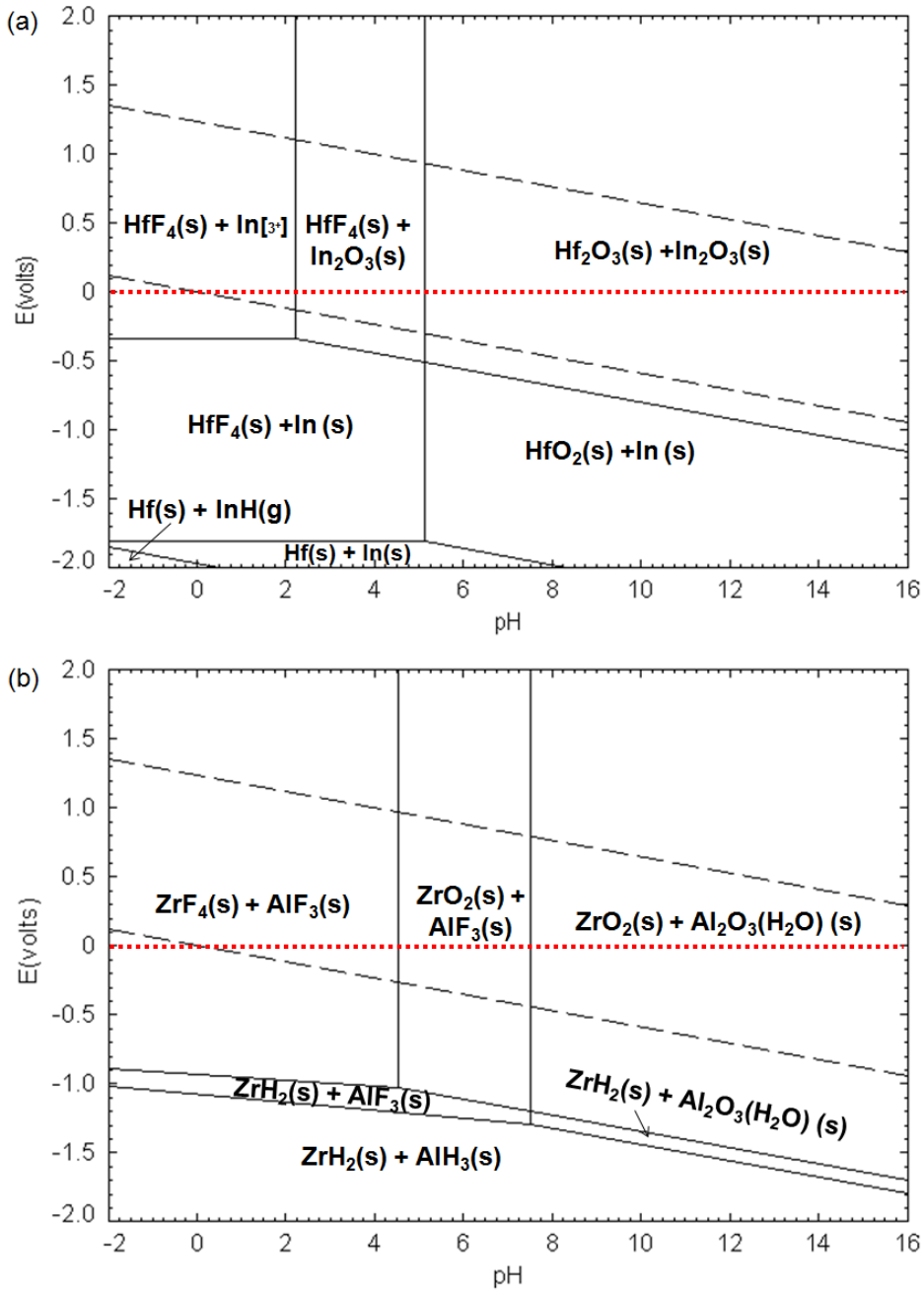

Figure B5: Pourbaix diagrams calculated using FactSage for (a) Hf-In-F-H_2O and (b) Zr-Al-F-H_2O at m F^{-1} = 0.1 mol/kg and under 1 atm pressure at room temperature. The horizontal red dotted line is an eye guide for the 0 V which is the condition at which all the chemical treatments were carried.

Figure B6a shows the Pourbaix diagram for Cr-Al-F-H_2O system. AlF_3 and dissolved chromium ions are expected to be in the system at 0V and pH below 2.8. This may explain the difficulty to synthesis Cr contained MXene using HF.

At 0 V and pH of 1, MoO_2 is expected to exist (Figure B6b) which is known to be insoluble in water and acids, which means in principle that synthesis of Mo contained MXene using HF is possible. Those voltage and pH conditions are located exactly at the border between GaF_3 region and dissolved gallium compound. The former is insoluble in water or HF.[220] So it is reasonable to assume that once GaF_3 was formed in the outer layers of Mo_2GaC particles, it hinders the continuation of the etching reaction toward the center of the particle. This may explain why only 17% MXene was the maximum conversion of Mo_2GaC into Mo_2CT_x using HF. According to Figure B6b, it is expected to form a soluble Ga compound if the pH increases slightly higher than 1 or electrochemically at voltages below - 0.3 V.

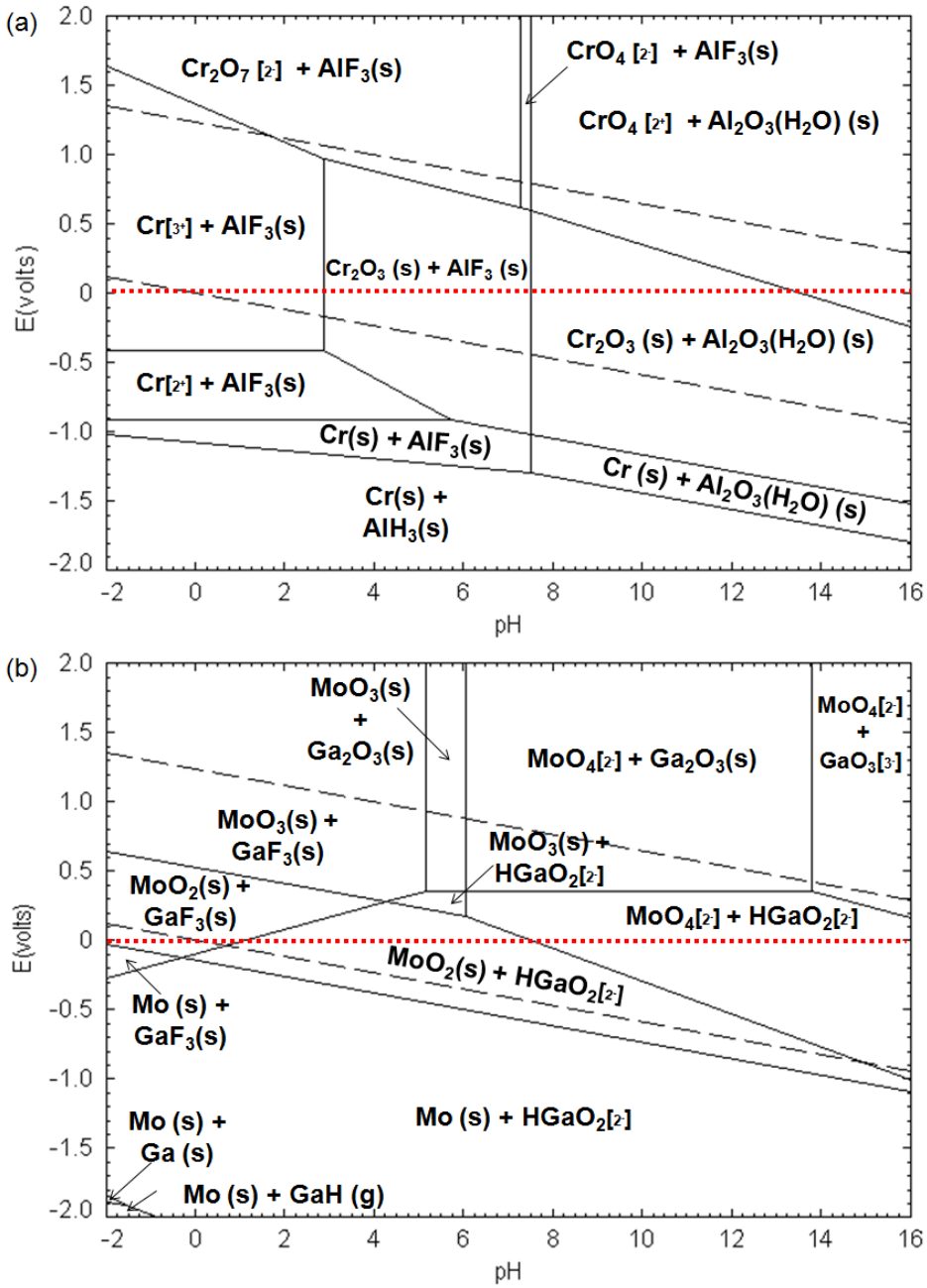

Figure B6: Pourbaix diagrams calculated using FactSage for (a) Cr-Al-F-H_2O and (b) Mo-Ga-F-H_2O at m F^{-1} = 0.1 mol/kg and under 1 atm pressure at room temperature. The horizontal red dotted line is an eye guide for the 0 V which is the condition at which all the chemical treatments were carried.

LIST OF REFERENCES

[1] K. S. Novoselov, A. K. Geim, S. V. Morozov, D. Jiang, Y. Zhang, S. V. Dubonos, I. V. Grigorieva, A. A. Firsov, *Science* **2004**, *306*, 666.

[2] F. Yavari, N. Koratkar, *The Journal of Physical Chemistry Letters* **2012**, *3*, 1746.

[3] D. Jariwala, V. K. Sangwan, L. J. Lauhon, T. J. Marks, M. C. Hersam, *ACS Nano* **2014**, *8*, 1102.

[4] X. Peng, L. Peng, C. Wu, Y. Xie, *Chemical Society Reviews* **2014**.

[5] M. D. Stoller, S. Park, Y. Zhu, J. An, R. S. Ruoff, *Nano Letters* **2008**, *8*, 3498.

[6] J. Liu, X.-W. Liu, *Advanced Materials* **2012**, *24*, 4097.

[7] S. Stankovich, D. A. Dikin, G. H. Dommett, K. M. Kohlhaas, E. J. Zimney, E. A. Stach, R. D. Piner, S. T. Nguyen, R. S. Ruoff, *Nature* **2006**, *442*, 282.

[8] H. Kim, A. A. Abdala, C. W. Macosko, *Macromolecules* **2010**, *43*, 6515.

[9] F. Gao, *Materials Today* **2004**, *7*, 50.

[10] A. H. C. Neto, K. Novoselov, *Materials Express* **2011**, *1*, 10.

[11] K. S. Novoselov, D. Jiang, F. Schedin, T. J. Booth, V. V. Khotkevich, S. V. Morozov, A. K. Geim, *Proceedings of the National Academy of Sciences of the United States of America* **2005**, *102*, 10451.

[12] J. N. Coleman, M. Lotya, A. O'Neill, S. D. Bergin, P. J. King, U. Khan, K. Young, A. Gaucher, S. De, R. J. Smith, I. V. Shvets, S. K. Arora, G. Stanton, H.-Y. Kim, K. Lee, G. T. Kim, G. S. Duesberg, T. Hallam, J. J. Boland, J. J. Wang, J. F. Donegan, J. C. Grunlan, G. Moriarty, A. Shmeliov, R. J. Nicholls, J. M. Perkins, E. M. Grieveson, K. Theuwissen, D. W. McComb, P. D. Nellist, V. Nicolosi, *Science* **2011**, *331*, 568.

[13] R. Ma, T. Sasaki, *Advanced Materials* **2010**, *22*, 5082.

[14] K. Chen, Z. Bao, *Journal of Nanoparticle Research* **2012**, *14*, 1.

[15] M. W. Barsoum, *MAX Phases: Properties of Machinable Ternary Carbides and Nitrides*, John Wiley & Sons, **2013**.

[16] I. Salama, T. El-Raghy, M. W. Barsoum, *Journal of Alloys and Compounds* **2002**, *347*, 271.

[17] H. B. Zhang, Y. C. Zhou, Y. W. Bao, M. S. Li, J. Y. Wang, *Journal of the European Ceramic Society* **2006**, *26*, 2373.

[18] M. W. Barsoum, T. El-Raghy, M. Ali, *Metallurgical and Materials Transactions A* **2000**, *31*, 1857.

[19] M. Naguib, V. N. Mochalin, M. W. Barsoum, Y. Gogotsi, *Advanced Materials* **2014**, *26*, 992.

[20] M. W. Barsoum, M. Radovic, in *Encyclopedia of Materials: Science and Technology* (Eds.: K. H. J. Buschow, W. C. Robert, C. F. Merton, I. Bernard, J. K. Edward, M. Subhash, V. Patrick), Elsevier, Oxford, **2004**, pp. 1.

[21] E. N. Hoffman, G. Yushin, T. El-Raghy, Y. Gogotsi, M. W. Barsoum, *Microporous and Mesoporous Materials* **2008**, *112*, 526.

[22] Z. M. Sun, *International Materials Reviews* **2011**, *56*, 143.

[23] A. K. Geim, K. S. Novoselov, *Nature Materials* **2007**, *6*, 183.

[24] S. Mouras, A. Hamwi, D. Djurado, J. C. Cousseins, *Revue de Chimie Minerale* **1987**, *24*, 572.

[25] B. C. Brodie, *Philosophical Transactions of the Royal Society of London* **1859**, *149*, 249.

[26] D. D. L. Chung, *Journal of Materials Science* **1987**, *22*, 4190.

[27] in *Nobelprize.org* The Royal Swedish Academy of Sciences, **2010**.

[28] G. Yongji, S. Gang, Z. Zhuhua, Z. Wu, J. Jeil, G. Weilu, M. Lulu, Y. Yang, Y. Shubin, Y. Ge, V. Robert, X. Qianfan, H. M. Allan, I. Y. Boris, L. Jun, L. Zheng, M. A. Pulickel, *Nature Communications* **2014**, *5*, 3193.

[29] J. Zupan, D. Kolar, *Journal of Physics C: Solid State Physics* **1972**, *5*, 3097.

[30] D. Pacilé, J. C. Meyer, Ç. Ö. Girit, A. Zettl, *Applied Physics Letters* **2008**, *92*.

[31] A. Ueno, T. Fujita, M. Matsue, H. Yanagisawa, C. Oshima, F. Patthey, H. C. Ploigt, W. D. Schneider, S. Otani, *Surface Science* **2006**, *600*, 3518.

[32] J. C. Garcia, D. B. de Lima, L. V. C. Assali, J. o. F. Justo, *The Journal of Physical Chemistry C* **2011**, *115*, 13242.

[33] K. Takeda, K. Shiraishi, *Physical Review B* **1994**, *50*, 14916.

[34] G. G. Guzmán-Verri, L. C. Lew Yan Voon, *Physical Review B* **2007**, *76*, 075131.

[35] B. Lalmi, H. Oughaddou, H. Enriquez, A. Kara, S. Vizzini, B. Ealet, B. Aufray, *Applied Physics Letters* **2010**, *97*.

[36] P. Vogt, P. De Padova, C. Quaresima, J. Avila, E. Frantzeskakis, M. C. Asensio, A. Resta, B. Ealet, G. Le Lay, *Physical Review Letters* **2012**, *108*, 155501.

[37] Q. H. Wang, K. Kalantar-Zadeh, A. Kis, J. N. Coleman, M. S. Strano, *Nature Nanotechnology* **2012**, *7*, 699.

[38] J. A. Wilson, A. D. Yoffe, *Advances in Physics* **1969**, *18*, 193.

[39] D. W. Murphy, G. W. Hull, *The Journal of Chemical Physics* **1975**, *62*, 973.

[40] C. Liu, O. Singh, P. Joensen, A. E. Curzon, R. F. Frindt, *Thin Solid Films* **1984**, *113*, 165.

[41] P. Joensen, R. F. Frindt, S. R. Morrison, *Materials Research Bulletin* **1986**, *21*, 457.

[42] B. Radisavljevic, A. Radenovic, J. Brivio, V. Giacometti, A. Kis, *Nature Nanotechnology* **2011**, *6*, 147.

[43] R. E. Schaak, T. E. Mallouk, *Chemistry of Materials* **2000**, *12*, 2513.

[44] Y. Omomo, T. Sasaki, Wang, M. Watanabe, *Journal of the American Chemical Society* **2003**, *125*, 3568.

[45] Y.-S. Han, I. Park, J.-H. Choy, *Journal of Materials Chemistry* **2001**, *11*, 1277.

[46] K. Kalantar-zadeh, J. Tang, M. Wang, K. L. Wang, A. Shailos, K. Galatsis, R. Kojima, V. Strong, A. Lech, W. Wlodarski, R. B. Kaner, *Nanoscale* **2010**, *2*, 429.

[47] N. A. Chernova, M. Roppolo, A. C. Dillon, M. S. Whittingham, *Journal of Materials Chemistry* **2009**, *19*, 2526.

[48] X. Rui, Z. Lu, H. Yu, D. Yang, H. H. Hng, T. M. Lim, Q. Yan, *Nanoscale* **2013**, *5*, 556.

[49] R. Ma, Z. Liu, L. Li, N. Iyi, T. Sasaki, *Journal of Materials Chemistry* **2006**, *16*, 3809.

[50] M. F. Brigatti, E. Galan, B. K. G. Theng, in *Developments in Clay Science, Vol. Volume 1* (Eds.: B. K. G. T. Faïza Bergaya, L. Gerhard), Elsevier, **2006**, pp. 19.

[51] P. F. Luckham, S. Rossi, *Advances in Colloid and Interface Science* **1999**, *82*, 43.

[52] K. Norrish, *Discussions of the Faraday Society* **1954**, *18*, 120.

[53] G. Walker, *Nature* **1960**, *187*, 312.

[54] K. S. Kim, Y. Zhao, H. Jang, S. Y. Lee, J. M. Kim, K. S. Kim, J.-H. Ahn, P. Kim, J.-Y. Choi, B. H. Hong, *Nature* **2009**, *457*, 706.

[55] A. Reina, X. Jia, J. Ho, D. Nezich, H. Son, V. Bulovic, M. S. Dresselhaus, J. Kong, *Nano Letters* **2008**, *9*, 30.

[56] H. Cao, Q. Yu, R. Colby, D. Pandey, C. S. Park, J. Lian, D. Zemlyanov, I. Childres, V. Drachev, E. A. Stach, M. Hussain, H. Li, S. S. Pei, Y. P. Chen, *Journal of Applied Physics* **2010**, *107*.

[57] L. Song, L. Ci, H. Lu, P. B. Sorokin, C. Jin, J. Ni, A. G. Kvashnin, D. G. Kvashnin, J. Lou, B. I. Yakobson, P. M. Ajayan, *Nano Letters* **2010**, *10*, 3209.

[58] H. Wang, L. Yu, Y. Lee, W. Fang, A. Hsu, P. Herring, M. Chin, M. Dubey, L. Li, J. Kong, T. Palacios, in *Electron Devices Meeting (IEDM), 2012 IEEE International*, **2012**, pp. 4.6.1.

[59] Y.-H. Lee, X.-Q. Zhang, W. Zhang, M.-T. Chang, C.-T. Lin, K.-D. Chang, Y.-C. Yu, J. T.-W. Wang, C.-S. Chang, L.-J. Li, T.-W. Lin, *Advanced Materials* **2012**, *24*, 2320.

[60] A. N. Obraztsov, *Nature Nanotechnology* **2009**, *4*, 212.

[61] S. Bae, H. Kim, Y. Lee, X. Xu, J.-S. Park, Y. Zheng, J. Balakrishnan, T. Lei, H. R. Kim, Y. I. Song, *Nature Nanotechnology* **2010**, *5*, 574.

[62] M. P. Levendorf, C. S. Ruiz-Vargas, S. Garg, J. Park, *Nano Letters* **2009**, *9*, 4479.

[63] A. Kara, H. Enriquez, A. P. Seitsonen, L. C. Lew Yan Voon, S. Vizzini, B. Aufray, H. Oughaddou, *Surface Science Reports* **2012**, *67*, 1.

[64] F. Wang, X. Wang, *Nanoscale* **2014**, *DOI: 10.1039/C4NR00973H*.

[65] H. Li, G. Lu, Y. Wang, Z. Yin, C. Cong, Q. He, L. Wang, F. Ding, T. Yu, H. Zhang, *Small* **2013**, *9*, 1974.

[66] S. Balendhran, J. Deng, J. Z. Ou, S. Walia, J. Scott, J. Tang, K. L. Wang, M. R. Field, S. Russo, S. Zhuiykov, M. S. Strano, N. Medhekar, S. Sriram, M. Bhaskaran, K. Kalantar-zadeh, *Advanced Materials* **2013**, *25*, 109.

[67] K. Kalantar-zadeh, A. Vijayaraghavan, M.-H. Ham, H. Zheng, M. Breedon, M. S. Strano, *Chemistry of Materials* **2010**, *22*, 5660.

[68] Y. Hernandez, V. Nicolosi, M. Lotya, F. M. Blighe, Z. Sun, S. De, I. McGovern, B. Holland, M. Byrne, Y. K. Gun'Ko, *Nature Nanotechnology* **2008**, *3*, 563.

[69] S. Park, R. S. Ruoff, *Nature Nanotechnology* **2009**, *4*, 217.

[70] S. Stankovich, D. A. Dikin, R. D. Piner, K. A. Kohlhaas, A. Kleinhammes, Y. Jia, Y. Wu, S. T. Nguyen, R. S. Ruoff, *Carbon* **2007**, *45*, 1558.

[71] G. Eda, G. Fanchini, M. Chhowalla, *Nature Nanotechnology* **2008**, *3*, 270.

[72] Y. Lin, T. V. Williams, J. W. Connell, *The Journal of Physical Chemistry Letters* **2009**, *1*, 277.

[73] Z. Zeng, Z. Yin, X. Huang, H. Li, Q. He, G. Lu, F. Boey, H. Zhang, *Angewandte Chemie International Edition* **2011**, *50*, 11093.

[74] J. Feng, X. Sun, C. Wu, L. Peng, C. Lin, S. Hu, J. Yang, Y. Xie, *Journal of the American Chemical Society* **2011**, *133*, 17832.

[75] L. Li, R. Ma, Y. Ebina, N. Iyi, T. Sasaki, *Chemistry of Materials* **2005**, *17*, 4386.

[76] Q. Wang, D. O'Hare, *Chemical Reviews* **2012**, *112*, 4124.

[77] T. Lan, T. J. Pinnavaia, *Chemistry of Materials* **1994**, *6*, 2216.

[78] J. Ma, Z.-Z. Yu, Q.-X. Zhang, X.-L. Xie, Y.-W. Mai, I. Luck, *Chemistry of Materials* **2004**, *16*, 757.

[79] M. Valášková, M. Rieder, V. Matějka, P. Čapková, A. Slíva, *Applied Clay Science* **2007**, *35*, 108.

[80] J. H. Park, S. C. Jana, *Macromolecules* **2003**, *36*, 2758.

[81] V. Nicolosi, M. Chhowalla, M. G. Kanatzidis, M. S. Strano, J. N. Coleman, *Science* **2013**, *340*.

[82] L. M. Viculis, J. J. Mack, O. M. Mayer, H. T. Hahn, R. B. Kaner, *Journal of Materials Chemistry* **2005**, *15*, 974.

[83] M. J. McAllister, J.-L. Li, D. H. Adamson, H. C. Schniepp, A. A. Abdala, J. Liu, M. Herrera-Alonso, D. L. Milius, R. Car, R. K. Prud'homme, I. A. Aksay, *Chemistry of Materials* **2007**, *19*, 4396.

[84] G. Wang, J. Yang, J. Park, X. Gou, B. Wang, H. Liu, J. Yao, *The Journal of Physical Chemistry C* **2008**, *112*, 8192.

[85] M. Lotya, Y. Hernandez, P. J. King, R. J. Smith, V. Nicolosi, L. S. Karlsson, F. M. Blighe, S. De, Z. Wang, I. T. McGovern, G. S. Duesberg, J. N. Coleman, *Journal of the American Chemical Society* **2009**, *131*, 3611.

[86] M. M. J. Treacy, S. B. Rice, A. J. Jacobson, J. T. Lewandowski, *Chemistry of Materials* **1990**, *2*, 279.

[87] A. J. Van Bommel, J. E. Crombeen, A. Van Tooren, *Surface Science* **1975**, *48*, 463.

[88] K. V. Emtsev, A. Bostwick, K. Horn, J. Jobst, G. L. Kellogg, L. Ley, J. L. McChesney, T. Ohta, S. A. Reshanov, J. Röhrl, *Nature Materials* **2009**, *8*, 203.

[89] C. Berger, Z. Song, T. Li, X. Li, A. Y. Ogbazghi, R. Feng, Z. Dai, A. N. Marchenkov, E. H. Conrad, P. N. First, W. A. de Heer, *The Journal of Physical Chemistry B* **2004**, *108*, 19912.

[90] J. J. Yoo, K. Balakrishnan, J. Huang, V. Meunier, B. G. Sumpter, A. Srivastava, M. Conway, A. L. Mohana Reddy, J. Yu, R. Vajtai, P. M. Ajayan, *Nano Letters* **2011**, *11*, 1423.

[91] E. Yoo, J. Kim, E. Hosono, H.-s. Zhou, T. Kudo, I. Honma, *Nano Letters* **2008**, *8*, 2277.

[92] J. Xiao, D. Choi, L. Cosimbescu, P. Koech, J. Liu, J. P. Lemmon, *Chemistry of Materials* **2010**, *22*, 4522.

[93] J.-w. Seo, Y.-w. Jun, S.-w. Park, H. Nah, T. Moon, B. Park, J.-G. Kim, Y. J. Kim, J. Cheon, *Angewandte Chemie International Edition* **2007**, *46*, 8828.

[94] Y. Jing, Z. Zhou, C. R. Cabrera, Z. Chen, *The Journal of Physical Chemistry C* **2013**, *117*, 25409.

[95] W. Xiao, J. S. Chen, Q. Lu, X. W. Lou, *The Journal of Physical Chemistry C* **2010**, *114*, 12048.

[96] S.-H. Yu, M. Park, H. S. Kim, A. Jin, M. Shokouhimehr, T.-Y. Ahn, Y.-W. Kim, T. Hyeon, Y.-E. Sung, *RSC Advances* **2014**, *4*, 12087.

[97] F. T. Wagner, B. Lakshmanan, M. F. Mathias, *The Journal of Physical Chemistry Letters* **2010**, *1*, 2204.

[98] B. Dunn, H. Kamath, J.-M. Tarascon, *Science* **2011**, *334*, 928.

[99] H. Chen, T. N. Cong, W. Yang, C. Tan, Y. Li, Y. Ding, *Progress in Natural Science* **2009**, *19*, 291.

[100] H. K. Liu, Z. P. Guo, J. Z. Wang, K. Konstantinov, *Journal of Materials Chemistry* **2010**, *20*, 10055.

[101] I. Kovalenko, B. Zdyrko, A. Magasinski, B. Hertzberg, Z. Milicev, R. Burtovyy, I. Luzinov, G. Yushin, *Science* **2011**, *334*, 75.

[102] U. Kasavajjula, C. Wang, A. J. Appleby, *Journal of Power Sources* **2007**, *163*, 1003.

[103] M. Radovic, M. W. Barsoum, *American Ceramics Society Bulletin* **2013**, *92*, 20.

[104] M. W. Barsoum, M. Radovic, *Annual Review of Materials Research* **2011**, *41*, 195.

[105] V. D. Jovic, B. M. Jovic, S. Gupta, T. El-Raghy, M. W. Barsoum, *Corrosion Science* **2006**, *48*, 4274.

[106] M. W. Barsoum, *Progress in Solid State Chemistry* **2000**, *28*, 201.

[107] Z. Sun, D. Music, R. Ahuja, S. Li, J. M. Schneider, *Physical Review B* **2004**, *70*, 092102.

[108] M. W. Barsoum, J. Golczewski, H. J. Seifert, F. Aldinger, *Journal of Alloys and Compounds* **2002**, *340*, 173.

[109] T. El-Raghy, M. W. Barsoum, M. Sika, *Materials Science and Engineering: A* **2001**, *298*, 174.

[110] M. W. Barsoum, T. El-Raghy, L. Farber, M. Amer, R. Christini, A. Adams, *J. Electrochem. Soc.* **1999**, *146*, 3919.

[111] J. Emmerlich, D. Music, P. Eklund, O. Wilhelmsson, U. Jansson, J. M. Schneider, H. Högberg, L. Hultman, *Acta Materialia* **2007**, *55*, 1479.

[112] E. N. Hoffman, G. Yushin, M. W. Barsoum, Y. Gogotsi, *Chemistry of Materials* **2005**, *17*, 2317.

[113] S. Brunauer, P. H. Emmett, E. Teller, *Journal of the American Chemical Society* **1938**, *60*, 309.

[114] G. E. Granroth, A. I. Kolesnikov, T. E. Sherline, J. P. Clancy, K. A. Ross, J. P. C. Ruff, B. D. Gaulin, S. E. Nagler, *Journal of Physics: Conference Series* **2010**, *251*, 012058.

[115] http://www.mantidproject.org.

[116] R. Cheary, A. Coelho, J. Cline, *Journal of Research of the National Institute of Standards and Technology* **2004**, *109*, 1.

[117] G. Pawley, *Journal of Applied Crystallography* **1981**, *14*, 357.

[118] A. Le Bail, H. Duroy, J. L. Fourquet, *Materials Research Bulletin* **1988**, *23*, 447.

[119] A. Coelho, *Journal of Applied Crystallography* **2000**, *33*, 899.

[120] B. Ravel, M. Newville, *Journal of Synchrotron Radiation* **2005**, *12*, 537.

[121] M. Naguib, V. Presser, D. Tallman, J. Lu, L. Hultman, Y. Gogotsi, M. W. Barsoum, *Journal of the American Ceramic Society* **2011**, *94*, 4556.

[122] G. Yushin, E. Hoffman, A. Nikitin, H. Ye, M. Barsoum, Y. Gogotsi, *Carbon* **2005**, *43*, 2075.

[123] N. Batisse, K. Guérin, M. Dubois, A. Hamwi, *Carbon* **2011**, *49*, 2998.

[124] M. Naguib, V. Presser, N. Lane, D. Tallman, Y. Gogotsi, J. Lu, L. Hultman, M. W. Barsoum, *RSC Advances* **2011**, *1*, 1493.

[125] N. V. Tzenov, M. W. Barsoum, *Journal of the American Ceramic Society* **2000**, *83*, 825.

[126] D. E. Mencer, T. R. Hess, T. Mebrahtu, D. L. Cocke, D. G. Naugle, *Journal of Vacuum Science & Technology A* **1991**, *9*, 1610.

[127] S. Myhra, J. A. A. Crossley, M. W. Barsoum, *Journal of Physics and Chemistry of Solids* **2001**, *62*, 811.

[128] T. Sultana, G. L. Georgiev, G. Auner, G. Newaz, H. J. Herfurth, R. Patwa, *Applied Surface Science* **2008**, *255*, 2569.

[129] M. Naguib, M. Kurtoglu, V. Presser, J. Lu, J. Niu, M. Heon, L. Hultman, Y. Gogotsi, M. W. Barsoum, *Advanced Materials* **2011**, *23*, 4248.

[130] M. Naguib, O. Mashtalir, J. Carle, V. Presser, J. Lu, L. Hultman, Y. Gogotsi, M. W. Barsoum, *ACS Nano* **2012**, *6*, 1322.

[131] P. Scherrer, *Göttinger Nachrichten Math. Phys.* **1918**, *2*, 98.

[132] M. Naguib, J. Halim, J. Lu, K. M. Cook, L. Hultman, Y. Gogotsi, M. W. Barsoum, *Journal of the American Chemical Society* **2013**, *135*, 15966.

[133] O. Mashtalir, M. Naguib, B. Dyatkin, Y. Gogotsi, M. W. Barsoum, *Materials Chemistry and Physics* **2013**, *139*, 147.

[134] M. J. McAllister, J.-L. Li, D. H. Adamson, H. C. Schniepp, A. A. Abdala, J. Liu, M. Herrera-Alonso, D. L. Milius, R. Car, R. K. Prud'homme, I. A. Aksay, *Chem. Mater.* **2007**, *19*, 4396.

[135] X. Wang, S. M. Tabakman, H. Dai, *J. Am. Chem. Soc.* **2008**, *130*, 8152.

[136] J. Xiao, D. Mei, X. Li, W. Xu, D. Wang, G. L. Graff, W. D. Bennett, Z. Nie, L. V. Saraf, I. A. Aksay, J. Liu, J.-G. Zhang, *Nano Lett.* **2011**, *11*, 5071.

[137] P. Eklund, J. P. Palmquist, J. Höwing, D. H. Trinh, T. El-Raghy, H. Högberg, L. Hultman, *Acta Mater.* **2007**, *55*, 4723.

[138] S. Lowell, J. E. Shields, *Powder Surface Area and Porosity*, 3rd ed., Chapman & Hall, New Yourk, **1991**.

[139] M. Naguib, J. Come, B. Dyatkin, V. Presser, P.-L. Taberna, P. Simon, M. W. Barsoum, Y. Gogotsi, *Electrochemistry Communications* **2012**, *16*, 61.

[140] J. E. F. C. Gardolinski, G. Lagaly, *Clay Minerals* **2005**, *40*, 547.

[141] D. D. L. Chung, *Journal of Materials Science* **2002**, *37*, 1475.

[142] R. L. Ledoux, J. L. White, *Journal of Colloid and Interface Science* **1966**, *21*, 127.

[143] O. Mashtalir, M. Naguib, V. N. Mochalin, Y. Dall'Agnese, M. Heon, M. W. Barsoum, Y. Gogotsi, *Nature Communications* **2013**, *4*, 1716.

[144] M. R. Lukatskaya, O. Mashtalir, C. E. Ren, Y. Dall'Agnese, P. Rozier, P. L. Taberna, M. Naguib, P. Simon, M. W. Barsoum, Y. Gogotsi, *Science* **2013**, *341*, 1502.

[145] L. Xu, C. Wang, C. Q. Hu, Z. D. Zhao, W. X. Yu, W. T. Zheng, *Journal of Applied Physics* **2009**, *105*, 074318.

[146] M. T. Marques, A. M. Ferraria, J. B. Correia, A. M. B. do Rego, R. Vilar, *Materials Chemistry and Physics* **2008**, *109*, 174.

[147] A. Darlinski, J. Halbritter, *Surface and Interface Analysis* **1987**, *10*, 223.

[148] C. F. Miller, G. W. Simmons, R. P. Wei, *Scripta Materialia* **2000**, *42*, 227.

[149] M. Grundner, J. Halbritter, *Journal of Applied Physics* **1980**, *51*, 397.

[150] Y. Taki, O. Takai, *Thin Solid Films* **1998**, *316*, 45.

[151] J. G. Choi, *Applied Surface Science* **1999**, *148*, 64.

[152] P. Frantz, S. V. Didziulis, L. C. Fernandez-Torres, R. L. Guenard, S. S. Perry, *Journal of Physical Chemistry B* **2002**, *106*, 6456.

[153] M. W. Barsoum, A. Crossley, S. Myhra, *Journal of Physics and Chemistry of Solids* **2002**, *63*, 2063.

[154] Z. Sun, S. Li, R. Ahuja, J. M. Schneider, *Solid State Communications* **2004**, *129*, 589.

[155] X. Min, Y. Ren, *Journal of Wuhan University of Technology-Mater. Sci. Ed.* **2007**, *22*, 27.

[156] I. R. Shein, A. L. Ivanovskii, *Computational Materials Science* **2012**, *65*, 104.

[157] M.-P. Crosnier-Lopez, F. Le Berre, J.-L. Fourquet, *Journal of Materials Chemistry* **2001**, *11*, 1146.

[158] Y. Xie, M. Naguib, V. N. Mochalin, M. W. Barsoum, Y. Gogotsi, X. Yu, K.-W. Nam, X.-Q. Yang, A. I. Kolesnikov, P. R. C. Kent, *Journal of the American Chemical Society* **2014**, *DOI: 10.1021/ja501520b*.

[159] A. N. Enyashin, A. L. Ivanovskii, *The Journal of Physical Chemistry C* **2013**, *117*, 13637.

[160] M. W. Barsoum, *Fundamentals of Ceramics*, Taylor & Francis, New York, **2003**.

[161] E. Wu, E. Herold Kisi, *Journal of the American Ceramic Society* **2006**, *89*, 710.

[162] W.-K. Pang, I.-M. Low, Z.-M. Sun, *Journal of the American Ceramic Society* **2010**, *93*, 2871.

[163] J. Kunze, A. Seyeux, P. Schmuki, *Electrochemical and Solid-State Letters* **2008**, *11*, K11.

[164] M. Khazaei, M. Arai, T. Sasaki, C.-Y. Chung, N. S. Venkataramanan, M. Estili, Y. Sakka, Y. Kawazoe, *Advanced Functional Materials* **2013**, *23*, 2185.

[165] Q. Tang, Z. Zhou, P. Shen, *Journal of the American Chemical Society* **2012**, *134*, 16909.

[166] Y. Xie, P. R. C. Kent, *Physical Review B* **2013**, *87*, 235441.

[167] N. J. Lane, M. W. Barsoum, J. M. Rondinelli, *EPL (Europhysics Letters)* **2013**, *101*, 57004.

[168] M. Kurtoglu, M. Naguib, Y. Gogotsi, M. W. Barsoum, *MRS Communications* **2012**, *2*, 133.

[169] X. Li, Y. Zhu, W. Cai, M. Borysiak, B. Han, D. Chen, R. D. Piner, L. Colombo, R. S. Ruoff, *Nano Lett.* **2009**, *9*, 4359.

[170] P. Blake, P. D. Brimicombe, R. R. Nair, T. J. Booth, D. Jiang, F. Schedin, L. A. Ponomarenko, S. V. Morozov, H. F. Gleeson, E. W. Hill, A. K. Geim, K. S. Novoselov, *Nano Lett.* **2008**, *8*, 1704.

[171] M. W. Barsoum, in *Encyclopedia of Materials: Science and Technology* (Eds.: K. H. J. Buschow, R. W. Cahn, M. C. Flemings, B. Ilschner, E. J. Kramer, S. Mahajan, P. Veyssière), Elsevier, Oxford, **2006**, pp. 1.

[172] J. Rafiee, M. A. Rafiee, Z.-Z. Yu, N. Koratkar, *Adv. Mater.* **2010**, *22*, 2151.

[173] Y. Dall'agnese, Master thesis, Drexel University **2012**.

[174] S. R. Sivakkumar, J. Y. Nerkar, A. G. Pandolfo, *Electrochimica Acta* **2010**, *55*, 3330.

[175] Z. Yang, D. Choi, S. Kerisit, K. M. Rosso, D. Wang, J. Zhang, G. Graff, J. Liu, *Journal of Power Sources* **2009**, *192*, 588.

[176] R. A. Huggins, *Journal of Power Sources* **1999**, *81–82*, 13.

[177] T. Moon, C. Kim, B. Park, *Journal of Power Sources* **2006**, *155*, 391.

[178] J. J. Xu, J. Yang, *Electrochemistry Communications* **2003**, *5*, 230.

[179] J. Li, Z. Tang, Z. Zhang, *Electrochemistry Communications* **2005**, *7*, 62.

[180] L. Mai, L. Xu, B. Hu, Y. Gu, *Journal of Materials Research* **2010**, *25*, 1413.

[181] M. Sasidharan, N. Gunawardhana, M. Yoshio, K. Nakashima, *Materials Research Bulletin* **2012**, *47*, 2161.

[182] J. B. Goodenough, Y. Kim, *Chemistry of Materials* **2009**, *22*, 587.

[183] A. K. Padhi, K. S. Nanjundaswamy, C. Masquelier, J. B. Goodenough, *Journal of the Electrochemical Society* **1997**, *144*, 2581.

[184] H. Han, T. Song, J.-Y. Bae, L. F. Nazar, H. Kim, U. Paik, *Energy & Environmental Science* **2011**, *4*, 4532.

[185] H. Ming, X. Li, L. Su, M. Liu, L. Jin, L. Bu, Z. Kang, J. Zheng, *RSC Advances* **2013**, *3*, 3836.

[186] H. Ming, J. Ming, X. Li, Q. Zhou, H. Wang, L. Jin, Y. Fu, J. Adkins, J. Zheng, *Electrochimica Acta* **2014**, *116*, 224.

[187] J.-G. Kim, D. Shi, K.-J. Kong, Y.-U. Heo, J. H. Kim, M. R. Jo, Y. C. Lee, Y.-M. Kang, S. X. Dou, *ACS Applied Materials & Interfaces* **2013**, *5*, 691.

[188] A. L. M. Reddy, A. Srivastava, S. R. Gowda, H. Gullapalli, M. Dubey, P. M. Ajayan, *ACS Nano* **2010**, *4*, 6337.

[189] X. Wang, X. Cao, L. Bourgeois, H. Guan, S. Chen, Y. Zhong, D.-M. Tang, H. Li, T. Zhai, L. Li, Y. Bando, D. Golberg, *Advanced Functional Materials* **2012**, *22*, 2682.

[190] H. Wang, C. Zhang, Z. Liu, L. Wang, P. Han, H. Xu, K. Zhang, S. Dong, J. Yao, G. Cui, *Journal of Materials Chemistry* **2011**, *21*, 5430.

[191] A. N. Enyashin, A. L. Ivanovskii, *Journal of Solid State Chemistry* **2013**, *207*, 42.

[192] W. H. Shin, H. M. Jeong, B. G. Kim, J. K. Kang, J. W. Choi, *Nano Letters* **2012**, *12*, 2283.

[193] C. Masarapu, V. Subramanian, H. Zhu, B. Wei, *Advanced Functional Materials* **2009**, *19*, 1008.

[194] B. Hao, Y. Yan, X. Wang, G. Chen, *ACS Applied Materials & Interfaces* **2013**, *5*, 6285.

[195] Q. Tang, Z. Zhou, P. W. Shen, *J Am Chem Soc* **2012**, *134*, 16909.

[196] L. Su, Z. Zhou, P. Shen, *The Journal of Physical Chemistry C* **2012**, *116*, 23974.

[197] L. Su, Z. Zhou, P. Shen, *Electrochimica Acta* **2013**, *87*, 180.

[198] L. Su, Z. Zhou, X. Qin, Q. Tang, D. Wu, P. Shen, *Nano Energy* **2013**, *2*, 276.

[199] X.-L. Wang, K. An, L. Cai, Z. Feng, S. E. Nagler, C. Daniel, K. J. Rhodes, A. D. Stoica, H. D. Skorpenske, C. Liang, W. Zhang, J. Kim, Y. Qi, S. J. Harris, *Sci. Rep.* **2012**, *2*, 1.

[200] K. Nakahara, R. Nakajima, T. Matsushima, H. Majima, *Journal of Power Sources* **2003**, *117*, 131.

[201] J. Come, M. Naguib, P. Rozier, M. W. Barsoum, Y. Gogotsi, P.-L. Taberna, M. Morcrette, P. Simon, *Journal of The Electrochemical Society* **2012**, *159*, A1368.

[202] R. Baddour-Hadjean, S. Bach, M. Smirnov, J.-P. Pereira-Ramos, *Journal of Raman Spectroscopy* **2004**, *35*, 577.

[203] T. Kim, S. Park, S. M. Oh, *Journal of the Electrochemical Society* **2007**, *154*, A1112.

[204] M. Hahn, H. Buqa, P. W. Ruch, D. Goers, M. E. Spahr, J. Ufheil, P. Novák, R. Kötz, *Electrochemical and Solid-State Letters* **2008**, *11*, A151.

[205] T. Ohzuku, N. Matoba, K. Sawai, *Journal of Power Sources* **2001**, *97–98*, 73.

[206] T. Ohzuku, Y. Iwakoshi, K. Sawai, *Journal of the Electrochemical Society* **1993**, *140*, 2490.

[207] J. G. Chen, *Surface Science Reports* **1997**, *30*, 1.

[208] W. J. Borghols, D. Lützenkirchen-Hecht, U. Haake, W. Chan, U. Lafont, E. M. Kelder, E. R. van Eck, A. P. Kentgens, F. M. Mulder, M. Wagemaker, *Journal of The Electrochemical Society* **2010**, *157*, A582.

[209] U. Lafont, D. Carta, G. Mountjoy, A. V. Chadwick, E. M. Kelder, *The Journal of Physical Chemistry C* **2009**, *114*, 1372.

[210] A. M. Andersson, D. P. Abraham, R. Haasch, S. MacLaren, J. Liu, K. Amine, *Journal of the Electrochemical Society* **2002**, *149*, A1358.

[211] I. Ismail, A. Noda, A. Nishimoto, M. Watanabe, *Electrochimica Acta* **2001**, *46*, 1595.

[212] M. Herstedt, A. M. Andersson, H. Rensmo, H. Siegbahn, K. Edström, *Electrochimica Acta* **2004**, *49*, 4939.

[213] M.-S. Wu, M.-J. Wang, J.-J. Jow, W.-D. Yang, C.-Y. Hsieh, H.-M. Tsai, *Journal of Power Sources* **2008**, *185*, 1420.

[214] M. Pfanzelt, P. Kubiak, S. Jacke, L. Dimesso, W. Jaegermann, M. Wohlfahrt-Mehrens, *Journal of the Electrochemical Society* **2012**, *159*, A809.

[215] V. Eshkenazi, E. Peled, L. Burstein, D. Golodnitsky, *Solid State Ionics* **2004**, *170*, 83.

[216] A. S. Ingason, A. Petruhins, M. Dahlqvist, F. Magnus, A. Mockute, B. Alling, L. Hultman, I. A. Abrikosov, P. O. Å. Persson, J. Rosen, *Materials Research Letters* **2013**, *2*, 89.

[217] J. R. Szczech, S. Jin, *Energy & Environmental Science* **2011**, *4*, 56.

[218] W. Q. Fang, J. Z. Zhou, J. Liu, Z. G. Chen, C. Yang, C. H. Sun, G. R. Qian, J. Zou, S. Z. Qiao, H. G. Yang, *Chemistry – A European Journal* **2011**, *17*, 1423.

[219] J. Chen, W. Jong Yoo, D. S. H. Chan, *Journal of the Electrochemical Society* **2006**, *153*, G483.

[220] W. C. Johnson, J. B. Parsons, *The Journal of Physical Chemistry* **1931**, *36*, 2588.

VITA

Michael Naguib Abdelmalak

Email: michael.naguib@gmail.com

Education:

- **Drexel University**, Philadelphia, PA, USA.
  PhD in Materials Science and Engineering, 01/2010-04/2014 (***GPA: 3.99***)
- **Cairo University**, Egypt.
  MSc in Metallurgical Engineering, 10/2007-12/2009
  BSc in Metallurgical Engineering, 09/2002-07/2007 (***Distinction with Honors Degree, and First of Class***)

Awards and Fellowships:

• Wigner Fellowship at Oak Ridge National Laboratory, 2014. • MRS Gold Graduate Student Award (GSA), Spring 2014. • Ross Coffin Purdy Award, 2013. • Graduate Excellence in Materials Science (GEMS) Award, 2013. • Roland B. Snow Award, 2013 and 2012. • DAAD (The German Academic Exchange Service) Short Term Grant Scholarship, 11/2012-01/2013. • George Hill, Jr. Endowed Fellowship, 2012. • Best Poster Award from the Organizers of Symposium O, Beyond Graphene – 2D Atomic Layers from Layered Materials, at the 2013 MRS Spring Meeting. • Best Poster Award from Drexel ECS student chapter, 2012. • People's choice award for International Science & Engineering Visualization Challenge from NSF, 2012.

Publications:

2014

1. **Naguib, M.;** Mochalin, V.N.; Barsoum, M.W.; Gogotsi, Y., 25th Anniversary Article: *MXenes*: A New Family of Two-Dimensional Materials, ***Advanced Materials 2014***, 26 (7), 992-1005.
2. Shi, C.; Beidaghi, M.; **Naguib, M.**; Mashtalir, O.; Gogotsi, Y.; Billinge, S.J.L., Structure of Nanocrystalline Ti_3C_2 MXene Using Atomic Pair Distribution Function, ***Physical Review Letters 2014*****.** 112 (12), 125501.
3. **Naguib, M.**; Mashtalir, O.; Lukatskaya, M.R.; Dyatkin, B.; Zhang, C; Presser, V.; Gogotsi, Y.; Barsoum, M.W., One-Step Synthesis of Nanocrystalline Transition Metal Oxide on Thin Sheets of Disordered Graphitic Carbon by Oxidation of MXenes, ***Chemical Communications 2014***, DOI:10.1039/C4CC01646G.
4. Lukatskaya, M.R.; Halim, J.; Dyatkin, B.; **Naguib, M.**; Buranova, Y.S.; Barsoum, M.W.; Gogotsi, Y., Room-Temperature Carbide Derived Carbon Synthesis by Electrochemical Etching of MAX Phases, ***Angewandte Chemie 2014,*** DOI: 10.1002/anie.201402513**.**
5. Xie, Y.; **Naguib, M.**; Mochalin, V.N.; Barsoum, M.W.; Gogotsi, Y.; Yu, X.; Nam, K-W.; Yang, X-Q.; Kolesnikov, A.I.; Kent, P.R.C., Role of Surface Structure on Li-ion Energy Storage Capacity of Two-dimensional Transition Metal Carbides, ***Journal of the American Chemical Society 2014*****.** DOI: 10.1021/ja501520b.

2013

6. **Naguib, M.;** Halim, J.; Lu, J.; Cook, M.K; Hultman, L.; Gogotsi, Y.; and Barsoum, M.W., New Two-Dimensional Niobium and Vanadium Carbides as Promising Materials for Li-ion Batteries, ***Journal of the American Chemical Society 2013***, 135 (43), 15966-15969.

7. Lukatskaya, M.R.; Mashtalir, O.; Ren, C.E.; Dall'Agnese, Y.; Rozier, P.; Taberna, P.L.; **Naguib, M.**; Simon, P.; Barsoum, M.W.; and Gogotsi, Y., Cation Intercalation and High Volumetric Capacitance of Two-dimensional Titanium Carbide, ***Science 2013****,* 341 (6153), 1502-1505.
8. Mashtalir, O.; **Naguib, M.;** Mochalin, V.N.; Dall'Agnese, Y.; Heon, M; Barsoum, M.W.; Gogotsi, Y., Intercalation and Delamination of Layered Carbides and Carbonitrides, ***Nature Communications 2013****,* 4, 1716-1722.
9. Mashtalir, O.; **Naguib, M.;** Dyatkin, B.; Gogotsi, Y.; Barsoum, M.W., Kinetics of Aluminum Extraction from Ti_3AlC_2 in Hydrofluoric Acid, *Materials Chemistry and Physics* ***2013****,* 139 (1), 147-152.
10. Mashtalir, O.; Kurtoglu, M.; Pogulay, S.; Gogotsi, A.; **Naguib, M.;** Gogotsi, Y., Photocatalytic WO_3 and TiO_2 Films on Brass, ***International Journal of Applied Ceramic Technology 2013,*** 10 (1), 26-32.

2012

11. **Naguib, M.;** Mashtalir, O.; Carle, J.; Presser, V; Lu, J.; Hultman, L.; Gogotsi, Y.; Barsoum, M.W., Two-Dimensional Transition Metal Carbide, ***ACS Nano 2012,*** 6 (2), 1322-1331.
12. **Naguib, M.**; Come, J.; Dyatkin, B.; Presser, V.; Taberna, P-L.; Simon, P.; Barsoum, M. W.; Gogotsi, Y.; MXene: A Promising Transition Metal Carbide Anode Material for Lithium-ion Batteries, ***Electrochemistry Communications 2012,*** 16 (1), 61-64.
13. Come, J.; **Naguib, M.**; Rozier, P.; Barsoum, M.W.; Gogotsi, Y. ; Taberna, P-L.; Morcrette, M.; Simon, P., A Non-aqueous Asymmetric Cell with a Ti_2C Based Two-Dimensional Negative Electrode, ***Journal of The Electrochemical Society 2012***, 159 (7) A1-A6.
14. Lane, N.J.; **Naguib, M.**; Lu, J.; Eklund, P.; Hultman, L.; Barsoum, M.W., Comment on "$Ti_5Al_2C_3$: A New Ternary Carbide Belonging to MAX Phases in the Ti–Al–C System" ***Journal of the American Ceramic Society 2012***, 95 (10), 3352-3354.
15. Kurtoglu, M.; **Naguib, M.**; Gogotsi, Y.; Barsoum, M.W., First Principles Study of Two-Dimensional Early Transition Metals Carbides, ***MRS Communications 2012*****,** 2 (4), 133-137.
16. Presser, V.; **Naguib, M.**; Chaput, L.; Togo, A.; Hugd, G.; Barsoum, M.W., First-order Raman scattering of the MAX phases: Ti_2AlN, $Ti_2AlC_{0.5}N_{0.5}$, Ti_2AlC, $(Ti_{0.5}V_{0.5})_2AlC$, V_2AlC, Ti_3AlC_2, and Ti_3GeC_2, ***Journal of Raman Spectroscopy 2012*****,** 43 (1),168-172.
17. Lane, N.; **Naguib, M.**; Presser, V; Hugd, G.; Hultman, L.; Barsoum, M.W., First-Order Raman Scattering of the MAX phases Ta_4AlC_3, Nb_4AlC_3, Ti_4AlN_3 and Ta_2AlC, ***Journal of Raman Spectroscopy 2012***, 43 (7), 954-958.
18. Lane, N.J.; **Naguib, M.**; Lu, J.; Hultman, L.; Barsoum, M.W., Structure of a New bulk $Ti_5Al_2C_3$ MAX Phase Produced by the Topotactic Transformation of Ti_2AlC, ***Journal of European Ceramic Society 2012***, 32 (12), 3485-3491.
19. Tallman, D.; **Naguib, M.**; Anasori, B.; Barsoum, M.W., Tensile Creep of Ti_2AlC in the 1000-1150ºC Temperature Range, ***Scripta Materialia 2012,*** 66 (10), 805-808.

2011

20. **Naguib, M.**; Kurtoglu, M.; Presser, V.; Lu, J.; Niu, J.; Heon, M.; Hultman, L.; Gogotsi, Y.; Barsoum, M. W., Two Dimensional Nanocrystals Produced by Exfoliation of Ti_3AlC_2, ***Advanced Materials 2011***, 23 (37), 4248-4253.
21. **Naguib, M.**; Presser, V.; Lane, N.; Tallman, D.; Gogotsi, Y.; Lu, J.; Hultman, L.; Barsoum, M.W., Synthesis of a New Nanocrystalline Titanium Aluminum Fluoride Phase by Reaction of Ti_2AlC with Hydrofluoric Acid**,** ***RSC Advances 2011***, 1 (8), 1493-1499.
22. **Naguib, M.**; Presser, V.; Tallman, D.; Lu, J.; Hultman, L.; Gogotsi, Y.; Barsoum, M.W., On the Topotactic Transformation of Ti_2AlC into a Ti-C-O-F Cubic Phase by Heating in Molten

Lithium Fluoride in Air, ***Journal of the American Ceramic Society 2011***, 94 (12), 4556-4561.

Manuscripts under Review:

1. **Naguib, M.**; Bentzel, G.W.; Shah, J.; Halim, J.; Caspi, E.N.; Lu, J.; Hultman, L.; Barsoum, M.W., New Solid Solution MAX Phases: $(Ti_{0.5},V_{0.5})_3AlC_2$, $(Nb_{0.5},V_{0.5})_2AlC$, $(Nb_{0.5},V_{0.5})_4AlC_3$, and $(Nb_{0.8},Zr_{0.2})_2AlC$, ***Under Review 2014***.
2. Er, D.; Li, J.; **Naguib, M.**; Gogotsi, Y.; Shenoy, V.B., MXenes as High Capacity Electrode Materials for Metal (Li, Na, K, Ca)-Ion Batteries, ***Under Review 2014.***
3. Mauchamp, V.; Bugnet, M.; Bellido, E.P.; Botton, G.A.; Moreau, P.; Magne, D.; **Naguib, M**.; Barsoum, M.W.; Cabioc'h, T., Enhanced and Tunable Surface Plasmons in Two-Dimensional Ti_3C_2 Stacks: Electronic Structure *vs* Boundary Effects, ***Under Review 2014.***